Evaluation of Different Techniques for Repair of Shear-span Corrosion-Damaged RC Beams

by

Hesham Elhuni

A thesis
presented to the University of Waterloo
in fulfillment of the
thesis requirement for the degree of
Master of Applied Science
in
Civil Engineering

Waterloo, Ontario, Canada, 2013

Declaration

I hereby declare that I am the sole author of this thesis. This is a true copy of the thesis, including any required final revisions, as accepted by my examiners.

I understand that my thesis may be made electronically available to the public.

Hesham Elhuni

Abstract

Deterioration of reinforced concrete structures due to reinforcement corrosion is a serious problem that faces concrete infrastructure worldwide. Effect of the rebar corrosion in the shear span on the structural behaviour is not fully addressed in the published literature. This study examined the effects of corrosion of the longitudinal reinforcement in the shear span on the structural behaviour of RC beams and the effectiveness of three rehabilitation schemes on the structural performance of such beams. The experimental program consisted of testing fifteen medium-scale reinforced concrete beams (150mm wide x 350 deep x 2400mm long) under static load. Test variables included: span to depth ratio, the degree of corrosion and the anchorage end condition and repair schemes. Two span to depth (a/d) ratios were considered: a/d=3.4 with one-point loading and a/d=2.4 with two-point loading. Two anchorage end-conditions were used: bonded or un-bonded reinforcement in the anchorage zone. Four degrees of corrosion were chosen to simulate minor (2.5% to 5% mass loss), medium (7.5% mass loss), and severe (15% mass loss) degrees of corrosion. Corrosion was induced in the longitudinal reinforcement in the shear-span using accelerated corrosion techniques based on Faradays' law. Three different repair scenarios were applied. The first scenario included removing the deteriorated concrete, cleaning the corroded steel and patching with a new self-compacting concrete. The second scenario included U-wrapping the beams cross-section using Glass fiber reinforced cement-based composite (GFRCM), and Carbon fiber reinforced cement-based composite (CFRCM) without removing the deteriorated concrete. The third scenario included patch repair and confinement by wrapping with GFRCM or CFRCM. Following corrosion and repair, all specimens were loaded statically to failure. Test results showed no major effect of shear-span corrosion on the flexural behaviour for the beams with end anchorage whereas a noticeable effect on the flexural behaviour was observed for beams with no end anchorage regions. The corrosion degree and the shear span to depth ratio affected the mode of failure for the specimens with no end anchorages. The type of repair significantly affected the overall behaviour of the corroded specimens. An analytical model was proposed and used to predict the load-deflection response of the tested specimens. The program calculated the mid-span deflection for a given load as an integration of the deflection of

a series of elements, with the deflection being based on the elongation of the steel reinforcement in each element. A modified bond stress-slip model was incorporated into the calculations to account for the change in bond strength caused by the corrosion and/or confinement that are provided by repairs. The predicted results were in reasonable agreement with the experimental results.

Acknowledgements

After thanking God for giving me the strength and ability to complete this work, I would like to express my sincere thanks to my family and my closest friends who have instilled in me the drive and encouragement to complete this work.

I would like also to express my appreciation and gratitude to my thesis supervisor, Professor Khaled Soudki, for there encouragement, guidance, and support in my research. He gave me valuable insight and motivation for this work. I would also like to acknowledge and thank all the technicians of the Department of Civil Engineering at the University of Waterloo and all my colleagues in the Structure-Rehabilitation Research Group for their support and useful discussion.

Table of Contents

List of Figures

xi

List of Tables

Chapter 1

Introduction

1.1 Introduction

The functionality of a reinforced concrete (RC) member under loads depends on the composite action between the reinforcing steel and the surrounding concrete. The effectiveness of this action requires adequate interfacial bond strength at the concrete-steel interface. Many factors affect the quality of bond between steel reinforcement and concrete: the geometry and stress level of the reinforcement, the quality of concrete and its state of stress, environmental effects, and the load-and-time-history (FIB, 2000). Corrosion of the reinforcement is a major environmental factor which contributes to the deterioration of RC structures (Nossoni, 2010; Wang and Liu, 2010; and Soudki, et al 2007). One factor that increases vulnerability to corrosion is exposure to seawater and de-icing chemicals. For example, in U.S., $150 billion worth of corrosion damage has occurred on interstate highway bridges due to corrosion induced by de-icing and sea salt (Corrosion of steel in concrete, 2006).

Corrosion has a noticeable effect on the serviceability of reinforced concrete structures. The ultimate strength of RC elements could also be reduced under severe corrosion levels. The main driving force behind the corrosion deterioration is not related to the corrosion creating a decrease in the mechanical strength of the reinforcing bar or the reduction of the mechanical strength of the reinforcing bar instead, the pressure exerted by the expansion of the corrosion products cannot be supported by the limited tensile strength of the concrete, causing cracks to form in the area surrounding the rebar (Sahamitmongkol, et al 2007; Nossoni, and Hirichandran 2010; and Wang and Liu, 2010). When the corrosion-induced cracks extend to the concrete surface through the concrete cover, which acts as a physical barrier, the steel comes into direct contact with the surrounding media, which then escalates the corrosion process. The result is a significant reduction in the safety, serviceability and service life of the structure, with a long-term increase in maintenance costs and risk of injury.

Corrosion has an enormous impact on today's economy. For example, the annual direct cost of corrosion in highway bridges in the U.S. is estimated to be $8.3 billion (Koch et al., 2001). The repair of damaged concrete structures has become a significant component of the concrete industry: millions of dollars are spent annually on improvements in repair materials, extensive research has been conducted with the goal of understanding the behaviour of corroded concrete structures, and the engineering perspective has been modernized to include not only concerns about the applicability of structural design safety codes and construction specifications, but also attention to the mechanisms that cause concrete deterioration and repair methods. In summary, the corrosion of steel reinforcement causes early failure of reinforced concrete structures, leading to huge expenditures for inspection and rehabilitation. Understanding the causes of the corrosion deterioration is therefore essential for successful design for increasing the service life of the structure, and for reducing rehabilitation costs.

There has been remarkable developments in repair techniques, including notable advances in repair materials such as self compacting concrete (SCC) patches, fiber reinforced cement composites (FRCMs), and fiber reinforced polymers (FRPs). Fiber reinforced polymers (FRPs) have been broadly used for repairing and strengthening of reinforced concrete structures over the last 50 years. The effect of the FRPs application on the RC elements has been the subject for intensive investigations from both experimental and theoretical prospective. Based on these investigations, design codes and guidelines have been published (ACI 440.2R-08). FRPs have proven many advantages: high strength, light weight, corrosion resistivity, flexibility, and the fast application. However, there are some disadvantages with respect to FRPs application: the resistivity to fire, and the difficulty of application at low temperature environment and humid surfaces (Badanoiu and Holmgren, 2003). To overcome these disadvantages, advanced composite systems (FRCMs) composed of cement- based matrix reinforced with continuous fibers have been recently invented. FRCMs are characterized by high heat resistivity, and the ability to apply at low temperature environment or on wet surfaces (D'Ambrisi and Focacci, 2011), nevertheless; experimental and theoretical research is needed to assess and evaluate their mechanical effectiveness.

This research study falls within the general category of the selection of the ideal structural repair strategies for concrete deterioration caused by corrosion of steel reinforcement.

1.2 Research Motivation

The effect of the corrosion of tensile reinforcement on the structural behaviour of RC beams has been the subject of extensive research over the past 20 years. In most of the previous studies, the full length of the longitudinal rebar was corroded (Soudki and Sherwood, 2000; Masoud et al., 2001; El Maaddawy and Soudki, 2005; Craig and Soudki, 2005). However, in real life, only a localized portion of the rebar may be corroded, and the corrosion damage within a specific section length of the reinforcement may have a disproportional effect on the residual strength of the entire RC structural element.

The published studies related to the effect of shear-span corrosion on the structural behaviour of RC beams have reported contradictory results. Badawi and Soudki (2010) investigated the effect of shear-span corrosion of longitudinal reinforcement on the structural performance of RC beams with hooked end anchorages. They reported that with properly anchored reinforcement, shear-span corrosion has an insignificant effect on the flexural behaviour of RC beams. Wang et al. (2011) examined the impact of localized, single-shear-span corrosion damage on the shear behaviour of RC beams. Their results indicate that severe localized corrosion damage within the shear-span greatly affected the structural behaviour of the test specimens.

1.3 Objective of the Study

The research presented in this thesis was conducted to investigate the effect of shear-span corrosion on the structural behaviour of RC beams. Specifically, the research study will:

- Study the effect of shear-span corrosion on the structural performance of RC beams with properly anchored and intentionally non-anchored longitudinal reinforcement.

- Examine the effectiveness of various repair systems (patch repair, FRCM repair, and combined patch-FRCM repair) on the structural performance of RC beams with shear-span corroded longitudinal reinforcement.
- Model the structural behaviour of RC beams with shear-span corroded longitudinal reinforcement.

1.4 Thesis Organization

This thesis is composed of six chapters. Chapter 1 addresses the motivation and objectives of the research. Chapter 2 is the literature review explains the fundamentals of steel corrosion in concrete and reviews some of the latest experimental studies and models related to the structural behaviour of corroded structures. Chapter 3 describes the experimental program including test specimens, corrosion technique, repair techniques, instrumentations, and load testing. Chapter 4 provides a detailed analysis and discussion of the results. Chapter 5 introduces an analytical model for predicting the experimental results of the study. Chapter 6 gives the conclusions of the study and recommendations for further research.

Chapter 2
Literature Review

2.1 Fundamentals of Steel Corrosion in Concrete

2.1.1 Nature of corrosion

As with any natural process that has a tendency towards the lowest possible energy states, steel iron tends to combine with chemicals in the presence of oxygen and water in the natural environment in order to return to its lowest energy state (iron oxides, or rust). However, while steel requires acids in order to become corroded, it can be protected from corrosion by alkalis. Concrete is alkaline because it contains soluble calcium, sodium, and potassium oxides in its pore structure. These oxides react with water to form alkaline hydroxides: the hydrogen concentration number (pH) is in the range of 12-13. The alkalis are believed to provide an appropriate condition for the formation of a passive layer on the steel surface (passive film). This layer is dense and fully established which prevents further corrosion of the steel because it slows up the rate of oxidation. The passive layer is believed to be composed of combination of hydroxides from the steel and minerals from the concrete. As long as the pH remains within the specified range, the passive layer is maintained and regenerates on the steel surface. The passive film ranges in thickness from 10^{-3} μm to 10^{-1} μm (Ramachandran, 2001). However, two conditions can cause the passive environment to break down: carbonation and chloride attack, both of which are discussed later in this chapter.

2.1.2 Occurrence of Corrosion; an electrochemical reaction

Whether the initiating condition for corrosion is due to carbonation or chloride attack, the corrosion process is identical (Figure 2.1). Once the passive film is broken, both anodic and cathodic chemical reactions occur, the steel corrosion process is initiated: the anodic reaction leads to the de-passivation of the steel rebar. When steel corrodes, the corrosion product dissolves in the pore water and frees up electrons:

$$Fe \rightarrow Fe^{+2} + 2e^- \tag{2.1}$$

In the presence of oxygen and water, the two free electrons consumed at the steel surface cause a cathodic reaction in which hydroxyl ions are generated:

$$2e^- + H_2O + \frac{1}{2}O_2 \rightarrow 2OH^- \tag{2.2}$$

A flux of ions and electrons between the anode and the cathode is necessary for the corrosion process to proceed (Hunkeler, 2005). The pore water solution serves as a bridge for the transport of ions, while the reinforcement itself operates as a medium for the transport of the electrons. The anodic and cathodic reactions are in fact the first steps in the reaction that create rust. The next step is the transformation of the ferrous hydroxide $Fe(OH)_2$ to ferric hydroxide and then to hydrated ferric oxide or rust:

$$Fe^{2+} + 2OH^- \rightarrow Fe(OH)_2 \quad \text{Ferrous hydroxide} \tag{2.3}$$

$$4Fe(OH)_2 + O_2 + 2H_2O \rightarrow 4Fe(OH)_3 \quad \text{Ferric hydroxide} \tag{2.4}$$

$$2Fe(OH)_3 \rightarrow Fe_2O_3.H_2O + 2H_2O \quad \text{Hydrated ferric oxide (rust)} \tag{2.5}$$

Fe^{2+} + 2OH$^-$ → Fe(OH)$_2$ Ferrous hydroxide
4Fe(OH)$_2$ + O$_2$ + 2H$_2$O → 4Fe(OH)$_2$ Ferric hydroxide
2Fe(OH)$_2$ → Fe$_2$O$_3$ · H$_2$O + 2H$_2$O Hydrated ferric oxide (rust)
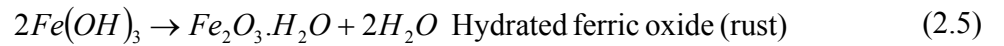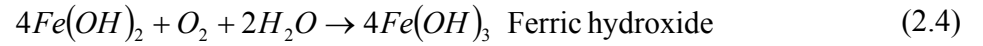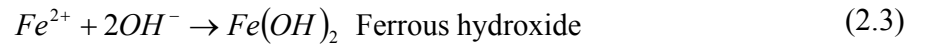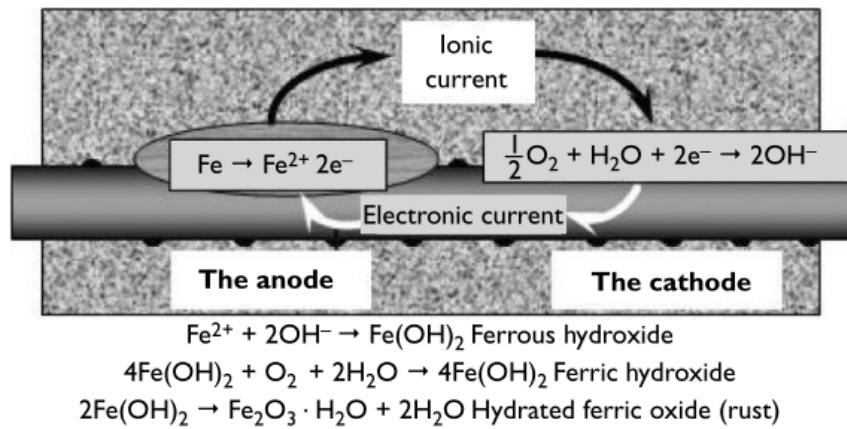
Figure 2.1: The anodic, cathodic, oxidation and hydration reactions in the corrosion of steel (Corrosion of steel in concrete, 2006)

When ferric oxide Fe_2O_3 is hydrated, it swells more than twice the volume it had when un-hydrated on the steel surface. This process creates six to ten times the amount of rust at the steel concrete interface; causing the concrete to crack and eventually spall-off (Figure 2.2).
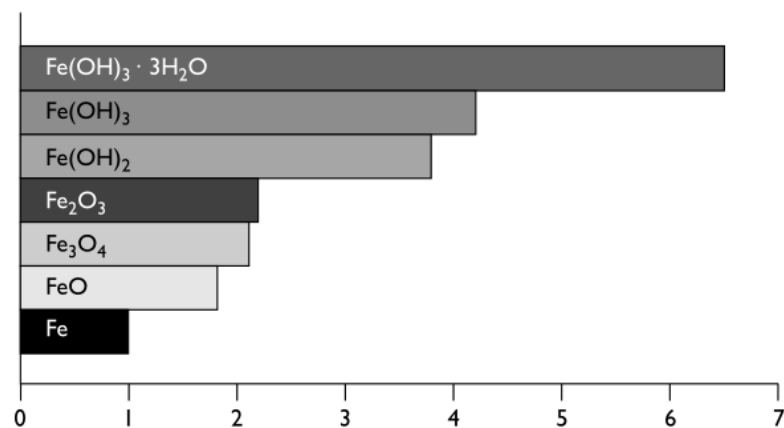
Figure 2.2: Relative volume of iron and its oxides (Corrosion of steel in concrete, 2006)

2.1.3 Carbonation

Carbonation conditions occur when the alkaline hydroxides in the concrete react with the carbon dioxide gas in the air. The result of this interaction is carbonic acid, which neutralizes the alkaline in the concrete pores and forms calcium carbonate. As the carbon dioxide continues to react with the calcium hydroxides in the concrete pores, the pH falls to the level at which steel will corrode (Smith, 2007).

$$\underbrace{CO_2}_{Gas} + \underbrace{H_2O}_{Water} \rightarrow \underbrace{H_2CO_3}_{Carbonic\ acid} \tag{2.6}$$

$$\underbrace{H_2CO_3}_{Carbonic\ acid} + \underbrace{Ca(OH)_2}_{Pore\ solution} \rightarrow CaCO_3 + 2H_2O \tag{2.7}$$
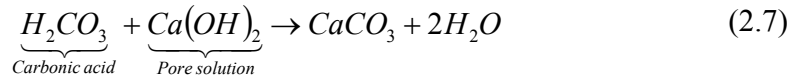
2.1.4 Chloride attack

Chloride attacks concrete in several ways: the use of seawater in the concrete mix, the use of contaminated aggregates, the use sea salt spray and direct seawater for wetting, and the use the de-icing salts. When salt water, for example, is absorbed by the concrete, chloride ions attack the passive film, which allows the corrosion process to proceed quickly, even though the pH does not drop significantly.

The mechanism by which the chloride ions break up the passive film is still not fully understood. Gu et al. (2001) presented three possible scenarios for the chloride attack. One theory proposes that the chloride ions can directly penetrate the passive film and attack the steel; they form a kind of colloid and diffuse the film. According to the second theory, the chloride ions are adsorbed at the steel surface, thus encouraging the hydration of the ions and initiating corrosion. The last theory hypothesizes that the chloride ions are integrated into the passive film through the substituting of some hydroxides; the passive layer becomes more soluble and thus unable to provide protection for the steel.

2.1.5 Corrosion damage

Higgins et al. (2003) divided the progression of the deterioration due to corrosion into four phases (Figure 2.3):

- Initiation phase, which is characterized by the de-passivation of the steel reinforcement due to carbonation or chloride attack.

- The first propagation phase, which is characterized by the cracking of the concrete and the appearance of rust staining on the surface of the concrete.

- The second propagation phase, in which the concrete cracks are widened and the concrete is delaminated.

- The serviceability-failure stage, in which the concrete cover begins to spall, as a result of a long period of direct exposure to a highly corrosive environment.
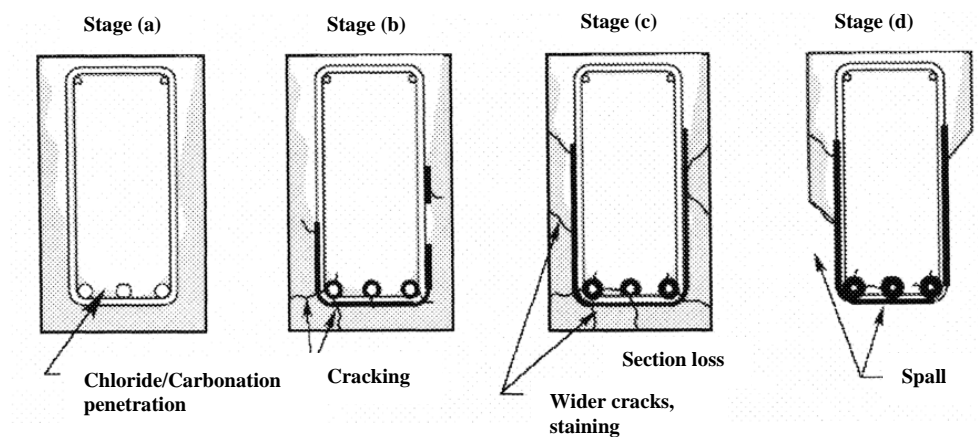
Figure 2.3: Corrosion deterioration phases of RC beams (Higgins et al., 2003)

2.2 Effect of Corrosion on the Structural Behaviour of Reinforced Concrete

The effect of corrosion on the performance of reinforced concrete members has been addressed by many researchers, who generally agree that the corrosion has an adverse effect on structural performance (flexure, shear, and bond). This section presents an overview of the fundamentals of conventional theories related to flexure, shear, and bond, together with highlights of a selection of recently published papers that discuss the effect of corrosion on the overall behaviour of RC beams.

2.2.1 Bond behaviour in reinforced concrete beams

2.2.1.1 Theory of bond in reinforced concrete

In reinforced concrete, bond is defined as the flow of stress between the reinforcing steel and the concrete. Bond is necessary for ensuring composite action between the two materials; and thus provides the concept of RC theory. The approach based on load transfer between the steel and the surrounding concrete suggests that a bond could be form through three mechanisms: the chemical adhesion force between the bar and the concrete, the frictional force due to roughness and the relative slip between the bar and the surrounding concrete, and the bearing of the ribs against the concrete (ACI 408R).

The mathematical representation of the bond strength has been expanded over the years. It was first defined as a material property and represented as a function of the change in shear stress at the concrete steel interface over the length of the beam. According to the traditional method, bond strength is calculated as the difference in tensile force (ΔT) between two adjusted sections along a flexural member (Figure 2.4).

$$\Delta T = T_1 - T_2 = \frac{M_1}{jd_1} - \frac{M_2}{jd_2} \tag{2.8}$$

It can also be considered for a very small distance between sections:

$$dT = \frac{dM}{jd} \tag{2.9}$$

Therefore, the bond force per unit length U is defined as;

$$U = \frac{dT}{dl} = \frac{1}{jd} \cdot \frac{dM}{dx} \qquad (2.10)$$

Or as;

$$U = \frac{1}{jd} \cdot V \qquad (2.11)$$
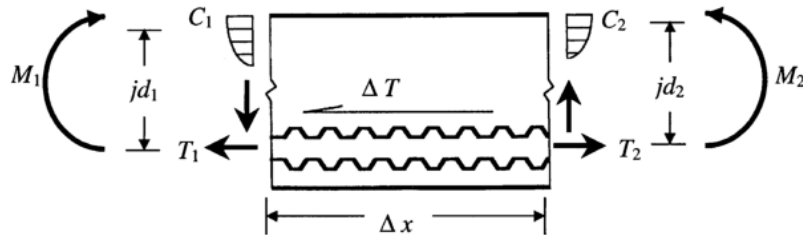
Figure 2.4: Variations in bar force due to changes in moment in a beam (ACI 408R)

Where;

ΔT : change in tensile force;

T_1, T_2 : tensile forces at two adjacent sections along the length of the member;

M_1, M_2 :bending moments at two adjacent sections along the length of the member;

jd_1, jd_2 : moment arms at two adjacent sections along the length of the member'

dx :change in length;

V : shear force in the section;

U : bond force at the section per unit length

Over time, based on numerous experimental studies, significant scatter between the calculated and the experimental bond stress results became clear and the mathematical concept for expressing bond strength has changed. Concrete cover, bar spacing, bar size, transverse reinforcement, bar geometry, concrete mix composition, steel stress and yield strength, bar surface condition, bar casting position, development and splice length, distance between spliced

11

bars, and concrete consolidation are all believed to be factors that affect bond strength in reinforced concrete beams. Consequently, bond strength is no longer just a material property. The updated mathematical representation is based on the fact that a change in force in a reinforcing bar is not solely a function of the applied load alone, but is also related to the force in the bar itself, which varies from a maximum value at cracks to a minimum value between cracks, where the steel transmits some of its stress to the surrounding concrete (Figure 2.5).

(a) Cracked concrete segment

(b) Bond stress in the reinforcing bar

(c) Variation in the tensile force in the steel

(d) Variation in the bond force along the bar
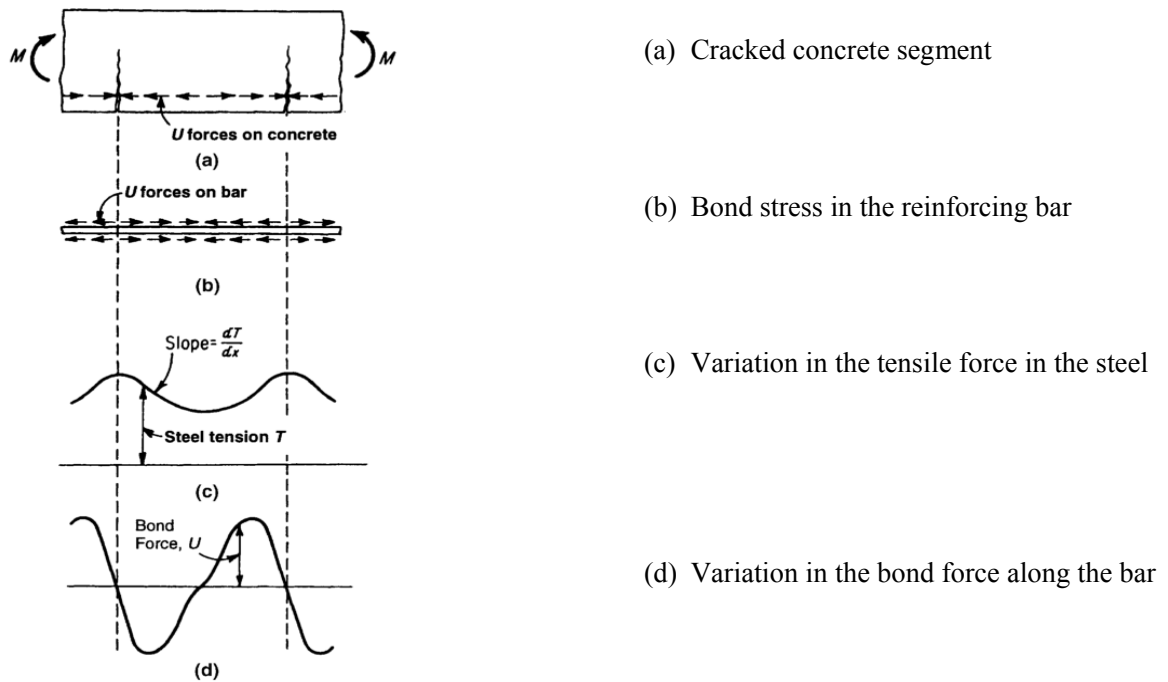
Figure 2.5: Variations in steel and bond forces in a reinforced concrete member subjected to bending (Nilson et al., 2004)

In fact, the use of the new mathematical concept of bond strength makes it impossible to predict the distribution of bond forces along the reinforcing bar because the locations of the flexural concrete cracks and the amount of steel stress shared with the concrete are unknowns. Therefore, all current mathematical bond models as well as the design codes are essentially empirical (ACI 408R).

FIB (2000) proposed a detailed model for defining the bond resistance mechanism of reinforced concrete; the model was developed based mainly on pull-out experimental results by

Tassios (1979). The model describes four different stages of the transfer of force between the reinforcing steel and the surrounding concrete (Figure 2.6):

- *Stage I (un-cracked concrete)*: This stage requires a bond stress in the range of $\tau \le \tau_1 = (0.2 - 0.8)f_{ct}$. The only key resistance in this stage is chemical adhesion; the stress is concentrated at the concrete lugs and no bar slip has occurred.

- *Stage II (first cracking):* This stage requires a bond stress of $\tau \ge \tau_1$, in which the chemical adhesion breaks down and the stress is resisted by the bearing force at the concrete lugs. This stage is characterized by microcracks at the concrete lugs, which produce a relatively small end-slip value.

- *Stage III*: This stage requires a bond stress value of $\tau \ge \tau_1 (1 - 3)f_{ct}$; and is characterized by the radial propagation of the longitudinal cracks, the crushing of the concrete on the front of the lugs, and the occurrence of considerable bar slip. The external bond stress is resisted primarily by the interlocking of the reinforcement. The end of this stage is distinguished by the extension of the longitudinal cracks to the outer surface of the concrete member (splitting).

- *Stage IVa*: This stage is specifies to plain reinforcement, in which only the friction is resisting the bond stresses.

- Stage IVb: The mechanism of this stage depends on the degree of confinement provided by the transverse reinforcement. If a light-to-medium amount of transverse reinforcement is available, the whole concrete cover breaks, and the member fails suddenly. If a sufficient amount of transverse reinforcement is available, the bond resistance is enhanced and the splitting failure is deferred. In this stage, the bond stress could be as high as $\left(\frac{1}{3} - \frac{1}{2} \right)f_c'$ and is associated with a large bar slip value.

- *Stage IVc*: In case of the use of heavy transverse reinforcement, high confinement prevents the occurrence of splitting failure, and the member fails through pull-out.

The bond stresses are resisted by the bearing force at the bar ribs and by the friction between the concrete and the reinforcement.

In the study presented in this thesis, this model was implemented for analyzing the bond-end slip behaviour of the test specimens in order to characterize the bond failure mode.
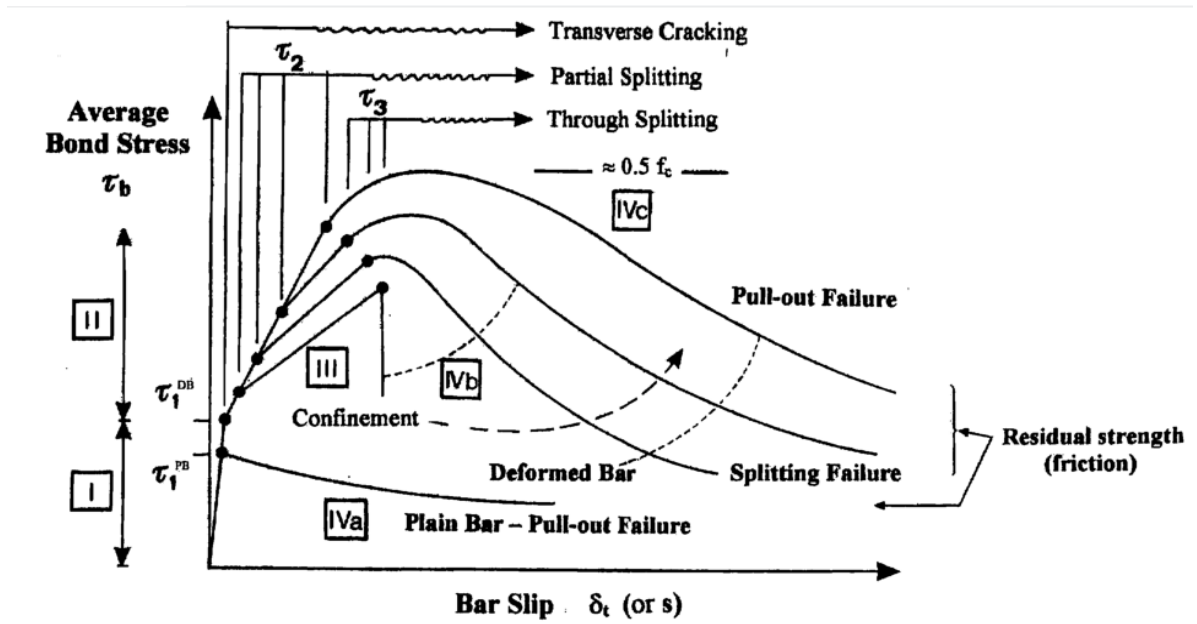
Figure 2.6: Bond strength mechanism in reinforced concrete (FIB, 2000)

2.2.1.2 Effect of corrosion on bond

The increase in volume resulting from the corrosion of the reinforcement in concrete initiates splitting stresses in the concrete, thus affecting the bond between the reinforcement and the concrete. Bond behaviour in corroded reinforced concrete has been studied experimentally and analytically by many researchers. Table 2.1 summarizes some of these studies and their specific categories. In the following a brief discussion of some of the key studies are presented.

Table 2.1: Summary of the literature related to the corroded reinforced concrete

Bond behaviour in corroded reinforced concrete		
Experimental work	**Empirical formulas**	**Analytical model**
• Al-Sulaimani et al. (1990)	• Cabrera (1996)	• Lundgren (2002)
• Rodriguez et al. (1994)	• Stanish et al. (1999)	• Coronelli 2002
• Cabrera (1996)	• Lee et al. (2002)	• Wang and Liu (2004)
• Almusallam et al. (1996-b)	• Chung et al. (2004)	• Maaddawy and Soudki (2004)
• Fu and Chung (1997)	• Bhargava et al. (2008)	• Khalfallah and Ouchenane (2008)
• Amleh and Mirza (1999)	• Wang and Liu (2010)	• Lundgren et al. (2012)
• Stanish et al. (1999)		
• Auyeung et al. (2000)		
• Lee et al. (2002)		
• Soudki and Sherwood (2003)		
• Chung et al. (2004)		
• Fang et al. (2004)		
• Craig (2004)		

Lundgren (2007) conducted a study of the effect of corrosion on the bond between the reinforcement and the concrete. The study includes a survey of the literature related to the experimental work together with the development of a finite element model. The model results agreed with the experimental findings. The study provided a summary of the effect of corrosion on the bond between steel and concrete based on the type of reinforcement, the deterioration in the concrete cover, and the existence of transverse reinforcement (Figure 2.7).
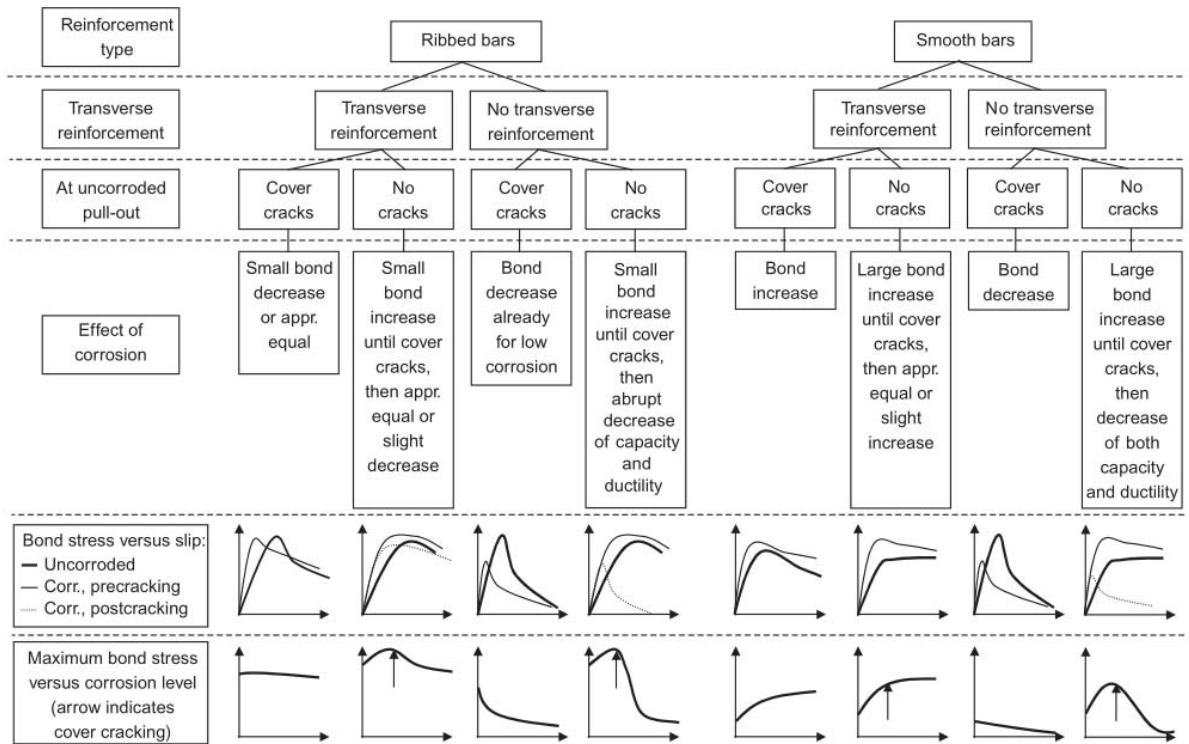
Figure 2.7: Summary of the effect of corrosion on bonding (Lundgren, 2007)

Bhargava et al. (2008) suggested an empirical formula for the estimation of the residual bond strength of reinforced concrete as a function of reinforcement corrosion. The formula was derived based on numerous previous experimental studies and on empirical models proposed by other researchers, all of which were related to the bond pull-out test and the bond-flexural test results. These experimental results reported in the literature were normalized in order to overcome the inconsistences in the test variables, such as the material properties, the specimen size and configurations, and the test setup and procedures (equations 2.12 and 2.13).

For the pull-out test, the reduction in bond strength due to corrosion is given as:

$$R = \begin{cases} 1.0 & \text{for } X \leq 1.5\% \\ 1.192e^{-0.117X} & \text{for } X > 1.5\% \end{cases} \tag{2.12}$$

For flexural bond testing, the reduction in bond strength due to corrosion is given as:

$$R = \begin{cases} 1.0 & \text{for } X \leq 1.5\% \\ 1.346e^{-0.198X} & \text{for } X > 1.5\% \end{cases} \tag{2.13}$$

Where;

R is the reduction in bond strength due to corrosion, and

X is the corrosion level (%).

The study also proposed a procedure for determining the flexural strength of the corrosion-damaged reinforced concrete beams that failed in bond (Equations 2.14-25). The predicted results were then compared to those collected from the experiments reported in the literature. The study showed that the proposed formula provides a reasonable estimate of the reduction in bond strength compared to both the experimental results and the empirical equations available in the literature.

The methodology used for calculating the residual capacity of corroded reinforced concrete beams is presented in Figure 2.8 and described by the following equations:

The tensile force in the corroded reinforcing bar is given as:

$$F_{tx} = n_{st}.\pi.D_{stx}.l_d.\tau_{bux} \tag{2.14}$$

The corresponding strain in the tensile steel rebar is given as:

$$\varepsilon_{stx} = \frac{F_{tx}}{A_{stx}.E_s} \tag{2.15}$$

The strains in the concrete and the compressive steel are given as:

17

$$\varepsilon_{ccx} = \frac{\varepsilon_{stx}.x_{ux}}{(d - x_{ux})}; \varepsilon_{scx} = \frac{\varepsilon_{stx}.(x_{ux} - d_{sc})}{(d - x_{ux})} \tag{2.16}$$

The total compressive force is given as:

$$F_{cx} = F_{ccx} + F_{scx} \tag{2.17}$$

Considering a parabolic stress-strain relationship for concrete, the force in concrete and its corresponding point of application are given as follows:

For $\varepsilon_{ccx} \leq 0.002$,

$$F_{ccx} = k.f_{ck}.b.x_{ux}\left[500\varepsilon_{ccx} - \left(\frac{250,000}{3}\right).\varepsilon_{ccx}^2\right] \tag{2.18}$$

$$Y_{cx} = x_{ux} - x_{ux}\left[\frac{\left(\frac{1,000}{3}\right) - 62,500\varepsilon_{ccx}}{500 - \left(\frac{250,000}{3}\right).\varepsilon_{ccx}}\right] \tag{2.19}$$

For $0.002 < \varepsilon_{ccx} \leq 0.0352$,

$$F_{ccx} = k.f_{ck}.b.x_{ux}\left[\frac{3\varepsilon_{ccx} - 0.002}{3\varepsilon_{ccx}}\right] \tag{2.20}$$

$$Y_{cx} = x_{ux} - x_{ux}\left[\frac{6\varepsilon_{ccx} - \left(\frac{0.000004}{\varepsilon_{ccx}}\right)}{12\varepsilon_{ccx} - 0.008}\right] \tag{2.21}$$

The force in the compression steel rebar is given as:

18

$$F_{scx} = \begin{cases} f_{scx}.A_{scx} = \varepsilon_{scx}.E_s.A_{scx} & \text{for } \varepsilon_{scx} \leq \left(f_y / E_s\right) \\ f_y.A_{scx} & \text{for } \varepsilon_{scx} > \left(f_y / E_s\right) \end{cases} \tag{2.22}$$

The flexural moment resistance of the beam for a given corrosion level is given as:

$$M_{ux} = F_{ccx}\left(d - Y_{cx}\right) + F_{scx}\left(d - d_{sc}\right) \tag{2.23}$$

(c) **Beam section**   (b) **Strain distribution**   (a) **Stress distribution**
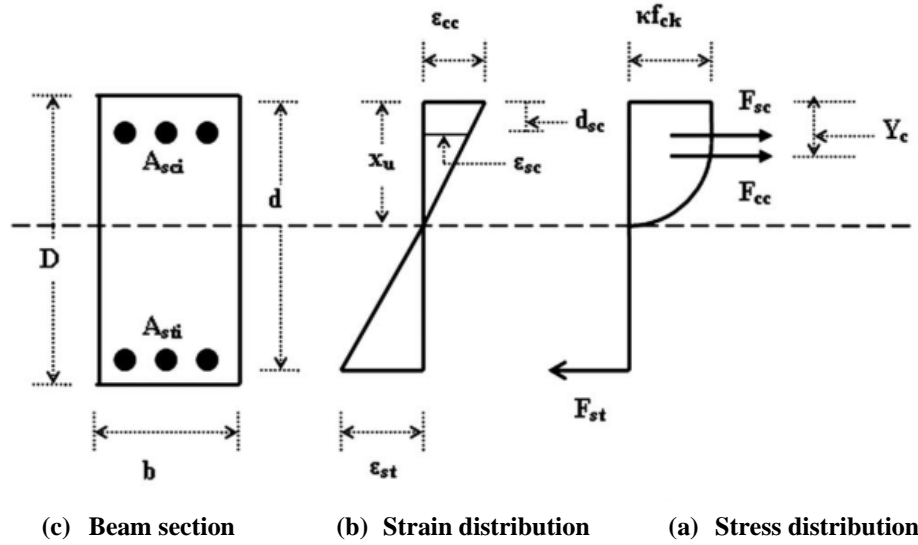
Figure 2.8: Derivation of the flexural strength of a corroded reinforced concrete beam (Bhargava et al., 2008)

Where;

F_{cx} : the tensile force in the corroded reinforcement;

n_{st} : the number of bottom tensile steel bars;

D_{stx} : the diameter of bottom tensile steel bars;

ld : the development length of the tensile reinforcement;

τ_{bux} : the bond strength at the corrosion level X;

ε_{stx} : the strain in the tensile strain;

A_{stx} : the area of tensile steel bar corresponding to corrosion level X;

A_{scx} : the area of the compression steel bars;

E_s : the modulus of elasticity for the steel;

ε_{ccx} : the strain in the concrete;

x_{ux} : the height of the compression zone corresponding to corrosion level X;

d : the distance between the centroid of the tensile steel bars and the edge of the compression zone;

d_{sc} : the distance between the centroid of the compressive steel bars and the edge of the compression zone;

F_{ccx} : the force of compression in concrete;

F_{scx} : the force in compressive steel bars;

b : the width of the beam section;

Y_{cx} : the point of application of F_{ccx} from the compression edge;

ε_{scx} : the strain in the compression steel bars;

f_{scx} : the stress in the compressive steel bars; and

f_y : the yield strength of the steel bars.

Auyeung et al. (2000) studied the bond behaviour of reinforced concrete by varying the level of corrosion in the reinforcing bars. The authors learned that a rapid decrease in bond strength is recorded at a corrosion mass loss of about 1 % (Figure 2.9). Bond strength degradation was non-linear with corrosion level.
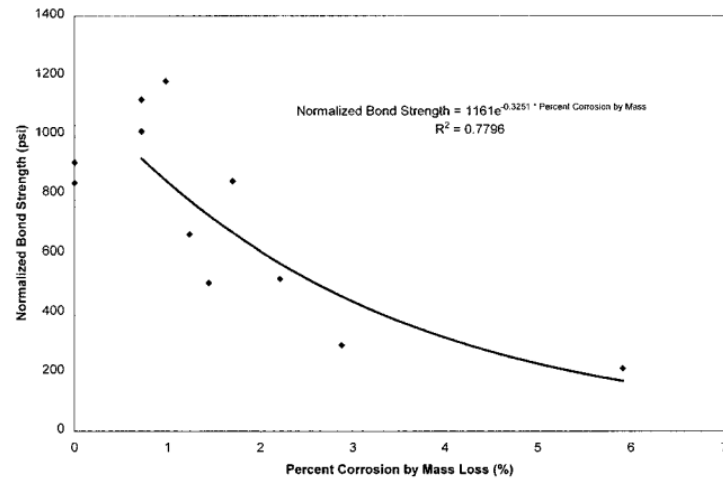
Figure 2.9: Influence of corrosion mass loss on bond strength (Auyeung et al., 2000)

The study also showed that the concrete cracks started to initiate around the corroded rebars at a corrosion level of about 2 % mass loss, after which a rapid increase in the level of corrosion could be observed. With respect to bar slip, the authors found that the bar exhibited a small amount of slip until the corrosion mass loss was about 2 %, after which the rate of slip increased with the reduction in the bond stiffness (Figure 2.10).
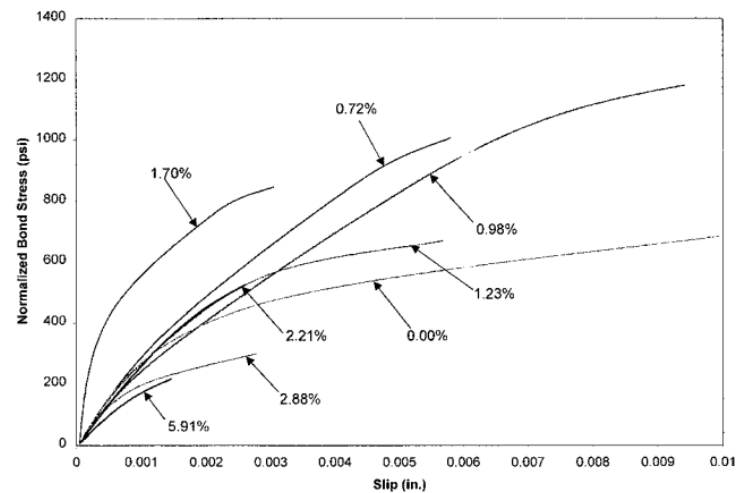
Figure 2.10: Effect of corrosion on bond-slip behaviour (Auyeung et al., 2000)

21

2.2.2 Flexural behaviour of reinforced concrete beams

2.2.2.1 Flexure theory

The principal flexural design criteria for reinforced concrete beams require that the factored moment resistance must be equal to or greater than the factored applied moment as follows:

$$M_r \geq M_f \qquad (2.24)$$

Where;

M_r : the factored moment resistance of the beam cross-section;

M_f : the factored moment due to applied load

Conventional section analysis based on force equilibrium and strain compatibility approach is widely used for analyzing the flexural behaviour of RC beams. This approach provides accurate predictions of the flexural capacity and moment-curvature behaviour. Figure 2.11 illustrates the stresses and forces operating in a cross-sectional of a rectangular RC beam (MacGregor and Bartlett, 2000).
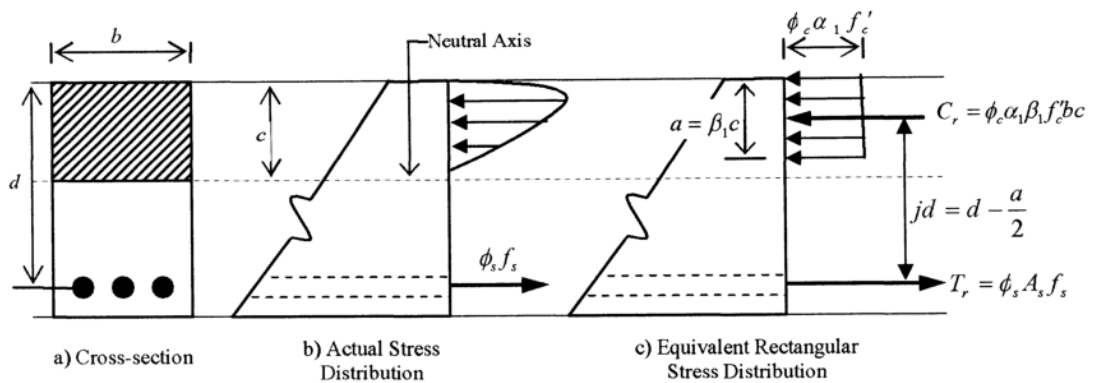
Figure 2.11: Stresses and forces in a singly reinforced rectangular beam (MacGregor and Bartlett, 2000)

Two common methods are used for approximating the analysis of RC beams. In the first method, an equivalent stress block approach is used in order to model the concrete in com-

22

pression where the actual stress-strain curve of the concrete is converted to an equivalent stress block using modification factors given by design codes. On the other hand, in the second method, a layered section approach is applied by dividing the cross-section of the RC beam into horizontal layers and calculating the strains and stresses in each layer based on strain compatibility and stress-strain relationships.

2.2.2.2 Effect of corrosion on the flexural behaviour of RC beams

The corrosion of the steel reinforcement in RC beams has been proven to reduce the load-carrying capacity and, in some cases, to change the structural response for the RC beams. Several researchers have investigated this problem and key studies are highlighted before.

Badawi and Soudki (2010) investigated the effect of shear-span and full-span corrosion of the longitudinal reinforcement on the structural performance of RC beams with hooked end anchorages. The experimental work included 15 RC beams: one control and 14 beams were corroded, seven of the 14 beams were repaired with CFRP laminates, and the other seven beams were kept un-repaired. Three levels of corrosion were chosen for the study: 5%, 10%, and 15% mass loss. The results showed that shear-span corrosion had almost no effect on the flexural capacity of the beams, whereas full-span corrosion reduced both the yield and the ultimate capacity by 23% and 12%, respectively. In general, corrosion increased the ductility of the unrepaired corroded beams due to the de-bonding of the corroded reinforcement. The repaired beams exhibited an increase in yield and the ultimate load of 19 % and 50 %, respectively compared to the control beam (Figure 2.12).
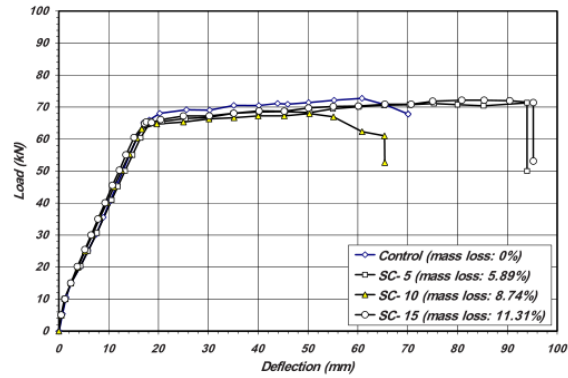
a) Shear-span corrosion
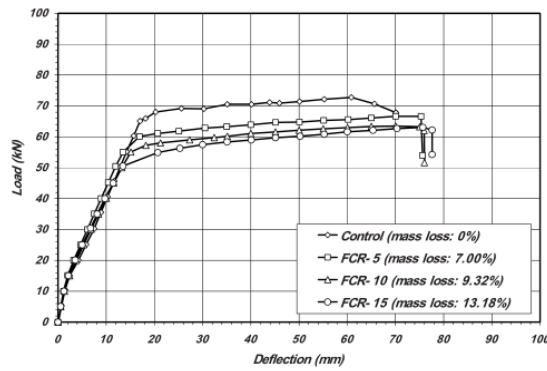
b) Full-span corrosion

Figure 2.12: Load-defection behaviour of unrepaired-corrosion specimens (Badawi and Soudki, 2010)

2.2.3 Shear behaviour of RC beams

2.2.3.1 Shear theory

For a simple beam subjected to a concentrated load (Figure 2.13), the concrete section above the neutral axis is in compression, while the section below the neutral axis exhibits tensile stresses. Farther away from the loading points, these tensile stresses create inclined shear stresses. If these shear stresses are relatively high, they can cause inclined cracks and eventual abrupt shear failure without advance warning (Figure 2.13). The stresses that cause the inclined cracks are known as diagonal tension stresses, and transverse reinforcing bars (stirrups) are added to RC beams to prevent failure caused by these stresses (MacGregor and Bartlett, 2000).

24
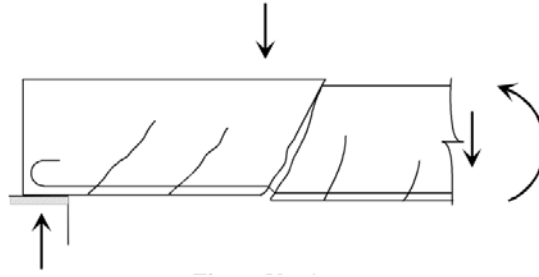
Figure 2.13: Diagonal shear cracks in a simple RC beam

The principles of shear design for RC beams stipulate that the intensity of the vertical shear is equivalent to the intensity of the diagonal tension. This premise simply means that designing for vertical shear forces addresses the resultant diagonal tension because of the weakness of the concrete in tension.

For a homogeneous elastic beam with stresses proportional to strains, the shear stresses can be obtained based on the principles of the mechanics of materials, as follows:

$$v = \frac{V.Q}{I.b} \tag{2.25}$$

where;

v : the shear stress at the section under consideration;

V : the shear force at the section under consideration;

Q : the moment of first moment of inertia about the neutral axis;

I : the moment of inertia of the cross-section about the neutral axis;

b : the width of the beam at the section under consideration.

2.2.3.2 Effect of corrosion on the shear behaviour of RC beams

Wang et al (2011) investigated the effect of localized corrosion damage in one shear-span with respect to the shear behaviour of RC beams. Fourteen RC beams were designed to fail in shear and were tested in a four-point bending configuration. Shear spans-to-depth ratios of 2 and 3 were selected, three types of partial lengths were used: 200 mm, 300 mm, and 450 mm; the partial length selected for the loading point started in the direction of the support. Three different bond characteristics were also considered within each designed partial length: complete loss of bond, moderate loss of bond, and substantial loss of bond. Banded polyfoam cubes were used to simulate complete loss of bond, while induced corrosion mass losses of 10 % and 25 % simulated moderate and substantial loss of bond, respectively. The test results showed that ductile behaviour and higher load capacity were exhibited by beams with lower shear-span-to-depth ratios. On the other hand, the beams with longer partial lengths showed greater ductility and larger load capacity (Figure 2.14). In addition, brittle failure mode was observed in the beams that had a higher corrosion level within a longer partial length rather than the ductile failure mode in the control beam (Figure 2.15).
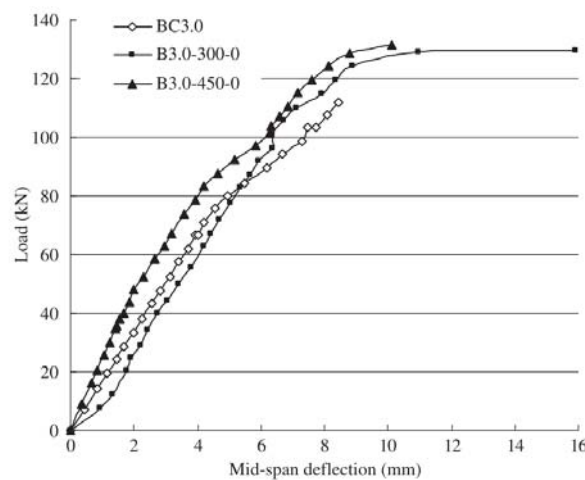
Figure 2.14: Comparison of the load-deflection curve of the normal control beam with those of beams that had partially un-bonded lengths (Wang et al., 2011)

26
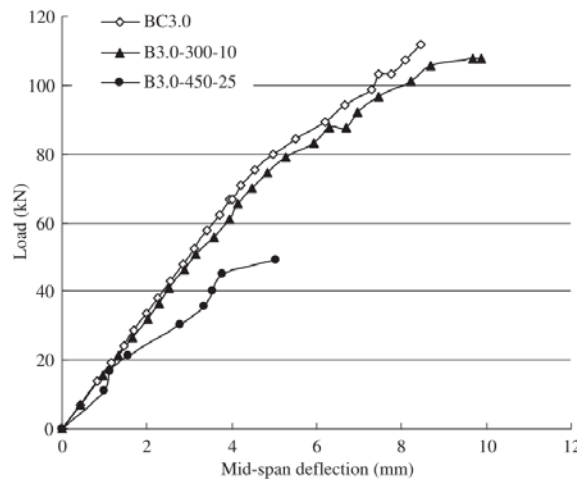
Figure 2.15: Comparison of the load-deflection curve of the normal control beam with those of typical beams that had the lowest and highest corrosion levels within the partial lengths (Wang et al., 2011)

2.3 Repair of Corroded RC beams

The structural behaviour of a RC member is compromised as deterioration occurs. When reinforcing steel bars are corroded, the pressure by corrosion produced at the steel-concrete interface causes cracking of concrete cover which leads to diminishing the bond between the steel and the concrete. In addition, the cross-sectional area of the steel reinforcement is also reduced as the corrosion increases. Eventually, the RC member can no longer withstand the stresses due to the applied loads. The premature failure of such a member must therefore be prevented through an effective monitoring system and the application of appropriate repair materials to the member in order to restore its original capacity.

Repair materials have generally been proven to enhance the structural performance of RC members. However, engineers find the selection of an appropriate repair material for a specific instance of deterioration challenging. Numerous studies have evaluated the performance and compatibility of a variety of available repair materials, yet no general agreement has been reached regarding the properties that should be considered in the evaluation of a repair material, such as dimensional stability, modulus of elasticity, thermal resistance, durability, compatibility, and strength.

Río at el (2005) conducted an experimental work to study the mechanical behaviour of patch repaired-corrosion-damaged RC beams. The study considered the effect of corrosion on loading crack patterns, load-bearing capacity, and the ductility of the patch repair. Twenty-four beams with two different steel configurations were constructed. Two beams with each configuration were kept as the control, and the remaining 22 beams were divided into two categories. Category I included 12 beams, in which corrosion was induced in the tension reinforcement at mid span. In the remaining 10 beams of category II, corrosion was induced in the compression reinforcement. Parts of the beams in both categories were repaired. Regardless of which reinforcement configuration was used (corroded tension steel or corroded compression steel bars), the induced corrosion led to a reduction in the cross-sectional area of the steel reinforcement. As a result, the cracking behaviour changed, and a reduction in the yield and ultimate capacities could be observed. The results were more pronounced in the case of category I, in which the tension steel was corroded. In the repaired beams, the yielding and ultimate load capacities are most likely slightly higher than in the corroded beams, but are still lower than in the control beams.

D'Ambrisi and Focacci (2011) investigated the effectiveness of fiber-reinforced cementitious matrix (FRCM) repair as a strengthening system for RC beams. Two different types of RC beams were considered: long beams (25 beams) and short beams (10 beams). The beams had different geometries and loading setups: the long beams were tested in a four-point bending configuration, and the short beams were tested in a three-point-bending configuration. Three different composite repair systems were used for the study: two fibers with a bidirectional sheet, and one fiber with a unidirectional sheet. All types were embedded in a cement-based matrix during application on the beams. The test results show that the FRCM materials increased the load-carrying capacity of the RC beams. The failure mode of the strengthened beams was characterized by the de-bonding of the composite sheets at the interface with the concrete beams. The study confirmed that the use of the FRCM-strengthening materials could change the failure mode of RC beams, especially in the case of concrete with low compressive strength. The findings also revealed that the performance of FRCM materials was largely dependent on the design of the matrix and on the composite action with the RC

beams. The performance of FRCM materials; could not be predicted based on common mechanical properties.

2.4 Modeling the Bond Behaviour of Corroded Reinforced Concrete

In practical terms, a perfect bond between reinforcing steel bar and concrete occurs only in un-cracked zones, where almost no stress is transferred between the steel bar and the concrete. However, in cracked zones, in which a high degree of stress transfer exists between the steel bar and the concrete, the compatibility of the strains is not valid. In such cases, the bond stresses are controlled by the relative displacement between the reinforcing steel bar and the surrounding concrete. The relation between the bond stresses and the relative displacements between the steel bar and the concrete in incompatibility conditions is known as bond-slip (Figure 2.16).
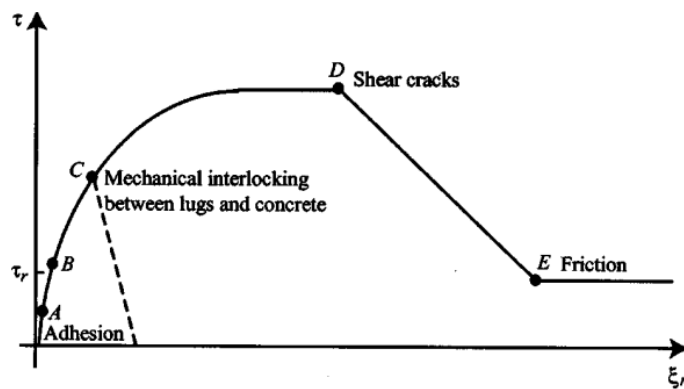
Figure 2.16: Typical bond stress-slip relationship (Girard and Bastien, 2002)

2.4.1 Modeling bond-slip for corroded reinforcement

Lundgren et al. (2012) reformulated the bond-slip constitutive one-dimensioned model provided by the CEP-FIP model code (1990) by employing the theory of plasticity. This change enabled the model to take into account both the effect of corrosion on the reinforcing bars and the effect of cyclic loading. The model is described as follows:

The bond stress is assumed to follow an elasto-plastic law;

$$\tau = D(s - s_P) \tag{2.26}$$

$$|\tau| \le \tau_b(k) \tag{2.27}$$

The bond strength curve equations are as follows;

$$\tau_b(k) = \left(1 - \left(1 - 2\frac{k}{s_1}\right)^2\right) * \tau_{max} \qquad ,0 \le k < \frac{s_1}{2} \tag{2.28}$$

$$\tau_b(k) = \tau_{max} \qquad ,\frac{s_1}{2} \le k < s_2 - \frac{s_1}{2} \tag{2.29}$$

$$\tau_b(k) = \tau_{max} - (\tau_{max} - \tau_f) * \left(\frac{k - s_2 + \frac{s_1}{2}}{s_3 - \frac{\tau_f}{D} - s_2 + \frac{s_1}{2}}\right) \qquad ,s_2 - \frac{s_1}{2} \le k < s_3 - \frac{\tau_f}{D} \tag{2.30}$$

$$\tau_b(k) = \tau_f \qquad ,s_3 - \frac{\tau_f}{D} \le k \tag{2.31}$$

For interpolation between the confined and the unconfined case;

$$\tau_b = k_{unconf}.\tau_{b,conf} + (1 - k_{unconf})\tau_{b,unconf} \tag{2.32}$$

For interpolation between the corroded and the un-corroded case;

$$\tau_b = k_{corr}.\tau_{b,conf} + (1 - k_{corr}).\tau_{b,unconf} \tag{2.33}$$

Where;

τ: the bond stress in the steel reinforcement;

D: bond stiffness;

s: bar slip;

s_p: plastic slip;

τ_b: the bond strength;

k: the hardening parameter;

$s_1, s_2, s_3, \tau_f,$ and τ_{max}: the model parameters;

k_{uconf}: the confinement factor;

k_{corr}: the corrosion factor.

2.5 Modeling the Flexural Behaviour of Beams with Corroded Reinforcement:

The flexural behaviour of RC beams is usually defined based on the load-deflection relationship, which can be described as having two main stages: a linear stage, which represents the loading stage up to the yielding point of the steel reinforcement, and a non-linear stage, which represents the loading stage between the yielding point of the steel reinforcement and the point at which the crushing of the concrete occurs.

The load-deflection relationship can be modeled either partially up to the yielding stage (linear) or as a full curve that includes the pre-yielding and ultimate stages (non-linear). Semi-empirical methods based on the effective moment of inertia of the beam cross-section are commonly used to determine the load-deflection relationship of RC beams in a linear manner, whereas more complicated numerical methods, such as finite elements, are used to represent the relation in a non-linear manner.

The flexural stiffness EI of the RC beam during loading is given as a product of two variables: the moment of inertia I which represents the cross-sectional resistance to the applied load, and the modulus of elasticity E which represents the resistance of the material to applied load. The variation in the moment of inertia can be explained based on the ineffectiveness of cracked concrete areas resisting applied stresses, which leads to greater deformations in the beam as the load is increased, while the variation in the modulus of elasticity can be attributed to the inelastic stress-strain behaviour of the concrete in the plastic range. The effective moment of inertia approach involves only the decrease in the moment of inertia with increasing load (Kalkan, 2010). Two methods are commonly used to determine the load-deflection curve based on the moment of inertia approach: the layered method, and the effective moment of inertia method. Both methods are based on the same concept of the effective moment of inertia but differ in the way in which the effective moment of inertia is calculated.

31

The effective moment of inertia concept is used for determining beam deflection according to the elastic theory of structural analysis, and the mid-span deflection of the beam can thus be calculated as follows:

$$\Delta = \frac{P.L^3}{48E_c.I_e} \tag{2.34}$$

Where;

Δ: the mid-span deflection;

P: the applied load at the mid-span;

L: the beam length;

E_c: the modulus of elasticity of concrete;

I_e: the effective moment of inertia.

In the layered method, the effective moment of inertia is represented as a function of the neutral axis c of the beam cross-section and is calculated using the simple-beam-bending theory:

$$E_c I_e = \frac{M}{\phi} \le E_c I_g \tag{2.35}$$

$$\phi = \frac{\varepsilon_{top}}{c} \tag{2.36}$$

where;

E_c: the modulus of elasticity of concrete;

M: the moment due to the applied load;

I_e: the effective moment of inertia;

I_g: the gross moment of inertia;

c: the neutral axis of the beam cross-section;

ϕ: the curvature; and

ε_{top}: the top concrete strain.

In the effective moment of inertia method, a semi-empirical equation first proposed by CSA A23.3-04 (CSA, 2004) is used to average the moments of inertia of the un-cracked and fully cracked portions of a concrete beam:

$$I_e = I_{cr} + \left[\left(I_g - I_{cr} \right) \left(\frac{M_{cr}}{M_a} \right)^3 \right] \leq I_g \qquad (2.37)$$

where;

I_g: the gross moment of inertia;

I_{cr}: the cracking moment of inertia;

M_a: the moment due to applied load; and

M_{cr}: the cracking moment.

2.6 Summary

The main information presented in this chapter can be summarized in the following points:

1. There is a lack of guidelines or limitations regarding the concrete crack widths due to corrosion of steel reinforcement.

2. The structural behaviour of RC beams with full-span corroded reinforcement has been intensely researched experimentally and theoretically, however very limited studies have been conducted with respect to RC beams with localized corroded rein-forcement.

3. There is a lack of equations, design guidelines and codes with respect to the prediction of the residual capacity and the service life of the RC elements with localized corrosion damage.

4. Limited research have been published with respect to the application of the FRCM repair system on the damaged RC beams.

5. There is a lack of design guidelines regarding the application of the patch repair in the bond-damaged zones due to corrosion of steel reinforcement in concrete.

6. No mathematical models have been proposed to predict the structural behaviour of RC beams with localized corroded reinforcement.

This literature has revealed a lack of information regarding the behaviour and repair of RC beams with localized corroded reinforcement. Therefore, it is important to study such a subject.

Chapter 3
Experimental Program

3.1 Introduction

This chapter presents the details of the experimental program, including a description of the test specimen, the specimens` fabrication, the material properties, the accelerated corrosion technique, the repair techniques, the instrumentation, the load setup and test procedure.

The experimental program consisted of testing 15 medium-scale reinforced concrete beams with corroded tension steel rebars in the shear-span and different repair scenarios. The main test parameters were:

1) The corrosion level: 0 %, 2.5 %, 5 %, 7.5 % and 15 % theoretical mass loss
2) The repair technique and materials: fiber reinforced cement-based composite and concrete patch
3) The depth-to-span ratio: 3.4 and 2.4
4) The end anchorage condition: bonded or un-bonded.

3.2 Test Program

This experimental program comprised of testing 15 medium-scale reinforced concrete beams (150 mm x 350 mm x 2400 mm) under static loading. Fourteen specimens were corroded, and one specimen was kept un-corroded as a reference. Table 3.1 summarizes the test matrix and Figure 3.1 shows a flowchart of the test program. The test specimens were divided into two main groups based on the loading-support condition and the span-to-depth ratio. Two span-to-depth ratios were selected: 3.4 with three-point bending and 2.4 with four point bending. Each group of specimens was subdivided based on the degree of corrosion and the condition of the end anchorage. Two end-anchorage conditions were chosen: specimens with end anchorages that were designed to fail in flexure, in which the anchorage zone was bonded, and specimens with no end anchorages that were designed to fail in bond, in which

the end anchorage zone was intentionally un-bonded through the use of an aluminum tube placed around the reinforcement.

Four degrees of corrosion were chosen to simulate of minor, medium and severe mass losses in the steel rebar. Reinforcement mass losses of 2.5 % and 5 % were used in one beams for each as definitions of minor degrees of corrosion. A reinforcement mass loss of 7.5 % was used in 6 beams as an indication of a medium degree of corrosion, and a mass loss of 15 % identified a severe corrosion level in 6 beams.

Three repair scenarios were used. The first repair involved U-wrapping of the deteriorated zone with two types of commercial fiber systems: a glass-fiber reinforced cement-based matrix (GFRCM) and a carbon-fiber reinforcing cement-based matrix (CFRCM). The second repair scenario was a patch repair, which includes the removal of the deteriorated concrete, the cleaning of the reinforcing steel, and the application of a commercial patch material. The third scenario involved U-wrapping and Patch repair. The application process conformed to the specifications given in the material data-sheets provided by the suppliers.

Table 3.1: Test matrix

Beam	Depth to span ratio (a/d)	Mass loss (%)	Anchorage condition	Repair scenario
A-C0%-U-3B	3.4	0	anchored	none
A-C2.5-U-3B	3.4	2.5	anchored	none
A-C5-U-3B	3.4	5	anchored	none
A-C7.5-U-3B	3.4	7.5	anchored	none
N-C7.5-U-3B	3.4	7.5	Non-anchored	none
A-C7.5-U-4B	2.4	7.5	anchored	none
N-C7.5-U-4B	2.4	7.5	Non-anchored	none
N-C7.5-R(GFRCM)-4B	2.4	7.5	Non-anchored	U-wrapping
N-C7.5-R(P)-4B	2.4	7.5	Non-anchored	Patch
N-C15-U-4B	2.4	15	Non-anchored	none
N-C15-R(GFRCM)-4B	2.4	15	Non-anchored	U-wrapping
N-C15-R(CFRCM)-4B	2.4	15	Non-anchored	U-wrapping
N-C15-R(P)-4B	2.4	15	Non-anchored	Patch
N-C15-R(P+GFRCM)-4B	2.4	15	Non-anchored	Combined
N-C15-R(P+CFRCM)-4B	2.4	15	Non-anchored	Combined

Specimen designation:

First letters: A or N refers to the bonded end zone specimens and the un-bonded end zone specimens.

Second letter/number: C# refers to the corrosion levels: 0 %, 2.5 %, 5 %, 7.5 % and 15 % mass loss.

Third letter: U refers to the unrepaired specimens, and R refers to the repaired specimens. The specific repair scenario is given in brackets. GFRCM indicates specimens-wrapped with glass-fiber-reinforced cement-based composite. CFRCM indicates specimens-wrapped with carbon-fiber-reinforced cement-based composite. P indicates specimens repaired with the use of a concrete patch.

Last letter: B refers to the loading configuration: a 3B represents 3-point-bending load configuration with an a/d of 3.4, and 4B represents a 4-point bending load configuration with an a/d of 2.4.
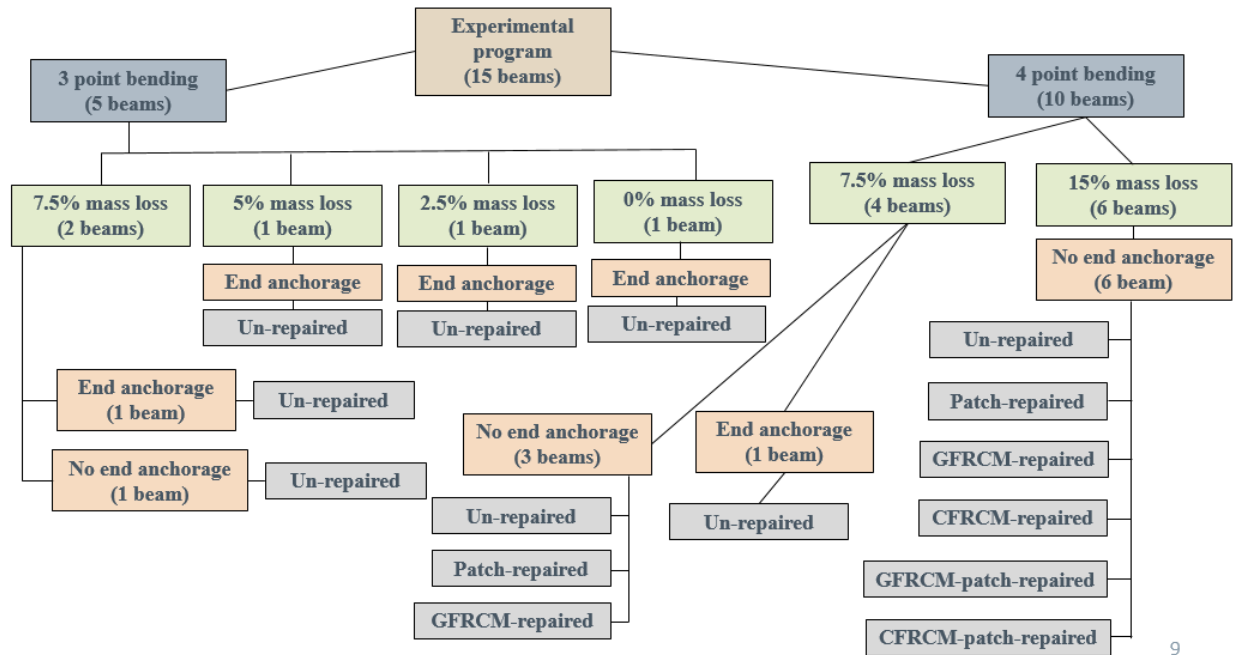
Figure 3.1: Flowchart of the experimental program

3.3 Specimens` Configuration

Figure 3.2 shows the specimen configuration and reinforcement details. All beams had the same geometry: a rectangular cross-section 350 mm deep by 150 mm wide, and a length of 2400 mm. Each beam was reinforced with two 25M deformed bars (bottom reinforcement) with a clear cover of 40 mm from the bottom and 25 mm from the sides. Two 10M deformed bars were used as top reinforcement with a cover 30 mm from the top and 25 mm from the sides. The shear reinforcement consisted of 10M epoxy coated stirrups (epoxy was used for corrosion protection) at a spacing of 200 mm c/c. A hollow 8 mm-diameter stainless steel bar was placed at a distance of 90 mm from the bottom of the specimen to act as the cathode in the accelerated corrosion circuit. The stainless steel bar was placed in all specimens. Both the bottom reinforcement bars and the stainless steel tube were extended 100 mm from one end of the beam in order to provide sufficient length for the connection of the electrical circuit.

During casting, NaCl (deicing salt) was added to the concrete in one shear span of the specimens in order to ensure localized corrosion of the bottom rebar. As shown in Figure 3.3, the salted shear zone had a length of 1000 mm and a height of 110 mm from the bottom face of the specimen. The reinforcing stirrups were epoxy coated to ensure that they were electrically insulated from the main rebars, and the corners of the stirrups (intersection points between the stirrup and the bottom rebars) were covered with electrical insulation tape, as illustrated in Figure 3.4.
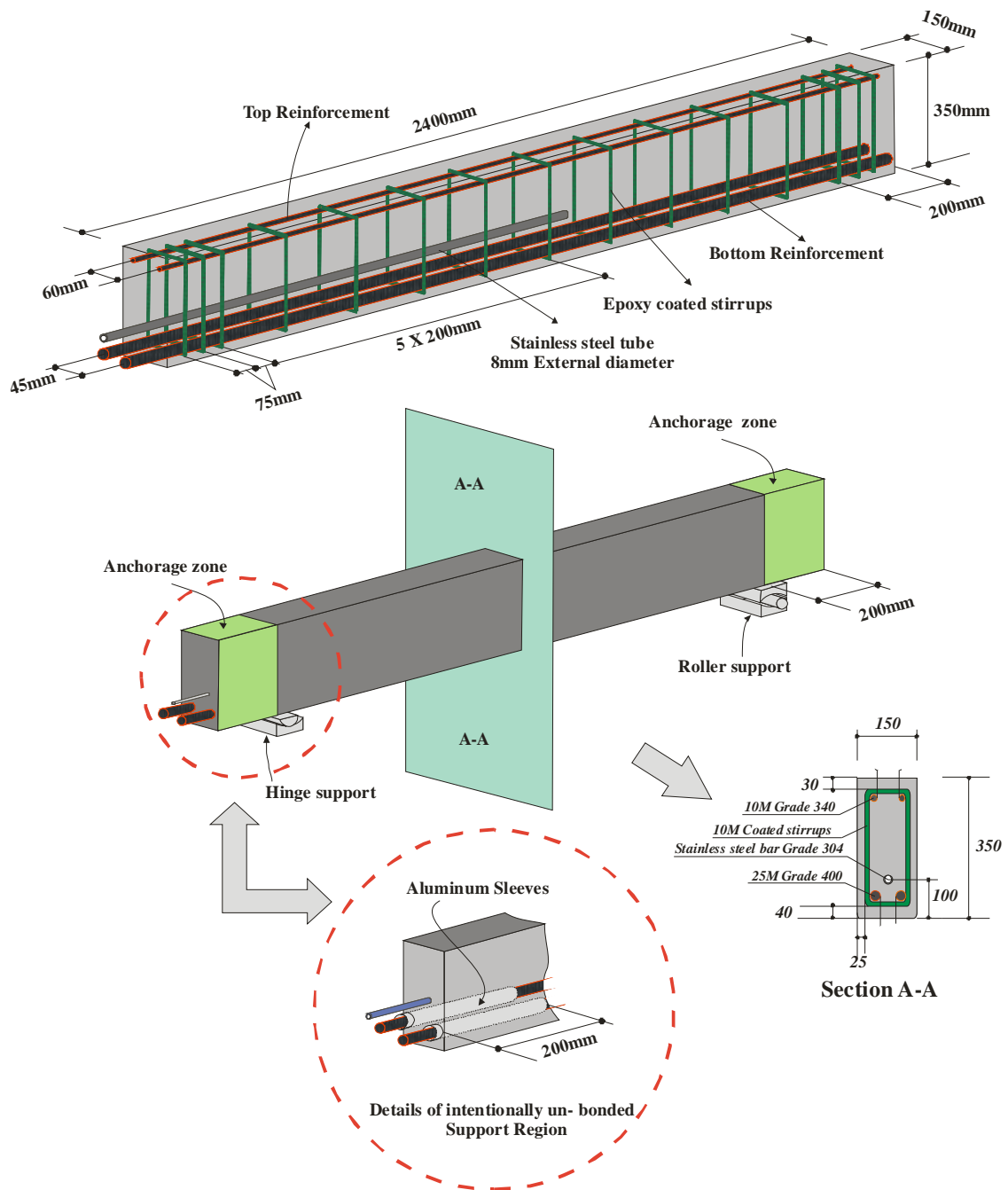
Figure 3.2: Specimen configuration and reinforcement layout (all dimensions in millimeters)

Top Reinforcement

2400mm

150mm

350mm

200mm

Bottom Reinforcement

Epoxy coated stirrups

60mm

5 X 200mm

Stainless steel tube
8mm External diameter

45mm

75mm

Anchorage zone

A-A

Anchorage zone

A-A

200mm

Roller support

Hinge support

Aluminum Sleeves

200mm

Details of intentionally un- bonded
Support Region

150

30

10M Grade 340

10M Coated stirrups

Stainless steel bar Grade 304

25M Grade 400

350

100

40

25

Section A-A

Figure 3.3: Salted concrete zones

Figure 3.4: Protection and insulation of stirrups

3.4 Formwork

Fifteen wooden forms were constructed. Each formwork consisted of the following compo-
nents, as shown in Figure 3.5:

- A steel channel (C-section) was used as the base, with cross-section of 152 mm x 50.8 mm x 50.8 mm and a length of 3048 mm.
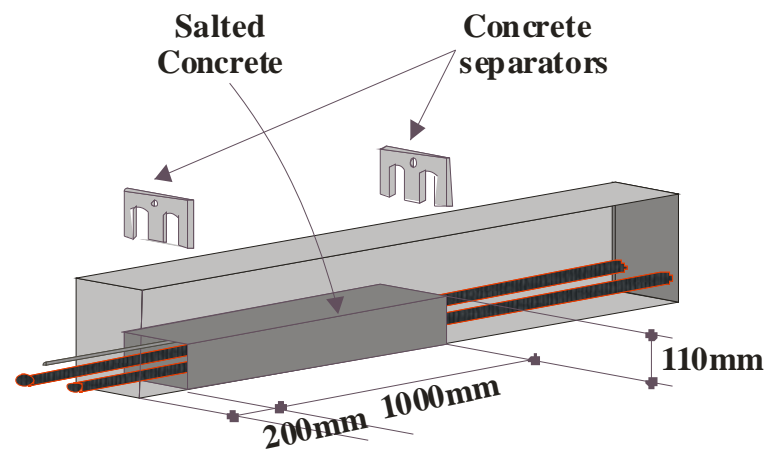
- Two wooden sides measuring 1220 mm long by 406 mm high by 25.4 mm thick, with 20 holes for bolts, each bolt was 10 mm in diameter and 280 mm long, which were used to tighten the sides to the base

- Two wooden end blocks (406 mm long by 152 mm wide by 38 mm thick) that were fastened to the wooden sides at both ends of the C-channel

- Two steel angles with 76 mm x 76 mm cross-section and a length of 1220 mm, were fixed along the length of the top edges of the wooden sides, one on each edge, in or-der to provide reinforcement against the horizontal pressure of the plastic concrete

- Three steel plates (50.8 mm by 203 mm), that were used as braces across the width of the form, and as a means of hanging the steel cages to provide the specified con-crete covers
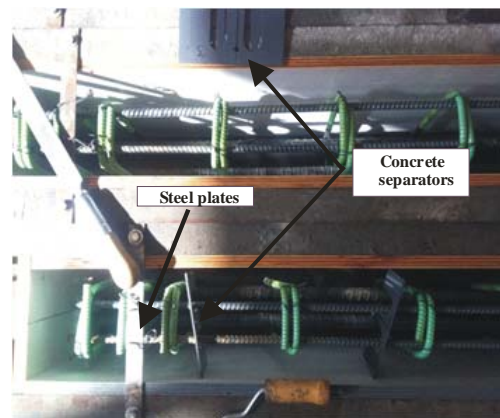
| (a) Side view | (b) Top view |

Figure 3.5: Forms and steel cages prior to concrete casting

3.5 Concrete Mix Design and Placement

Ready-mix concrete was supplied by two trucks: one with one cubic meter of concrete and another with two cubic meters of concrete. The mix proportions, per cubic meter, were 290 kg of Portland cement, 1125 kg of pea stone (13 mm maximum aggregate size), 865 kg of sand, 60 kg of NewCem +(70/30 % blend of slag and flyash), and 160 liters of water: resulting in a water-cement ratio of 0.457. An additional 30 kg of salted water was added to the first truck, and 60 kg of regular water was added to the second truck in order to produce a water-cement ratio of 0.55. In the salted water, an amount of 11 kg of deicing salts (NaCl) was mixed with the 30 kg of water to produce a 2.15 % chloride (Cl$^-$) by weight of cement, which is above the threshold value for depassivating the 2-25M rebar and accelerating the corrosion.

Throughout the placement of the concrete, rigid plastic dividers 110 mm deep and 150 mm wide were used to separate the salted zone from the unsalted concrete in the rest of the beam (See Fig. 3.3). First, salted concrete was placed in the shear zone of the fifteen corroded beams (1000 mm long by 110 mm high), then the unsalted concrete was placed in the remaining part of each beam. Once the top part of the beam was filled with unsalted concrete, the plastic dividers were removed. The specimens were cured for one week under wet burlap and plastic sheets. For both batches, the average 28-day compressive strength was 49 MPa.

3.6 Steel Reinforcement

The steel reinforcing bars conformed to CSA Standard. The yield strength of the 25M bars and the 10M reinforcing bars was 460 MPa, and the ultimate strength was 580MPa. The yield strength of the reinforcing stirrups was 320 MPa.

3.7 Repair Material and Application Procedure

Three types of repair materials were used: a glass-fiber reinforced cement-matrix (GFRCM), manufactured by SIKA Inc.; a carbon-fiber reinforced cement-matrix (CFRCM), manufac-

tured by SGL GROUP Inc.; and a self-compacting concrete patch manufactured by SIKA Inc.

3.7.1 Composite Material

Two composite FRCMs were used as external wrapping repair systems. Each system was composed of two major constituents: fiber grid and a matrix (Figure 3.6). The reinforcing fiber grids in the first system were a glass fiber grid (Sika Wrap-350G), manufactured by Sika Canada, Inc.; the second system, a SIGRATEX® Grid, was a carbon fiber grid manu-factured by SGL Group, Inc. For both systems, the grid size was 30 mm by 30 mm, with a width of 2 mm and a thickness of 0.25 mm. The matrix was a conventional cement matrix (Sika®MonoTop®-623 Mur), manufactured by Sika Canada, Inc., as the bonding agent that adheres the glass and the carbon-fibre grids onto the concrete substrate. Tables 3.2, 3.3, and 3.4 give the mechanical properties of the dry fibers and the composite, as provided by the manufacturers.

Seven corroded beams were repaired using FRCM and/or patch. Five of the seven were U-wrapped with externally bonded single layer bi-directional fiber-reinforced cement-based matrix (FRCM): three beams were wrapped with glass-FRCM (GFRCM), and two beams were wrapped using carbon-FRCM (CFRCM). The other repair scheme utilized involved confining the entire span of the repaired beam (Figure 3.8). Two of the five were repaired with patching before application of the FRCM wrapping. The other two of the seven were repaired with patch without wrapping (Figure 3.7).

(a) Glass-fiber reinforced cement-based composite matrix (GFRCM)

(b) Carbon-fiber reinforced cement-based composite matrix (CFRCM)

(c) Sika®MonoTop®-623 Mur cement

Figure 3.6: Fibre-reinforced cement composite components

Table 3.2: Mechanical properties of the dry glass and carbon fibers (as reported by manufactures)

Fiber Name and Description	Fiber Properties (Dry Condition)			
	Ultimate Strength (MPa)	Modulus of Elasticity (MPa)	Ultimate Elongation (%)	Density (g/cm^3)
SIGRATEX grid: bi directional carbon-fiber reinforced grid	1671	23000	1.25-1.6	N/A
Sika Wrap-350G Grid (glass-fiber reinforced-grid)	3400	75000	2.8	2.56

Table 3.3: Mechanical properties of the resin (as reported by manufactures)

Resin Name and description	Resin Properties (Dry condition)		
	Ultimate Strength (MPa)	Modulus of Elasticity (MPa)	Ultimate Elongation (%)
Mono Top-722 Mur (fiber-reinforced cementitious mortar)	Compression 22.1 Flexural 6.7 Bond 1.88	8000	-

Table 3.4: Mechanical properties of the composites after curing (as reported by manufactures)

Composite	Composite Properties (After Curing)				
	Ultimate Strength (MPa)	Modulus of Elasticity (MPa)	Ultimate Elongation (%)	Areal Weight (g/m^2)	Thickness (mm)
GFRCM	45KN/m both directions	-	2	350	6 - 10
CFRCM	-	-	-	-	6 - 10
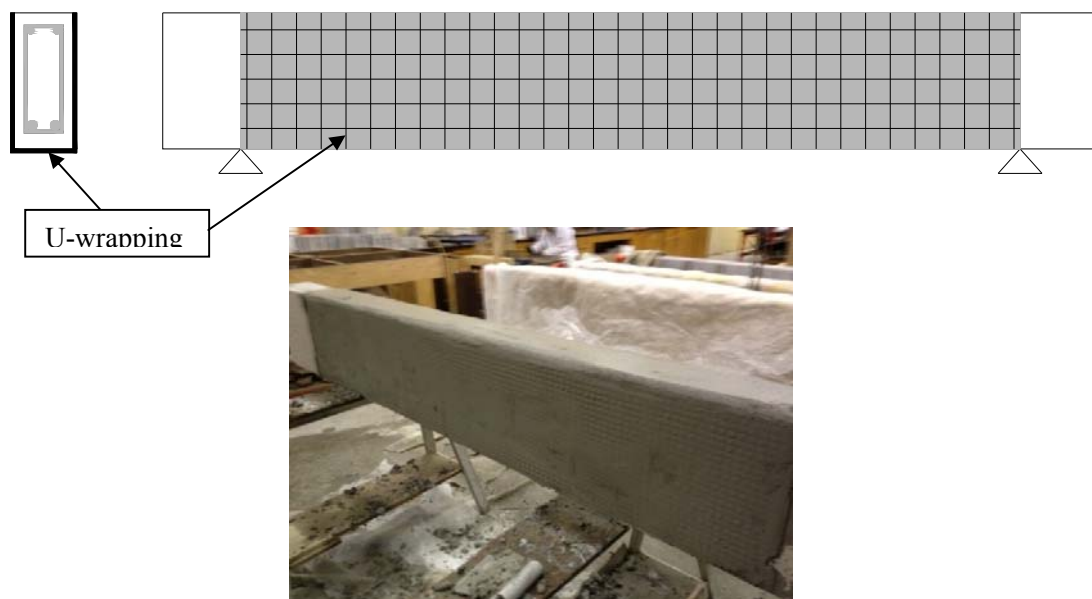
U-wrapping

Figure 3.7: Wrapping scheme

Prior to FRCM repair, the concrete surface was prepared according to the following steps: the edges of the beam were rounded using a concrete grinder as means of obtaining smooth angles in order to avoid stress concentration; the concrete surface was then sandblasted in order to remove the dust products, and the dust was removed using a compressed air line (Figure 3.8).

Figure 3.8: Surface sandblasting

Prior to the application of the FRCM, the concrete surface was saturated with water; the first layer (4 mm thick) of the cement paste was applied to the surface, and the corrosion cracks were sealed with the cement paste. The fiber grid was installed (U-wrapping) within the first cement layer, following which the second layer (2 mm thick) of the cement paste was applied. The surface was finished, leveled, and cured for three days. The repaired beams were tested seven days after the application of the composite FRCM. Figure 3.9 shows the wrapping stages.
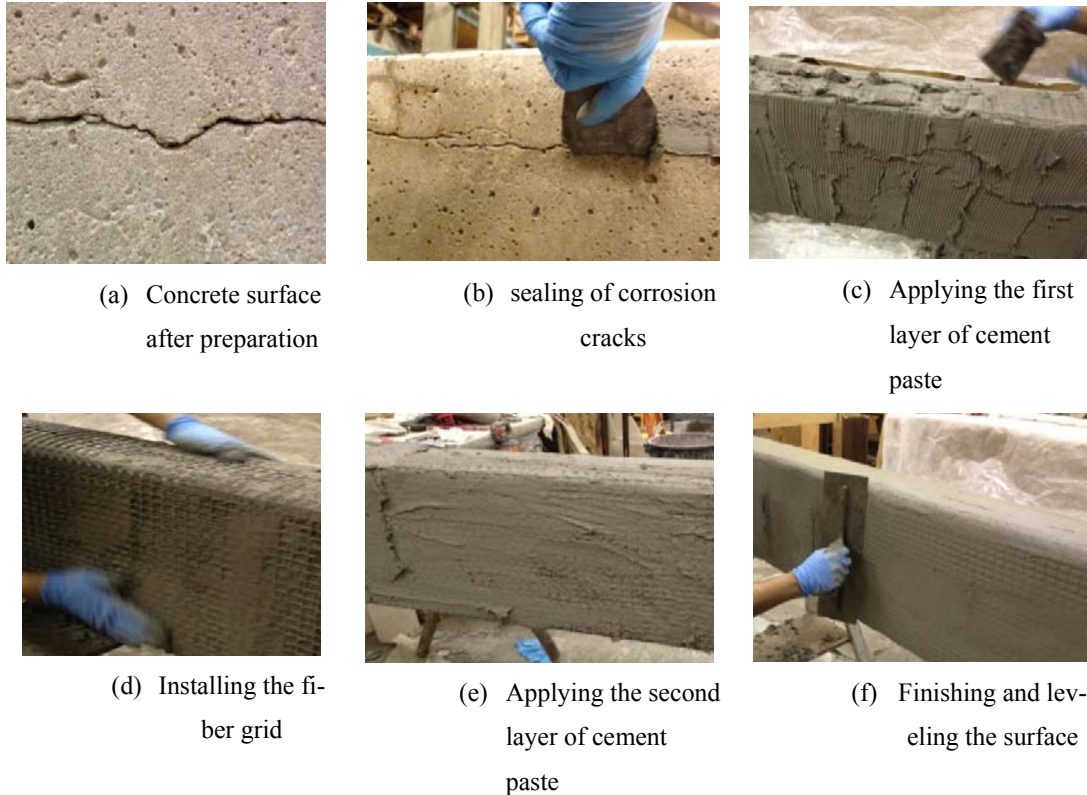
(a) Concrete surface after preparation	(b) sealing of corrosion cracks	(c) Applying the first layer of cement paste
(d) Installing the fiber grid	(e) Applying the second layer of cement paste	(f) Finishing and leveling the surface

Figure 3.9: Wrapping with composite FRCM systems

3.7.2 Patch material

Self-consolidated ready-to-use cement-based fine concrete (Sika-Crete-08) manufactured by Sika Canada, Inc. was used as a patch material for replacing the deteriorated concrete. Based on the manufacture's specifications and the recommendations provided by the Concrete Repair Guide (ACI 546R-04), the patch repair was applied on four specimens. The stitch drilling method specified by ACI 546R-04 was selected for the removal of the deteriorated concrete in the specimen. A Hilti hammer drill, TE6S manufactured by Hilti Canada Corporation, was used to drill small holes along the deteriorated zone in order to weaken the concrete locally. As recommended by ACI 546-04 and shown in Figure 3.10, with the use of hand chisel and a hammer, the deteriorated concrete was then removed smoothly to a depth of 150 mm from the bottom of the beam, allowing a minimum of 20 mm behind the tension steel rebar in the deteriorated zone.

A wire brush was used to remove the concrete from the surface of the steel rebar, following which the target area was sandblasted as recommended by the ACI 546-04. The surface of the concrete was saturated prior to the application of the repair patch. The patch material was mixed and poured according to the manufacturer's specifications, and the specimens were then cured for 15 days. Figure 3.10 shows the process of removing the deteriorated concrete and applying the patch repair. Table 3.5 lists the mechanical properties of the patch concrete.

Table 3.5: Patch material properties as supplied by the manufacturer

Patch Name and Description	Patch Properties			
	Ultimate Strength (MPa)	Bond Strength (MPa)	Mixing Time (min)	Application Time(min)
Sikacrete®-08 SCC (self-compacting concrete)	45	2.5	2 - 2.5	25 - 30

(a) Deteriorated zone

(b) Drilled holes along the deteriorated zone

(c) Beam after concrete removal

(d) Beam after concrete patch

Figure 3.10: Concrete removal and patch repair application

3.8 Induced Corrosion

The theoretical mass loss induced in the steel rebar was estimated based on Faraday's law as follows:

$$m = \frac{I.t.a}{ZF} \tag{3.1}$$

Where; m is the mass loss in grams; I is the corrosion current in amperes; t is the corrosion time in seconds; a is the atomic weight of the iron: 56 g; Z is the valence of the corroding iron: 2, and F is Faraday's constant: 96,500 ampere-seconds.

For this study, the specified corrosion levels were achieved within a relatively short time, with the use of an accelerated corrosion technique. The corrosion was initiated with the steel rebar embedded in chloride contaminated concrete (2.15 % by weight of cement), which were premixed within a specified zone in the concrete beam in order to depassivate the steel rebar, so that the corrosion could be achieved. Power supplies induced a constant current density of 200 μA/cm^2 through the bottom steel reinforcements (Figure 3.11). The technique is described in detail by El Maddawy and Soudki (2003). The test specimens were connected in series, and the corrosion circuit was completed, with the tension steel acting as the anode and the stainless steel bar acting as the cathode. Figure 3.12 shows a schematic of the corrosion circuit.
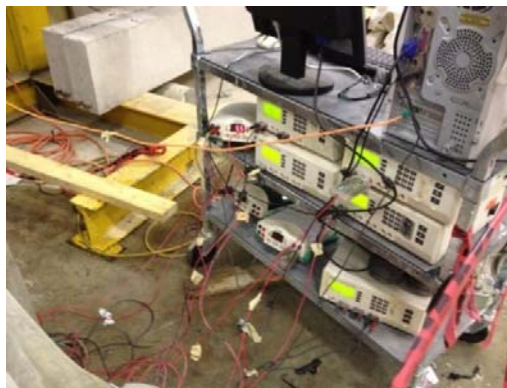

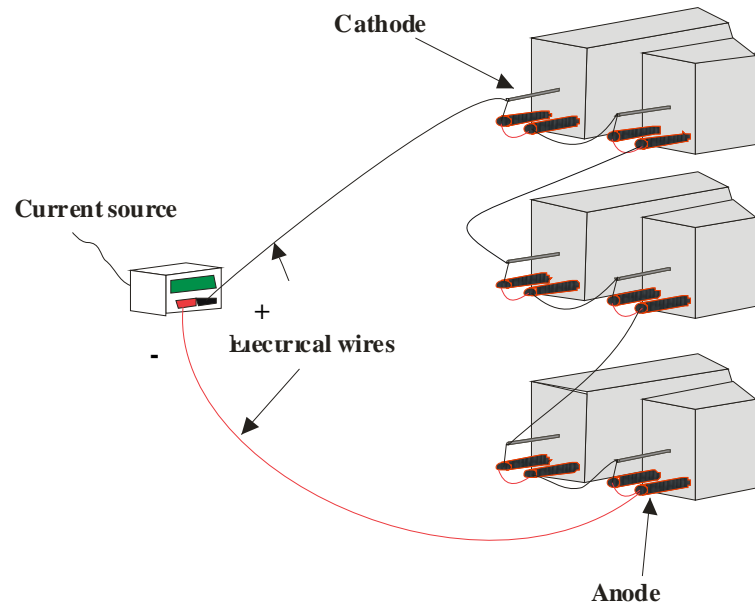**Figure 3.11: Power supplies used in accelerated corrosion process**

Figure 3.12: Schematic of the corrosion circuit

3.9 Corrosion Chamber

A large-scale corrosion chamber with two steel racks, with a capacity of 20 beams each, was used as a wetting room in order to simulate the desired humidity required to produce the corrosion. The steel racks frame supported the specimens, and a sprinkler system ensured a moist environment (90 % - 100 % RH) inside the chamber. The test specimens were placed upside down in the steel rack so that the bottom face (corroded side) would be fully subjected to the humid environment. Plastic sheets were used to cover the steel racks in order to isolate the chamber from the external laboratory atmosphere. Figure 3.13 illustrates the details of the corrosion chamber.
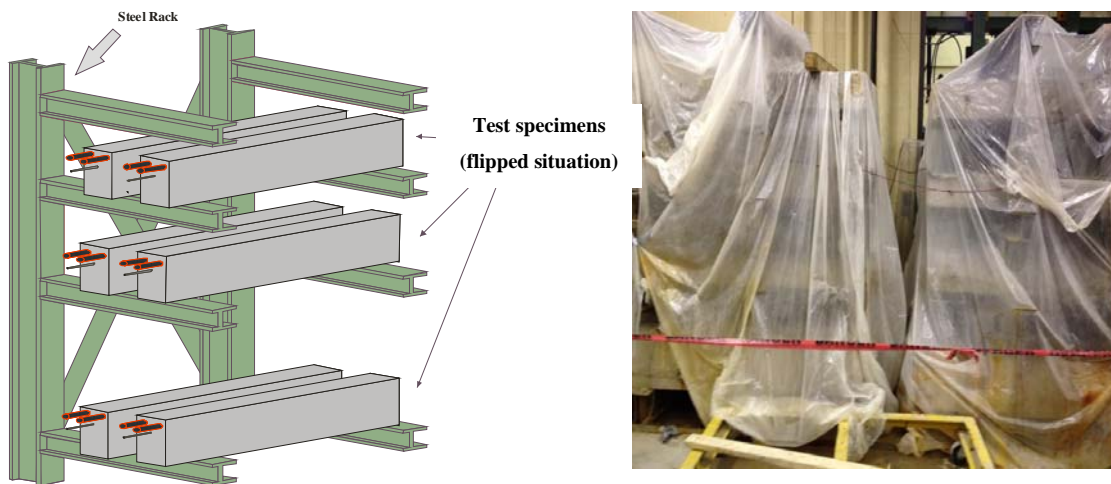
(a) Steel racks supporting the test specimens
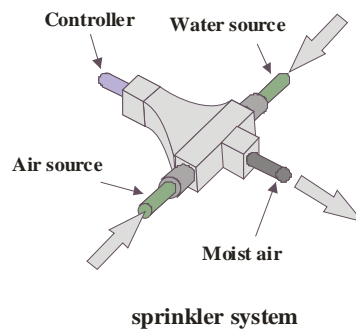
sprinkler system

(b) Sprinkler system providing moisture mist

(c)

Figure 3.13: Corrosion chamber components

3.10 Evaluation of corrosion

The corrosion of the steel rebar was evaluated based on the mass loss analysis described in ASTM standard G1-03, C.3.5. Mass loss analysis was conducted following the testing of the specimens. Coupons of steel reinforcement were extracted from each specimen, cleaned to remove any concrete on their surfaces, weighed, measured with respect to length, and then soaked for at least 10 min in a solution of hydrochloric acid so that the corrosion products would be extracted. The next step was to remove the steel coupons from the solution, and clean, dry, and weigh them. The mass loss was calculated as follows:

$$m\% = \frac{\text{mass of original steel - mass of corroded steel}}{\text{mass of original steel}} \qquad (3.2)$$

This process was repeated until no significant difference in the reduction in mass loss was observed between two successive trials. Figure 3.14 shows the mass loss analysis process.

(a) Preparing the solution

(b) Soaking the steel sections in the solution

(c) Cleaning and weighing the sections

Figure 3.14: Mass loss analysis process

3.11 Instrumentation

Three linear variable differential transformer (LVDTs) were used to monitor the displacement during testing. One vertical LVDT, with a range of 50 mm and an accuracy of 0.01 mm, was used to measure the vertical mid-span deflection. Two horizontal LVDTs, with a range of 25 mm and an accuracy of 0.01 mm, were used to measure the free-end slip in the two main reinforcing rebars. Figure 3.15 shows the horizontal and vertical LVDTs.

Strains in the steel rebar and concrete were monitored using electrical resistance strain gauges, manufactured by Kyowa Japan Inc., with a resistance of 120 Ω, and two different lengths: 5 mm and 60 mm respectively. The concrete strain was measured with the 60 mm strain gauges that were bonded on the concrete surface at the mid-span of each beam, in three different locations along the height of the beam (Figure 3.16). To monitor the stress level in the reinforcement rebars, 5 mm strain gauges were bonded to the steel rebars, close to the middle section of the beam.

(a) Horizontal LVDTs
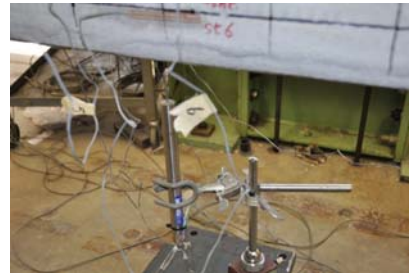
(b) Vertical LVDT
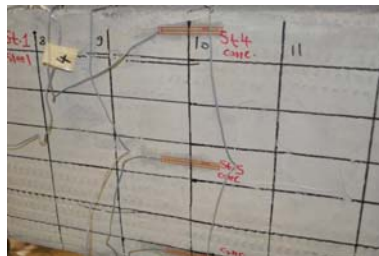
Figure 3.15: The vertical and horizontal LVDTs

Figure 3.16: Strain gauges

3.12 Test Setup and Test Procedure

All of the test specimens were tested monotonically to failure under two different loading configurations: three-point bending and four point-bending (Figure 3.17). Five specimens were loaded under three-point bending with a shear-span-to-depth ratio of 3.4. The remaining ten beams were loaded under four-point bending, which produces a constant moment region, with a shear-span-to-depth ratio of 2.4. The load was applied using a servo-controlled hydraulic actuator with a capacity of 500 kN, as shown in Figure 3.18. The loading was applied under displacement control at a rate of 3 mm per minute until beam failure occurred.
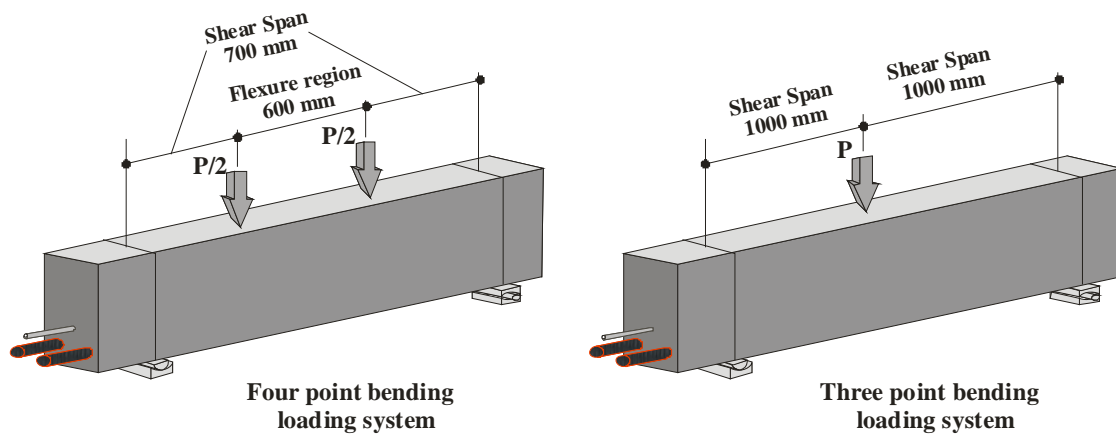
Figure 3.17: Loading configurations
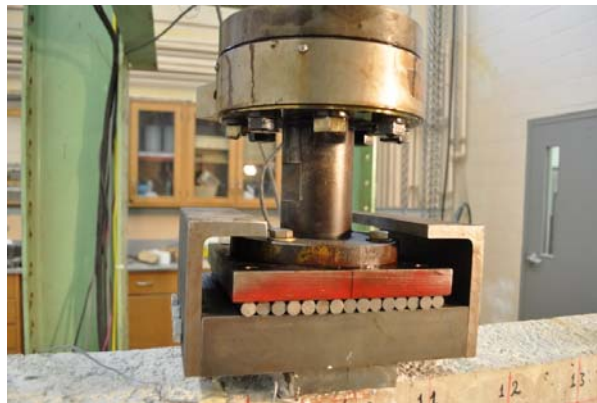
Figure 3.18: The 500 kN actuator

An MTS-406 controller was used to control the loading (Figure 3.19). Each test specimen was placed on a cylindrical mount at one end (roller support), and on a half-moon mount at

55

the other end (pin support). To avoid local crushing at the support points, bearing plates were placed between the mounts and the specimen. For the specimens tested with the four-bending configuration system, another set of half-moon and cylindrical mounts were placed at the loading points underneath the spreader beam.


Figure 3.19: The SCXI data acquisition system

For the specimens tested in the three-point bending configuration, the load was applied to the specimen through a steel plate. For the specimens tested in the four-point bending configuration, the load was applied to the specimen through a spreader steel beam. The loading rate used was 0.03 mm/min. Figure 3.20 shows the loading test setup.

A load cell attached to the 500 kN actuator was used in order to record the load. The mid-span deflection, horizontal end slip and material strains were recorded using an SCXI data acquisition system (Figure 3.19). Based on a specified accuracy level, a computer program provided control of the load data and the deflection data through a graphical interface.
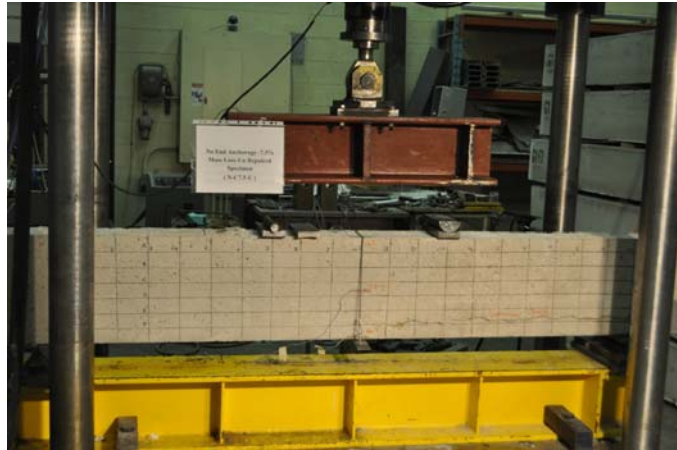
(a) Loading setup of the test specimen
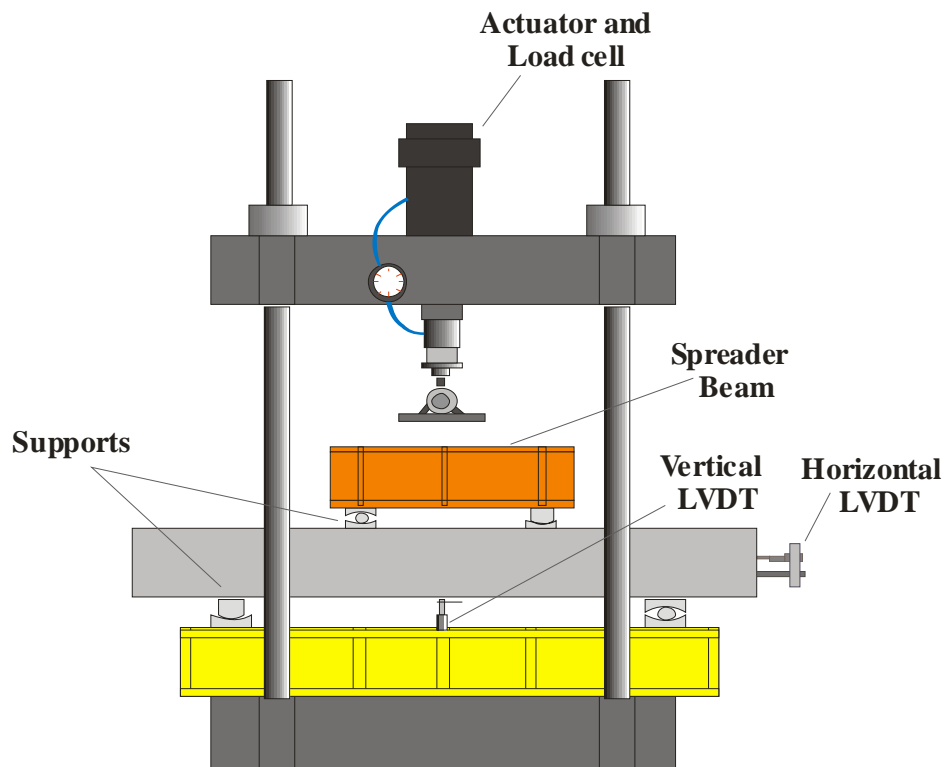
(b) Schematic of the loading setup

Figure 3.20: Loading test setup

Chapter 4

Experimental Results and Analysis

4.1 Introduction

In the current study, 15 reinforced concrete beams were constructed, corroded, repaired, and tested. The study variables included: corrosion level, load configuration, end anchorage condition, and repair scenario. This chapter presents the results of the experimental program followed by a detailed analysis and discussion of these results.

4.2 Corrosion Results

As described in Chapter 3, the specimens were subjected to four different corrosion levels: 2.5%, 5%, 7.5%, and 15% corrosion mass loss. During the corrosion exposure, the corroded specimens were inspected so that the widths of the corrosion cracks could be measured using a crack comparator of 0.15 mm accuracy. At the end of the corrosion phase, a detailed crack pattern was drawn for four selected specimens: A-C2.5-U-3B, A-C5-U-3B, A-C7.5-U-3B, and N-C15-U-4B. Following load testing, coupons of the steel reinforcing rebars were extracted from the corroded rebars of each specimen. The steel coupons were cleaned and weighed to access the steel mass loss due to corrosion according to ASTM G1-90. The results of the steel mass loss, the corrosion crack patterns, and propagation of the corrosion crack widths over time are presented and discussed in the following sections.

4.2.1 Mass loss results

After corrosion and load testing, eight 200 mm long coupons, four from each rebar were extracted from the two bottom corroded rebars in each specimen. The steel coupons were cleaned according to ASTM standard G1-90. The steel mass loss for the steel rebars was calculated as the average of the eight results of the steel coupons. As detailed in Table 4.1, the following mass loss results were obtained:

- For the specimen corroded for 30 days with 2.5% theoretical mass loss, the measured mass loss per coupon (eight coupons) ranged from 0.85% to 2.24%.

- For specimen corroded for 60 days (5% theoretical mass loss), the measured mass loss per coupon (eight coupons) ranged from 1.64% to 4.63%.

- For specimens corroded for 90 days (six specimens, 7.5% theoretical mass loss), the measured mass loss per coupon (48 coupons: eight per specimen) ranged from 5.37% to 8.91%. The average mass loss per specimen ranged from 6.71% to 8.27%.

- For specimens corroded for 180 days (six specimens, 15% theoretical mass loss), the measured mass loss per coupon (48 coupons: eight per specimen) ranged from 7.25% to 16.28%. The average mass loss per specimen ranged from 8.20% to 12.41%.

Table 4.1: Detailed corrosion results for the test specimens

Specimen notation	Exposure time (days)	Theoretical mass loss (%) (Faraday's law)	Actual corrosion mass loss (%)		Corrosion crack width range (mm)
			Steel section range	Average mass loss	
A-C2.5-U-3B	30	2.5	0.85-2.24	1.52	0.1-0.5
A-C5-U-3B	60	5	1.64-4.63	3.54	0.55-1.0
A-C7.5-U-3B		7.5	6.02-7.91	7.36	0.7-1.21
N-C7.5-U-3B		7.5	5.84-8.32	7.31	-
A-C7.5-U-4B	90	7.5	6.95-8.91	8.27	-
N-C7.5-U-4B		7.5	5.37-7.48	6.71	-
N-C7.5-R(GFRCM)-4B		7.5	5.94-8.16	7.13	-
N-C7.5-R(P)-4B		7.5	7.14-8.44	7.34	-
N-C15-U-4B		15	6.81-10.04	8.20	1.55-2.25
N-C15-R(GFRCM)-4B		15	11.53-16.28	12.41	-
N-C15-R(CFRCM)-4B	180	15	10.47-13.75	11.14	-
N-C15-R(P)-4b		15	9.98-14.22	11.93	-
N-C15-R(P+GFRCM)-4B		15	8.74-13.14	10.11	-
N-C15-R(P+CFRCM)-4B		15	8.65-13.44	10.74	-

It should be noted that, although a uniform current was induced along the length of the rebars in the corroded zone, a visual inspection of the corroded rebars revealed local corrosion pits on the steel surface. Figure 4.1 shows the corroded rebars at different corrosion levels. Figure

4.2 represents the average actual mass loss versus the exposure time. The best-fit relationship can be expressed as follows:

$$m_S = -0.0004t_C^2 + 0.1407t_c - 2.7243$$ (4.1)

where m_s is the average percentage of the mass loss of the reinforcing rebar and t_c is the corrosion exposure time in days

It was observed that Faraday's law overestimated the steel mass loss for all corrosion phases. For high corrosion levels, the overestimation agrees with the results provided by Badawi and Soudki (2005) who attributed the overestimation to the corrosion barrier that formed by the corrosion products around the reinforcing rebars, which prevents water and oxygen from reaching the steel surface and thus slows the corrosion process. The overestimation in the lower corrosion levels can be attributed to the small surface area of the stainless-steel tube (8mm diameter) compared to the surface area of the steel rebar (25mm diameter), or in other words the small cathode to anode surface area.

4.2.2 Corrosion crack widths and patterns

In this study, the first visible corrosion crack was visually observed after approximately 3 days. At the end of the corrosion exposure, corrosion crack maps were drawn for all corroded beams. These maps show the location and width in mm for all visible surface corrosion cracks. The widths of the cracks were measured along the length of the corroded zone with the use of a crack comparator and an electronic dial caliper. The results of these measurements were used to assess the upper and lower bounds of the corrosion crack widths as a function of the severity of the corrosion, as explained later in section 4.2.3. As shown in Figure 4.3, all test specimens exhibited two main longitudinal cracks on the sides of the beam parallel to the two bottom-longitudinal steel rebars along the length of the corroded zone. At the end of the fourth corrosion phase, hairline cracks appeared along the bottom of the beam cross-section in the corroded zone, and vertical hairline cracks occurred at some stirrup locations.

(a) Exposure time 0 days (0 % mass loss)

(b) Exposure time 30 days (2.5 % mass loss)

(c) Exposure time 60 days (5 % mass loss)

(d) Exposure time 90 days (7.5 % mass loss)

(e) Exposure time 180 days (15 % mass loss)

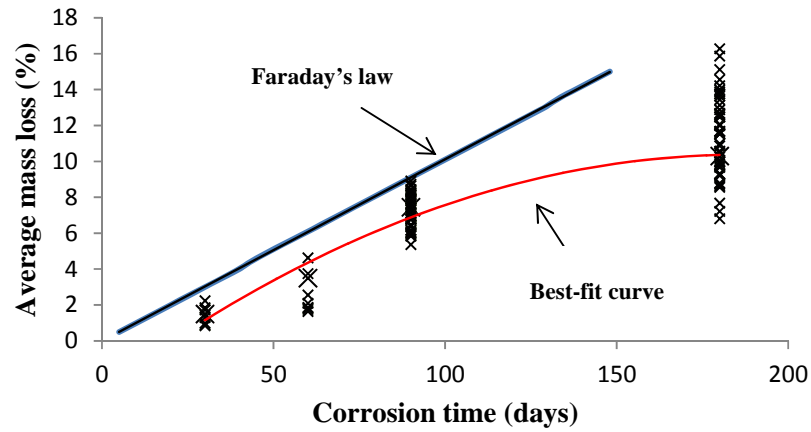**Figure 4.1: Corrosion of the steel rebars at different exposure times**

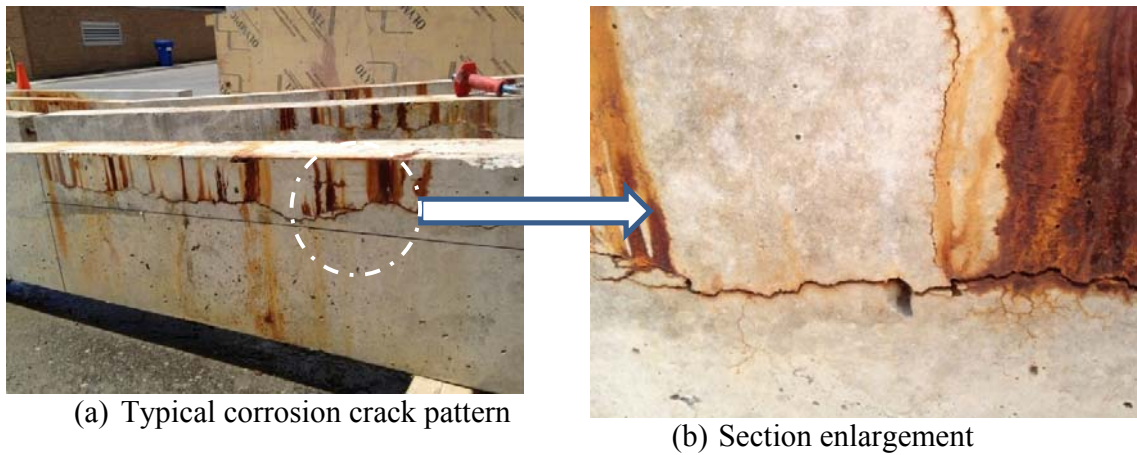**Figure 4.2: Variation in the experimental steel mass loss with corrosion time**

(a) Typical corrosion crack pattern

(b) Section enlargement

Figure 4.3: Typical longitudinal corrosion side-cracks

The corrosion crack patterns for specimens A-C2.5-U-3B (2.5% mass loss, 30 days), A-C5-U-3B (5% mass loss, 60 days), A-C7.5-U-3B (7.5% mass loss, 90 days), and N-C15-U-4B (15% mass loss, 180 days) are shown in Figures 4.4, 4.5, 4.6 and 4.7 respectively. For each figure, the corrosion cracks are identified by a solid line, and the left and right beam faces are illustrated. The maximum corrosion crack widths measured in these typical specimens were 0.5 mm, 1.0 mm, 1.21 mm, and 2.25 mm at the end of the first, second, third, and fourth corrosion phases, respectively.
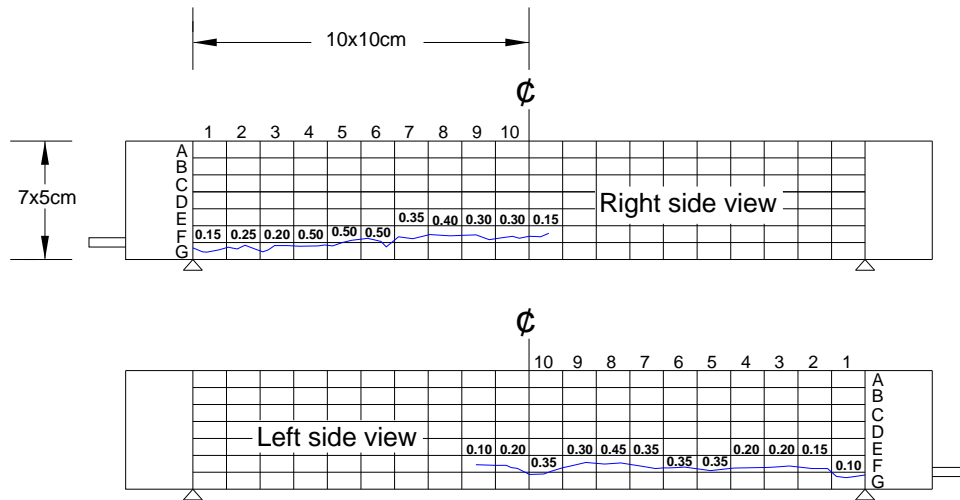
Figure 4.4: Corrosion crack pattern for specimen A-C2.5-U-3B at the end of the first corrosion phase (30 days)
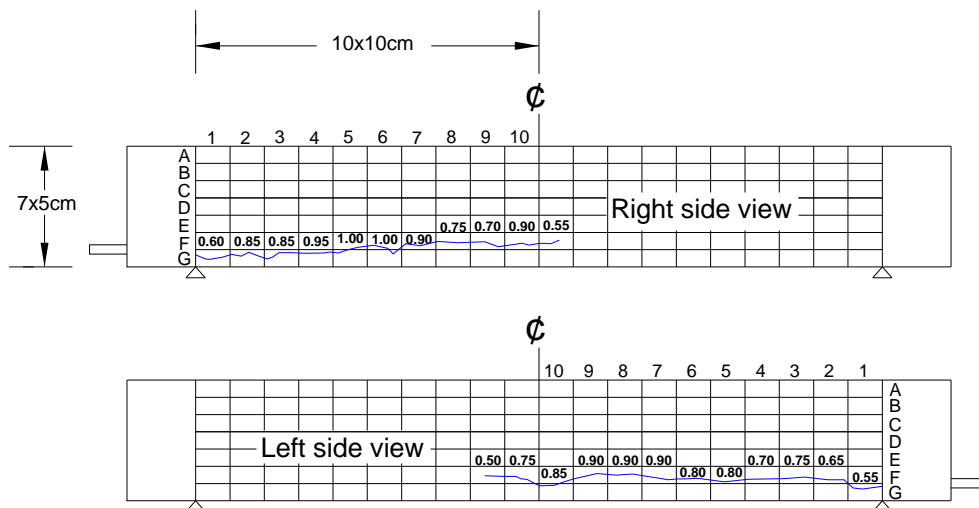
Figure 4.5: Corrosion crack pattern for specimen A-C5-U-3B at the end of the second corrosion phase (60 days)
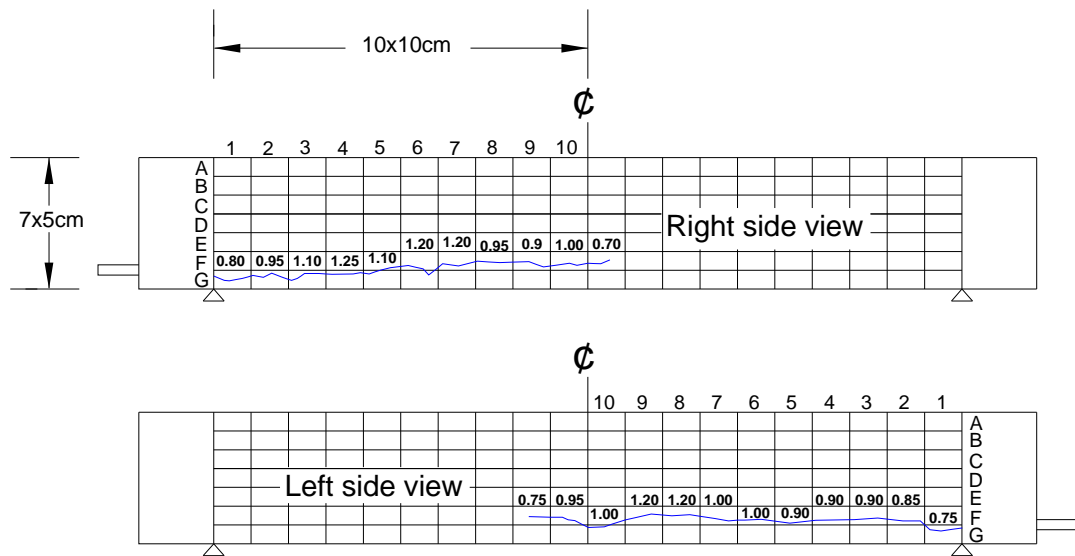
Figure 4.6: Corrosion crack pattern for specimen A-C7.5-U-3B at the end of the third corrosion phase (90 days)
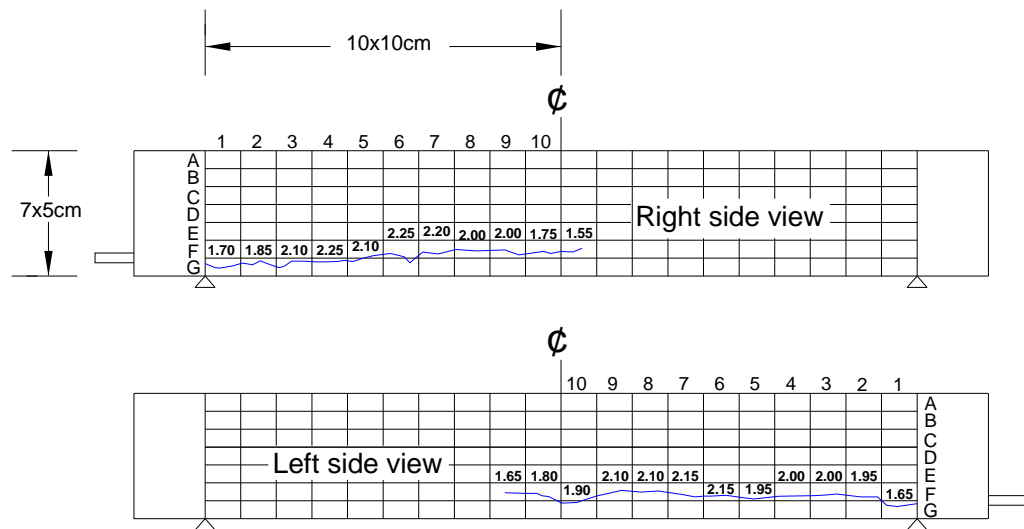
Figure 4.7: Corrosion crack pattern for specimen N-C15-U-4B at the end of the fourth corrosion phase (180 days)

4.2.3 Corrosion crack widths as a function of the degree of corrosion

Specimen N-C15-U-4B (15 % mass loss: 180 days) was selected as a typical specimen for the recording of the corrosion crack widths at short time-intervals in order to evaluate the progression of the corrosion crack width versus the exposure time. Figure 4.8 shows the relationship between the measured crack widths and time for specimen N-C15-U-4B. The crack width measurements observed for beam N-C15-U-4B were somewhat scattered which is due to the non-uniformity of the corrosion. In general, the crack width increased linearly with corrosion time. To define the relationship between the crack width and the average steel mass loss, Equation (4.1) was used to calculate the average mass loss corresponding to the different exposure times shown in Figure 4.8. Then the variation of crack width vs. mass loss was plotted in Figure 3.9. The cracking behaviour varied in the four corrosion phases: phase 1 during which crack width increased rapidly with corrosion, phases 2 and 3 where crack width increased slowly with corrosion mass loss, and during phase 4 corrosion crack width increased rapidly with little increase in mass loss.
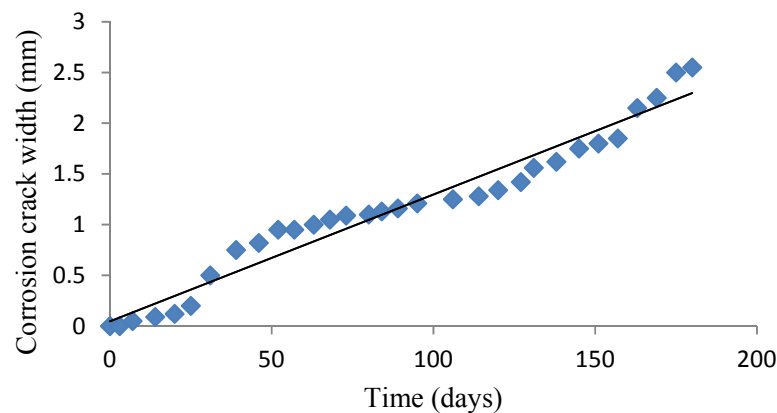
Figure 4.8: Corrosion crack widths versus exposure time for specimen N-C15-U-4B
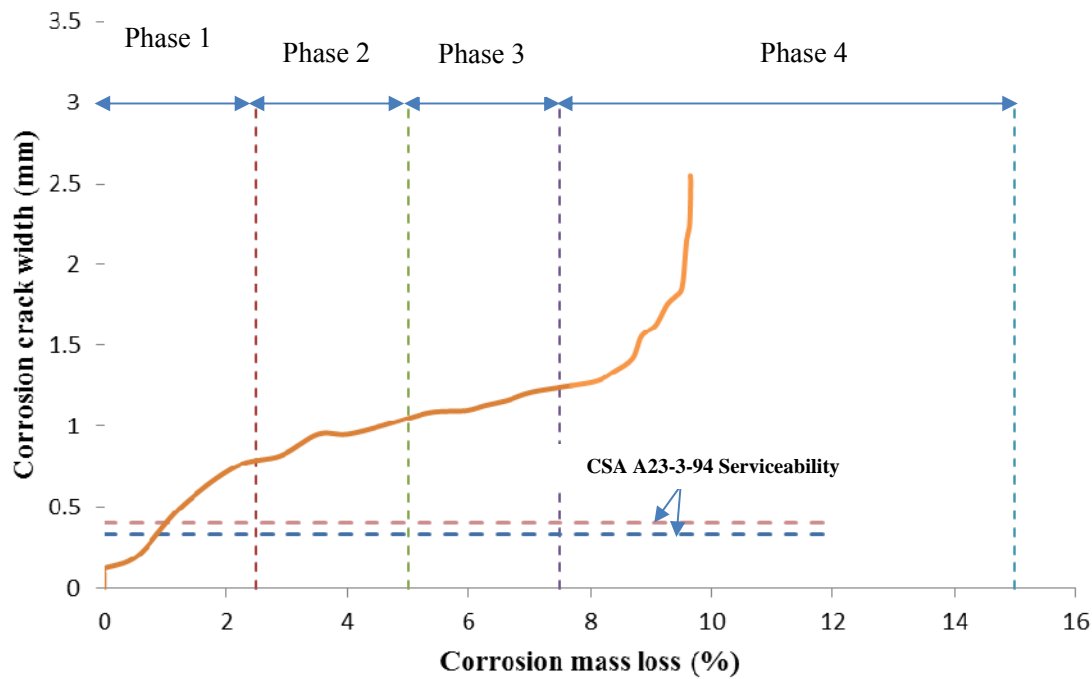
Figure 4.9: Corrosion crack widths versus corrosion mass loss for specimen N-C15-U-4B

Due to the absence of specifications regarding the limits of the corrosion crack widths, the flexural crack limits provided in CSA A23.3-94 were used to assess the serviceability condition of the test specimen (Figure 4.9). Clause 10.6 states that the maximum allowable flexural transverse crack width for beams and one-way slabs in service is limited to 0.33mm and 0.4mm for interior and exterior exposure conditions, respectively. According to Figure 4.9, these limits would correspond to corrosion mass losses of 1% and 1.5% for the two exposure conditions. This indicates that all specimens in this study failed to meet the serviceability limit state.

4.3 Loading Test Results

All test specimens were loaded monotonically in flexure to the failure. During testing, the following measurements were monitored: the load, the mid-span vertical deflection, the mid-span strain in the main reinforcing steel rebars, the mid-span concrete top strain, and the end slips of the tension reinforcing steel rebars.

The following definitions are important for the understanding of the load-testing results:

- Cracking load: the load value at which the first flexural crack appears at any location along the beam span, or the load value that corresponds to the appearance of the first non-linear trend in the load-deflection curve

- Yielding load: the load value at which the tensile steel reinforcement yields

- Ultimate load: the maximum load value that can be sustained by the beam before failure

- Failure load: the load value at which a significant drop in the load occurs, and corresponds to one or more of the following modes of failure: concrete crushing, fiber rupture, and bond splitting

- Bond capacity: the load value that corresponds to the end slip at which a significant drop in the load occurs

- Ultimate deflection: the deflection value that corresponds to the failure load

- Ultimate slip: the end slip value that corresponds to the failure load

- Anchorage capacity:, the maximum value of the tensile force in the steel rebar that crossing an inclined shear crack near a support, assuming bond stress is constant alone the anchorage length

- Flexural failure mode: characterized by the yielding of the tension steel reinforcement followed by concrete crushing with no visible splitting cracks

- Bond pull out failure mode: rebar pulling out of moderate confined concrete sections where the force transfer mechanism changes from rib bearing to friction after the shear resistance of the concrete between adjacent ribs is exceeded.

- Bond splitting failure mode: occurs when the splitting cracks extend to the free surface and thus reduce the development of the concrete confinement to the reinforcing rebar.

Based on the material properties and dimensions of the specimen, the predicted cracking moment is 18.51 kN.m which corresponds to a cracking load of 37.02 kN (15% of the ultimate capacity) for the three-point bending configuration and 52.89 kN (16% of the ultimate capacity) for the four-point bending configuration. With the use of section analysis and based on the material properties and dimensions of the specimen, the predicted ultimate moment was 110 kN.m which corresponds to a load of 220 kN for the three-point bending configuration and 314.29 kN for four-point bending configuration.

Table 4.2 summarizes the load test results including the cracking load, yield load, and ultimate load, along with the corresponding mid span deflection and end slip values. The results of the load testing are described in the following sections.

Table 4.2: Summary of the load-carrying capacity of the test specimens

Specimen	Mass loss (%)	Cracking stage		Yielding stage		Ultimate stage			Failure mode
		Load (KN)	Deflection (mm)	Load (KN)	Deflection (mm)	Load (KN)	Deflection (mm)	End slip (mm)	
A-C0-U-3B	0	58	1.88	209	7.5	250	23	≈ 0	Flexure
A-C2.5-U-3B	1.52	58	2.03	224	11	239	17	≈ 0	Flexure
A-C5-U-3B	3.54	58	1.62	214	7	255	21	≈ 0	Flexure
A-C7.5-U-3B	7.36	58	1.07	212	7	244	22	≈ 0	Flexure
N-C7.5-U-3B	7.31	54	1.17	222	8.5	260	23	≈ 0	Flexure
A-C7.5-U-4B	8.27	61	1.15	300	7	322	13	≈ 0	Flexure
N-C7.5-U-4B	6.71	64	1.58	305	9	323	17	0.33	Flexure
N-C7.5-R(GFRCM)-4B	7.13	68	2.02	290	11	317	>50	0.2	Flexure
N-C7.5-R(P)-4B	7.34	31	0.94	-	-	276	8	1.5	Bond
N-C15-U-4B	8.2	54	1.66	295	10	313	15	0.65	Bond
N-C15-R(GFRCM)-4B	12.41	57	1.09	-	-	270	7.5	0.16	Bond
N-C15-R(CFRCM)-4B	11.41	83	1.67	297	8.5	325	11	0.5	Bond
N-C15-R(P)-4B	11.93	73	1.71	-	-	288	9	0.25	Bond
N-C15-R(P+GFRCM)-4B	10.11	58	1.95	260	8.3	290	11.6	0.31	Bond
N-C15-R(P+CFRCM)-4B	10.74	69	1.74	317	9.6	340	12.2	0.56	Bond

4.3.1 Load-cracking behaviour

This section describes the flexural cracks that developed during load testing. The loading crack maps for the beams are provided in Appendix A. As an example, Figure 4.10 illustrates the load induced crack map of beam A-C7.5-U-4B. The crack maps are used to quantify the crack development with load by recording the average flexural crack numbers and average spacing. Table 4.3 summarizes the number of flexural cracks and the average crack spacing as observed in all test specimens. It is evident that in the case of anchored specimens, as corrosion level increased the number of cracks decreased and the crack spacing increased. More cracks were observed and crack spacing was reduced with the non-anchored specimens. The specimens corroded to 15 % theoretical mass loss then repaired

with GFRCM or CFRCM and patch exhibited more cracking and closer crack spacing un-
der load.
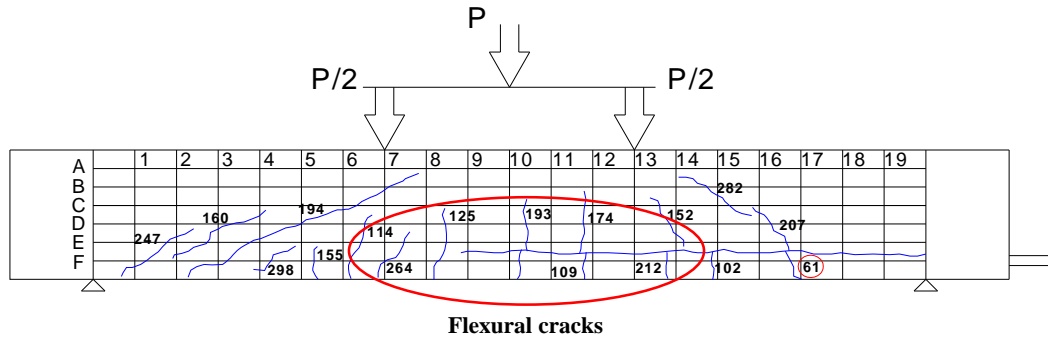
Figure 4.10: Load-cracking behaviour for specimen A-C7.5-U-4B

Table 4.3: Flexural crack details

Specimen	No. of cracks	Shear span average spacing (mm)	Mass loss
A-C0-U-3B	11	159	0
A-C2.5-U-3B	5	300	1.52
A-C5-U-3B	7	174	3.54
A-C7.5-U-3B	5	363	7.36
N-C7.5-U-3B	9	197	7.31
A-C7.5-U-4B	9	149	8.27
N-C7.5-U-4B	7	99	6.71
N-C7.5-R(GFRCM)-4B	9	114	7.13
N-C7.5-R(P)-4B	8	118	7.34
N-C15-U-4B	7	172	8.2
N-C15-R(GFRCM)-4B	8	86	12.41
N-C15-R(CFRCM)-4B	17	85	11.41
N-C15-R(P)-4B	11	123	11.93
N-C15-R(P+GFRCM)-4B	12	113	10.11
N-C15-R(P+CFRCM)-4B	17	97	10.74

4.3.2 Failure modes

Two failure modes were observed: flexural failure (ductile) and bond failure (brittle). Eight beams failed in flexure and seven beams failed in bond (Table 4.4).

For the beams that exhibited flexure failure, the first crack was visually observed at a load range of 21%-23% of the ultimate capacity for the three-point bending configuration and at a load range of 19%-21% of the ultimate capacity for the four-point bending configuration. As the load was increased, more flexural and shear-flexural cracks continued to appear along the beam span until yielding of the tension steel occurred at about 84%-95% of the ultimate capacity. The flexural cracks increased in width and number, and propagated toward the loading point. At this point, the beam was no longer able to resist the applied load, and failed by concrete crushing. Figure 4.11 provides photos of the flexural failure mode. It is important to note that in specimen N-C7.5-R(GFRCM)-4B, the composite repair system provides enough confinement for the concrete to prevent the load drop after failure, thus offering a more ductile post-failure behaviour.

In beams that exhibited bond failure, the first crack was visually observed at a load range of 12%-29% of the ultimate capacity. As the load was increased, more flexural and shear-flexural cracks continued to appear along the beam span until the yielding of the tension steel occurred at about 89% %-94% of the ultimate capacity. After that point, longitudinal cracks started to appear in the un-bonded zone of the beam end at about 95%-98% of the ultimate capacity, and the rebar began to slip. Shortly thereafter, the longitudinal cracks increased in width and number. At this point, the beam was no longer able to resist the load and it failed. It is important to note that specimens N-C7.5-R(P)-4B, N-C15-R(GFRCM)-4B, and N-C15-U-4B exhibited pure brittle behaviour with no yield points. The side and bottom splitting cracks in the unrepaired and patch-repaired beams indicate that the final failure mode was bond splitting. In contrast, the side and bottom splitting cracks in the wrapped and/or patched-wrapped beams indicate that the final failure mode was splitting-induced pull-out failure. Figure 4.12 shows photos of the bond failure. Appendix B provided photos of failure modes for all test specimens.
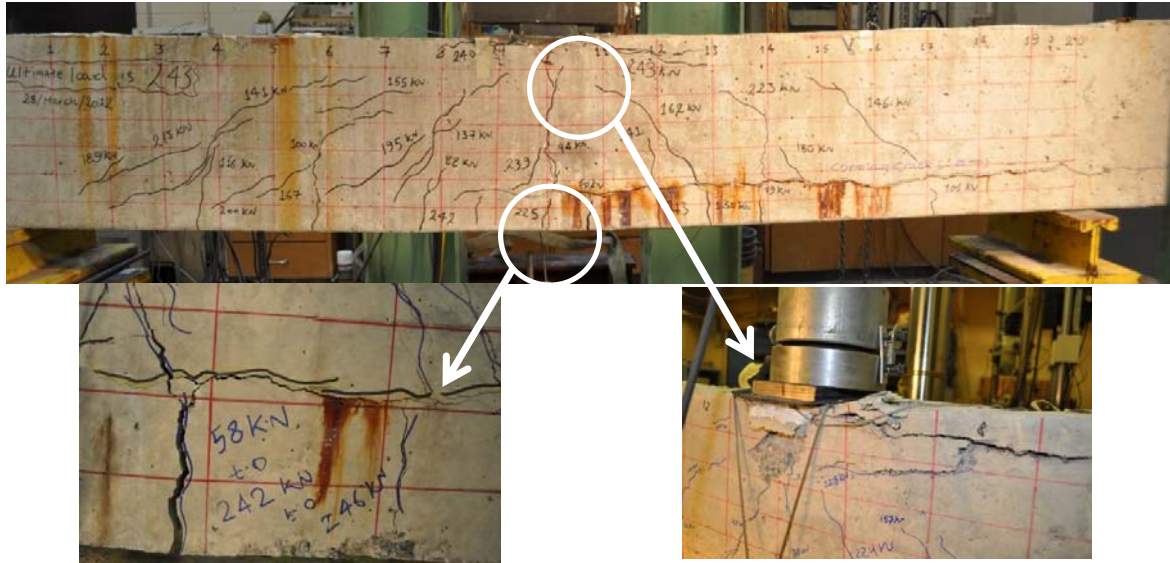
Figure 4.11: Flexural failure mode

(a) Splitting bond failure
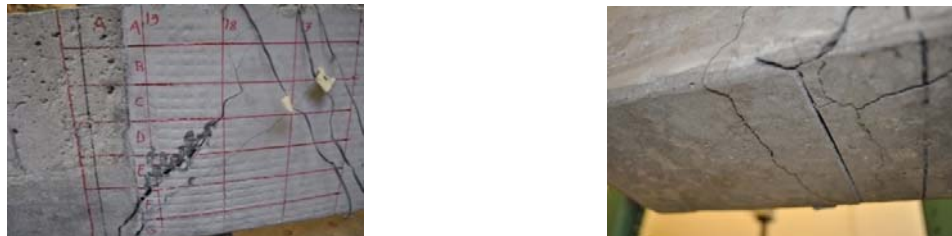
(b) Splitting-induced pull-out failure

Figure 4.12: Bond failure mode

4.3.3 Load-deflection behaviour

Load-deflection curves provide a great deal of information about the structural behaviour of test specimens. In particular, they revealed the effect of corrosion, the influence of the end anchorage condition, and the effectiveness of the repair scheme.

Figures 4.13 and 4.14 show typical load-deflection curves observed in this study: one for beam A-C0-U-3B which failed in flexure, and the other for beam N-C7.5-R(P)-4B which failed in bond. Beam A-C0-U-3B (flexure) exhibited an approximately linear trend until the yielding of the tensile steel reinforcement, followed by a nonlinear trend to the point of concrete crushing (Figure 4.13). Beam N-C7.5-R(P)-4B (bond) displays an approximately linear trend until the peak load, which was followed by a nonlinear decreasing trend (Figure 4.14). For both curves, the slope of the load-deflection curve up to the yielding of the steel reinforcement (flexural failure) or up to peak load (bond failure) represents the stiffness of the beam, while the ductility is defined as the ratio of the ultimate deflection to the yielding deflection (ductility was not defined in the case of bond failure). The calculated stiffness and ductility values of all test specimens are summarized in Table 4.4.

Table 4.4 shows that low and medium corrosion levels lead to slightly increased the beam stiffness. This can be explained based on the fact that corrosion products enhanced the bond between the reinforcing steel and the concrete, and that the reduction in the area of reinforcing steel caused by the low to medium corrosion did not contribute to the stiffness reduction. However, at severe corrosion level the non-anchored beams had a pronounced decrease in stiffness because of the combination of both the bond deterioration due to corrosion, and the loss of bond in the anchorage zone. Appendix C provided load-deflection curves for all test specimens.
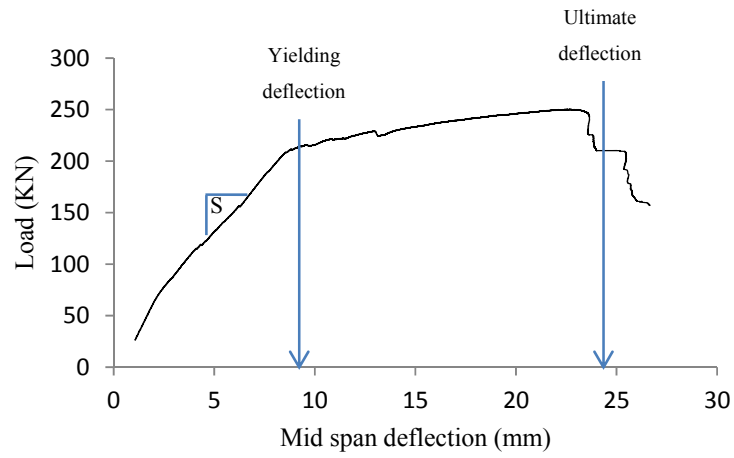
Figure 4.13: Load-deflection behaviour for specimen A-C0-U-3B
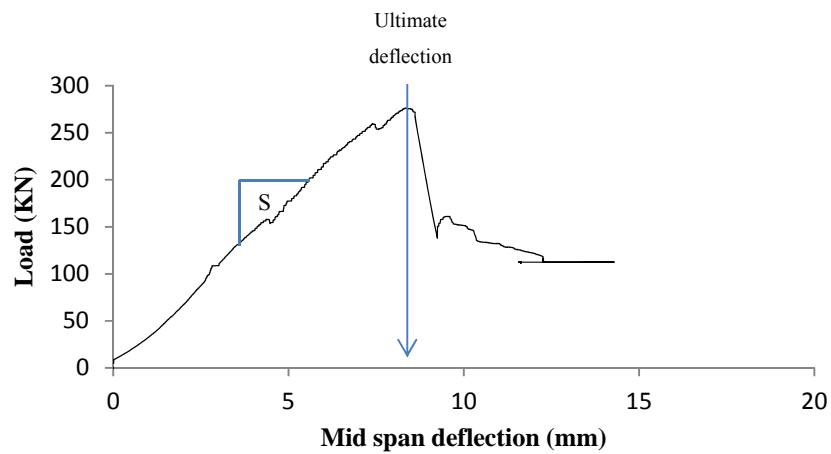
Figure 4.14: Load-deflection behaviour for specimen N-C7.5-R(P)-4B

74

Table 4.4: Summary of the stiffness and ductility of the test specimens

Specimen	Mass loss (%)	Stiffness (KN/mm)	Ductility	Failure mode
A-C0-U-3B	0	22.09	3.07	Flexure
A-C2.5-U-3B	1.52	23.12	1.54	Flexure
A-C5-U-3B	3.54	22.31	3.00	Flexure
A-C7.5-U-3B	7.36	25.38	3.14	Flexure
N-C7.5-U-3B	7.31	42.29	2.71	Flexure
A-C7.5-U-4B	8.27	26.18	1.86	Flexure
N-C7.5-U-4B	6.71	31.80	1.89	Flexure
N-C7.5-R(GFRCM)-4B	7.13	30.84	4.55	Flexure
N-C7.5-R(P)-4B	7.34	25.29	-	Bond
N-C15-U-4B	8.2	37.25	1.50	Bond
N-C15-R(GFRCM)-4B	12.41	34.52	-	Bond
N-C15-R(CFRCM)-4B	11.41	31.85	1.29	Bond
N-C15-R(P)-4B	11.93	30.36	-	Bond
N-C15-R(P+GFRCM)-4B	10.11	29.80	1.4	Bond
N-C15-R(P+CFRCM)-4B	10.74	32.86	1.53	Bond

4.3.4 Load-end slip behaviour

For beams that had bond failures, the load-end slip curves describe how the bond degradation changes the behaviour of the beam from a ductile flexural to a brittle bond of faliure. The factors that affect the bond-end slip behaviour for such specimens include the severe corrosion mass loss, the partial loss of the bond between the cleaned/corroded rebar and the concrete patch, the confinement of the FRCM wrapping system, and the artificial loss of the bond at the support zone.

In this study, the end-slip of the steel rebar was induced by the longitudinal cracks in the concrete that initiated at the steel rebar ribs concrete interface. The propagation of these cracks, together with the loss in steel lug height due to corrosion and/or sandblasting (cleaning), eventually weakened the resistance of the concrete keys. In both the repaired and unrepaired beams, when the bearing resistance of the concrete keys was exceeded, the steel bar started to slip at the free end. The artificial loss of bond at the end of the shear span is expected to increase the end slip by reducing the bond stiffness. The FRCM repair system is

expected to provide confinement for the concrete cross-section that would delay the initiation of the end slip by enhancing the bond stiffness. Figure 4.15 shows photos of the concrete below the steel rebars for corroded, un-corroded-unrepaired, and corroded-patched beams. The markings of the ribs on the concrete were evident in the case of the un corroded-unrepaired beam (Figure 4.15 (a)), they were less pronounced in the corroded-patched beam (Figure 4.15 (c)) and almost non-existent in the corroded-un repaired beam (Figure 4.15 (b))

(a) Concrete below steel in un-corroded specimen

(b) Concrete below steel in corroded specimen

(c) Concrete below steel in patched specimen

Figure 4.15: Concrete below the steel in the test specimens

To determine the bond-end slip behaviour of the test specimens, the bond mechanism and limitations provided in FIB 2000 were adopted and applied to the measured bond stress-slip curves. Figure 4.16 shows the bond stress-slip curves for the two types of bond failures observed in this study: bond splitting failure (beam N-C15-U-4B) and bond splitting-induced-pull-out failure (beam N-C15-R(P+CFRCM)-4B).

The Roman numerals in the figure indicate the stage in the slip behaviour. Stage (*I*) is characterized by no slip and the bond stress was resisted only by the chemical adhesion. Stage (*II*)

is characterized by the breakdown of the chemical adhesion, with a very small amount of slip; the bond stress was resisted by the bearing stress at the concrete lugs. Stage (*III*) is characterized by significant slip and the appearance of longitudinal splitting cracks; the bond stress was resisted by friction. In stage (*IVb*), the splitting cracks break out to the free concrete surface, and the bond stress was resisted by the confinement of the transverse reinforcement. Stage (*IVc*) denotes the pull-out bond failure, in which the splitting cracks were limited and the transverse reinforcement and the wrapping repair provided high confinement. Figure 4.17 shows the bond-stress-slip curves for the other test specimens that exhibited bond failure. Details of the bond strength mechanics that was adapted from FIB 2000 were explained in detail in Chapter 2. Load-end slip curves for all test specimens are provided in Appendix D.
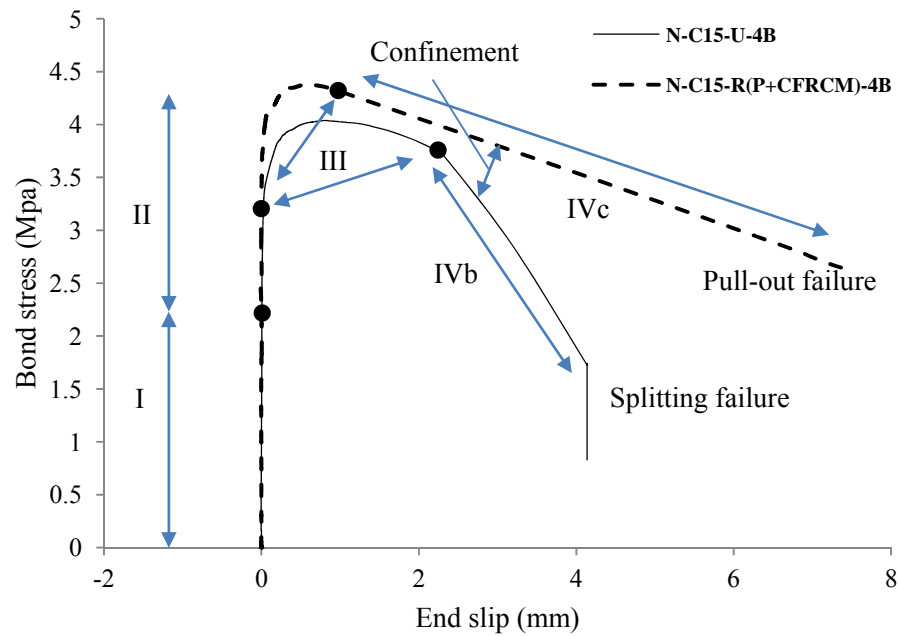
Figure 4.16: Bond stress-end slip relationship for specimens N-C15-U-4B and N-C15-R(P+CFRCM)-4B
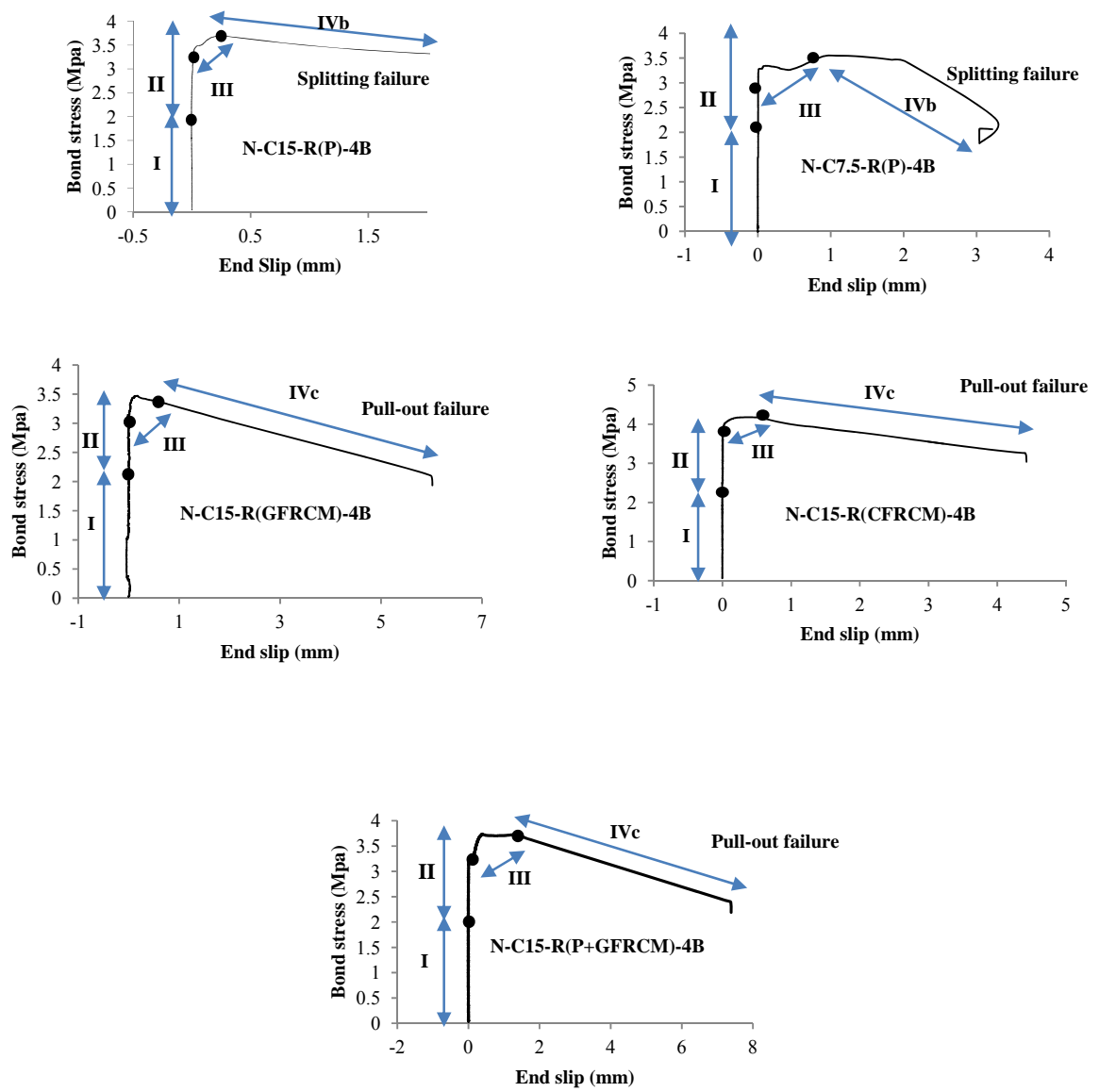
Figure 4.17: Bond stress-end slip relationships for additional test specimens

4.4 Discussion of Test Results

This section presents a discussion of the experimental results from both a qualitative and a quantitative perspective. The focus is on the effect of shear span corrosion and the different repair schemes on the structural performance of the test specimens.

4.4.1 Effects of shear span corrosion

4.4.1.1 Beams with properly anchored longitudinal reinforcement

All of the beams in this group had properly anchored longitudinal reinforcement. The beams were corroded to 2.5 %, 5 %, and 7.5 % theoretical mass loss; the actual mass losses achieved were 1.5 %, 3.5 %, and 7.36 %. They were unrepaired and loaded in three-point bending configuration. These beams exhibited flexure failure through concrete crushing after the steel yielded and there was no sign of shear or shear-bond failure modes (Figure 4.18). Figure 4.19 shows the load-deflection curves for the properly anchored shear-span corroded beams both versus the control (un-repaired) beam. Neither the cracking load nor the yield load of the corroded beams was affected by corrosion. The yield load increased with corrosion in the range of 1.44 %-7.18 %. The ultimate load was also not affected by shear span corrosion, with the reduction in the ultimate load in the range of -2.4 %-4.4 % with corrosion level up to 7.36 % mass loss. These results can be explained based on the fact that the reinforcement was full bonded in the anchorage zone, and because the beams failed by flexure at mid span, which was in the un-corroded zone. The shear-span corrosion slightly increased the flexural stiffness of the beams in the range of 5.7 %-7.1 %, the ductility of the corroded specimens were also unaffected by the shear span corrosion. Except for the beam with 1.52 % mass loss, in which the ductility was reduced by 48.3 %. The corroded beams exhibited fewer cracks in the corroded shear span, primarily because the loading cracks intercepted the longitudinal corrosion crack. The reduction in the average number of flexural cracks was in the range of 36. %-55 %. The increase in the average crack spacing was in the range of 9 %-128 % (Figure 4.20).
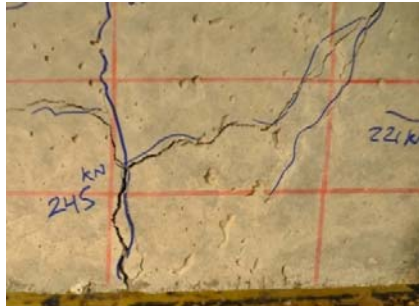
(a) **Beam A-C0-U-3B**
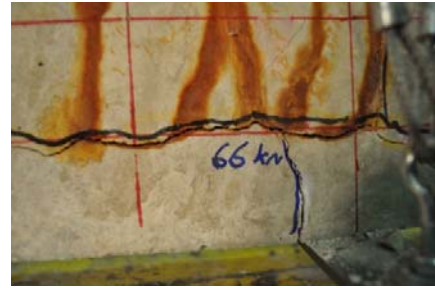
(b) Beam A-C2.5-U-3B

(c) Beam A-C5-U-3B

(d) Beam A-C7.5-U-3B

Figure 4.18: Failure modes of anchored beams
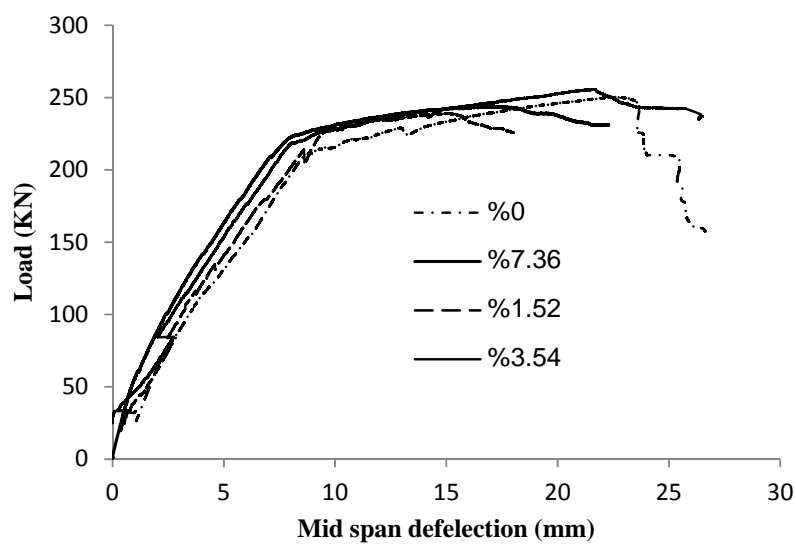
Figure 4.19: Effects of corrosion in anchored beams

Beam A-C0-U-3B

Beam A-C2.5-U-3B

Beam A-C5-U-3B

Beam A-C7.5-U-3B
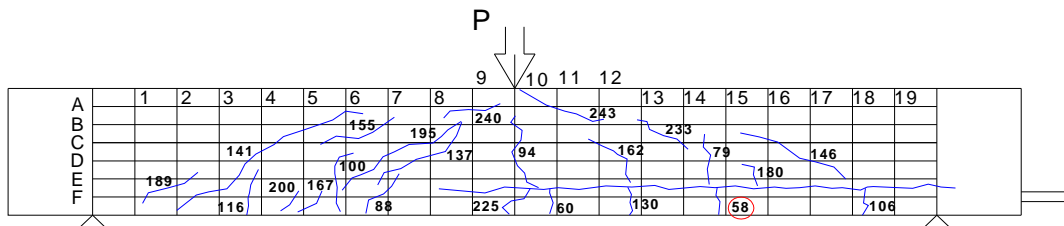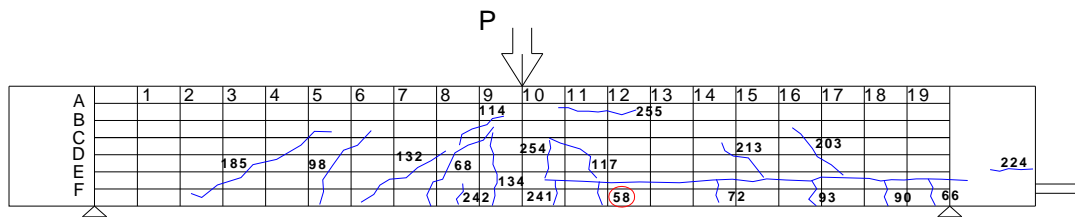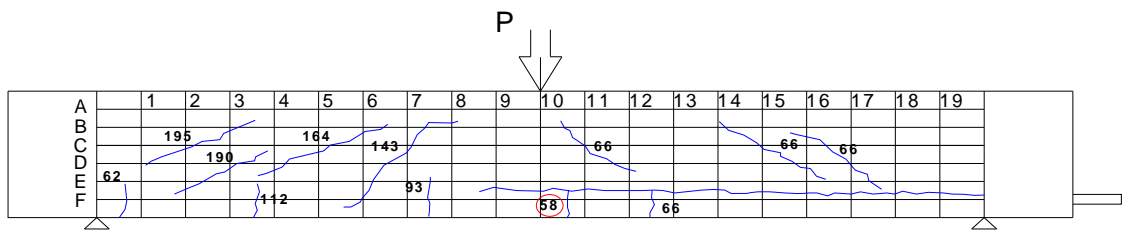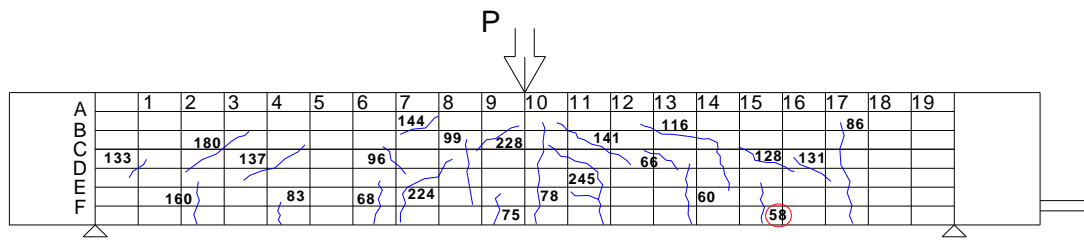
Figure 4.20: Load-cracking patterns for anchored beams

81

4.4.1.2 Beams with non-anchored longitudinal reinforcement

Figure 4.21(a) presents the load-deflection relationship for two unrepaired beams with improperly anchored reinforcement at different corrosion levels. Beam N-C7.5-U-4B and Beam N-C15-U-4B were corroded to theoretical mass losses of 7.5% and 15% but achieved average mass losses of 6.71% and 8.2%, respectively. When shear span corrosion increased by 22% (from 6.71% to 8.2%), the mode of failure changed from a ductile flexural mode to a brittle bond mode (Figure 4.22). The cracking load was reduced by 15.63%, but the yield load and the ultimate load were slightly reduced by 3.28%, and 3.1% respectively. Also, the stiffness of the beam was reduced by 17.14%. The ductility of the section was also reduced by 20.63% due to the increase in shear span corrosion. These results can be attributed to the loss of the cross-sectional area of the steel rebar. The two specimens exhibited the same number of flexural cracks but with a clear 74% increase in the average spacing between the cracks (Figure 4.23). The change in the beam behaviour due to high shear-span corrosion can be explained by looking at Figure 4.21(b) which represents the load-end slip relationship for these beams. The 22.21% increase in shear-span corrosion (from 6.71% to 8.2% mass loss) weakened the resistance of the concrete keys through the initiation and propagation of longitudinal concrete cracks at the steel rebar ribs. As the load increased, inclined shear-bond cracks began to propagate on the support zone. As a result, at about 90% of the maximum load, the steel rebar exhibited significant end slip at the free end. As the slip increased, splitting cracks were observed at the support zone. At this point, the beam was no longer able to take the load and bond failure occurred in specimen N-C15-U-4B.
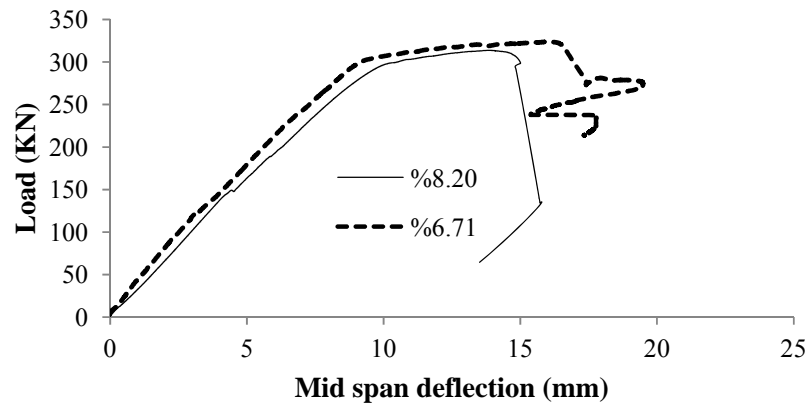
(a) Load-deflection relationship
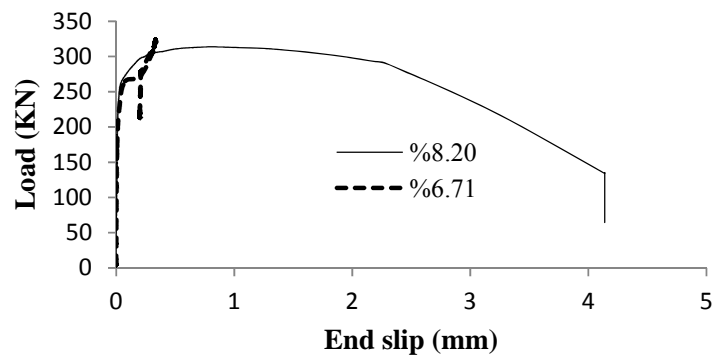
(b) Load-end slip relationship

Figure 4.21: Effects of corrosion in non-anchored beams
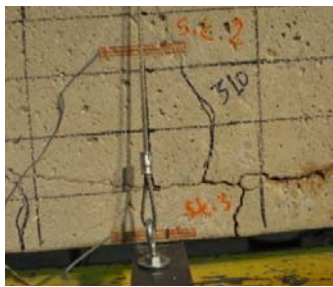
(a) N-C7.5-U-4B
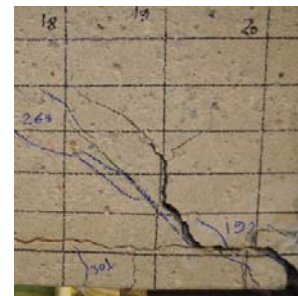
(b) N-C15-U-4B

Figure 4.22: Failure modes for non-anchored beams

(a) N-C7.5-U-4B

(b) N-C15-U-4B
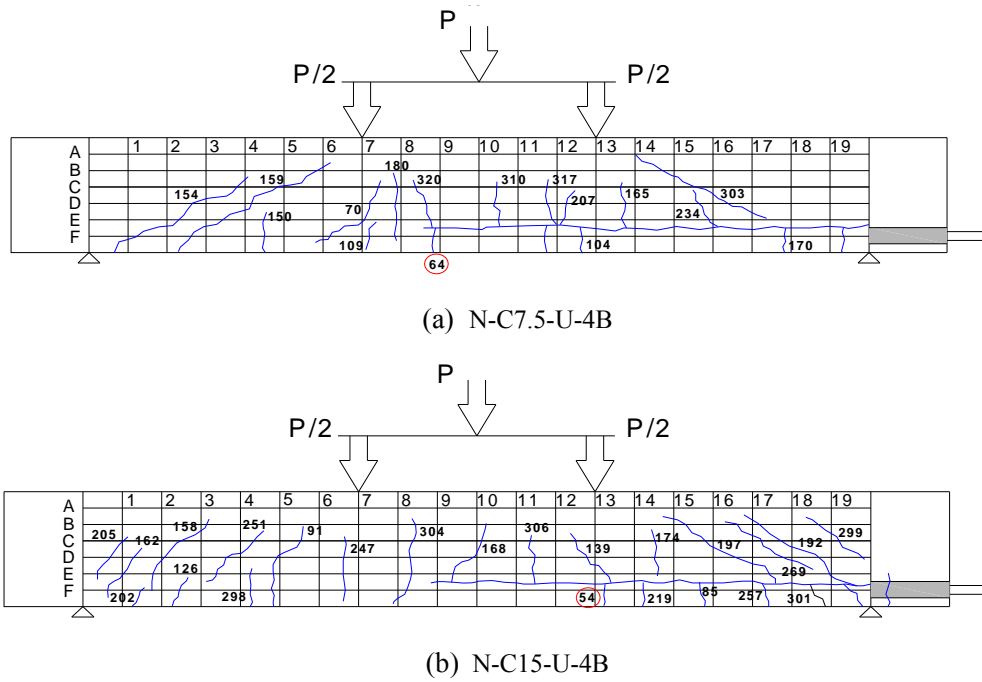
Figure 4.23: Load cracking Patterns for non-anchored beams

4.4.2 Effect of intentionally non- anchored longitudinal reinforcement

Since the shear span corrosion did not affect the structural behaviour of the anchored speci-mens, beam A-C7.5-U-4B can be considered a control (un-corroded) beam for the non- an-chored beam N-C7.5-U-4B. Figure 4.24(a) shows the load deflection curves for two beams: one with properly anchored reinforcement (A-C7.5-U-4B) and one with intentionally non-anchored reinforcement (N-C7.5-U-4B). Again, the yield load and the ultimate load were not affected by the use of intentionally non-anchored longitudinal reinforcement. However, it is evident that the beam with no end anchorage exhibited a pronounced 28.6% decrease in the flexural stiffness. The deflection at failure of the beam with the non-anchored reinforcement was 30% greater than the beam with the anchored reinforcement. An examination of Figure 4.24(b), load vs. end slip behaviour, provides an explanation of this result. The beam with non-anchored reinforcement began to slip close to failure due to the loss of bond at the an-chorage zone. The artificial loss of the bond at the end anchorage of the beam also affected

84

the load-induced cracking pattern: the beam with the non- anchored reinforcement exhibited of 22.22% fewer flexural cracks and 33.56 % less average crack spacing (Figure 4.25). Figure 4.26 illustrates modes of failure for these beams.
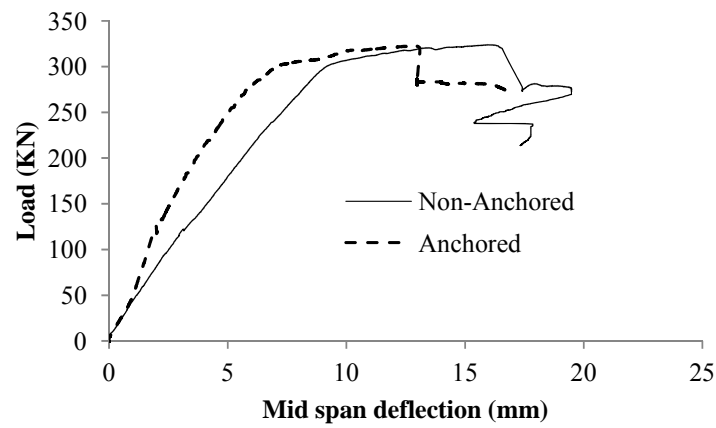
(a) Load-deflection relationship
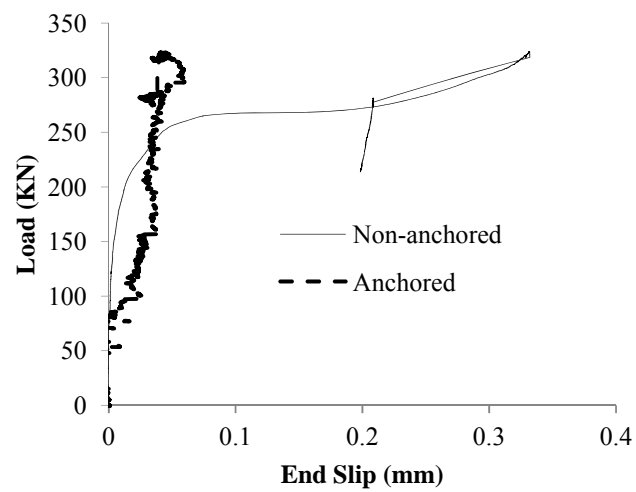
(b) Load-end slip relationship

Figure 4.24: Effects of the anchorage condition: anchored versus non-anchored

(a) A-C7.5-U-4B

(b) N-C7.5-U-4B
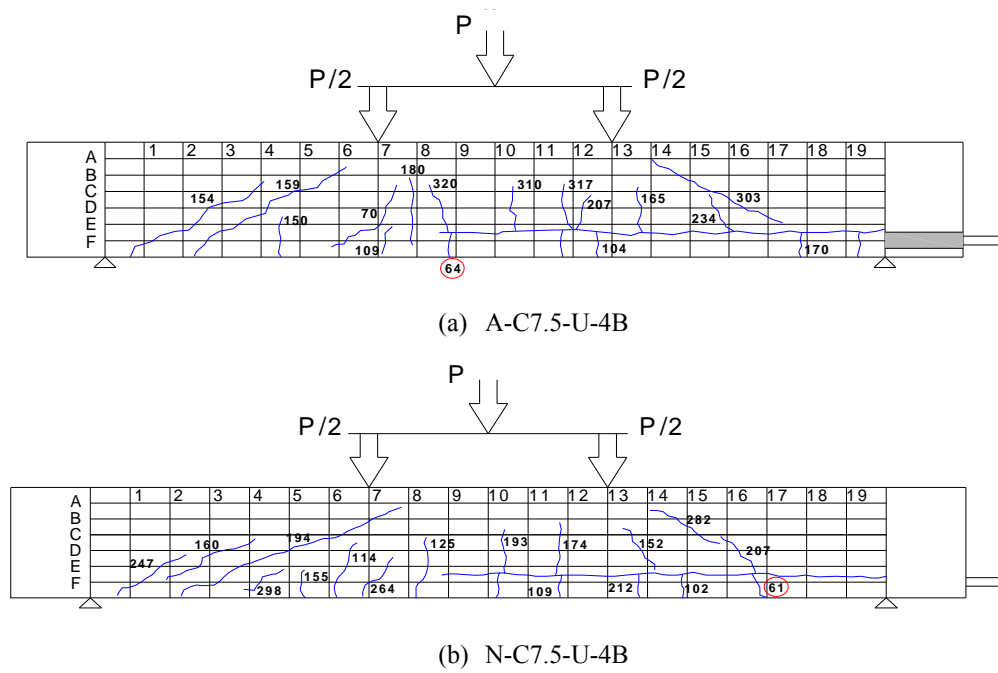
Figure 4.25: Effects of the anchorage condition: load cracking patterns

(a) A-C7.5-U-4B

(b) N-C7.5-U-4B
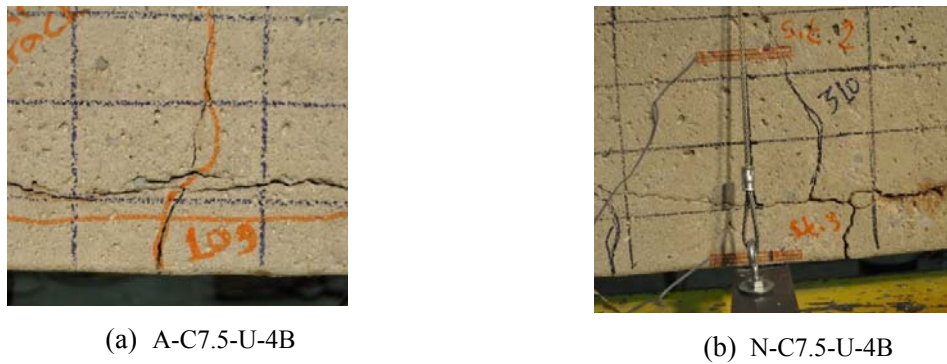
Figure 4.26: Effects of the anchorage condition: failure modes

4.4.3 Effects of repair systems

The following subsection discusses the effect of the type of repair system.

4.4.3.1 Patch repaired vs. GFRCM repaired beams with 7.5% theoretical corrosion mass loss

Figures 4.27(a) and 4.27(b) show the load-deflection curves and the load-end slip curves for three beams: corroded un-repaired (as control; N-C7.5-U-4B), corroded-patch repaired (N-C7.5-R(P)-4B), and corroded-GFRCM repaired (N-C7.5-R(GFRCM)-4B) beams. These three beams had the same steel mass loss following corrosion phase (Table 4.1). The following paragraphs provide a discussion on the effects of patch repair and GFRCM repair for shear-span corroded beams.

The patch repair has an adverse effect on the mode of failure and, therefore, on the flexural response (Figure 4.27 (a)). This can be attributed to the partial loss of the bond between the cleaned/corroded rebar and the patched concrete. The small aggregate size of the new patch (0 mm-8 mm) compared to the sound concrete (13 mm) reduces the friction component of the bond strength. The sandblasting of the corroded steel rebar (to clean it from rust) diminishes the height of the reinforcement ribs which, in turn weakens the mechanical interlock component of the bond strength. The patch-repaired beam exhibited a relatively large end slip because of the bond loss at the concrete-steel interface (Figure 4.27 (b)). The reduction in the load capacity was 14.6% and the decrease in deflection at failure was 53% in comparison to the corroded-un repaired beam. The failure mode changed from a ductile flexural failure to a brittle failure (Figure 4.28). The stiffness of the beams was not affected by the patch repair because the patched concrete has the same compressive strength as the sound concrete.

The GFRCM repair system (applied as U-wrap with fibers in transverse direction) significantly enhances the ductility of the repaired beam (80% increase over the corroded-un repaired beam) and provide post-ultimate flexural capacity after the crushing of the concrete. However, the GFRCM repair did not affect the yielding load or the ultimate load. The repaired beam exhibited a small end slip. The number of flexural cracks and average crack spacing increased by 28.6% and 15.2% respectively (Figure 4.29).
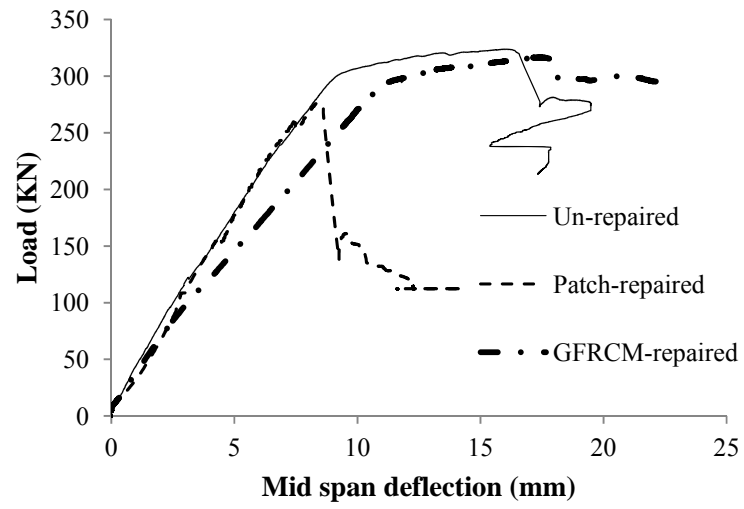
(a) Load-deflection relationship
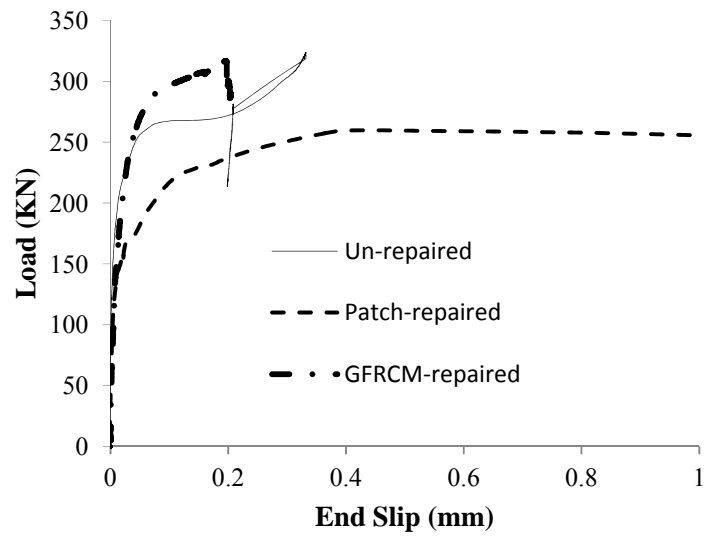
(b) Load-end slip relationship

Figure 4.27: Effects of the repair scenario: patched versus GFRCM (7.5% mass loss)
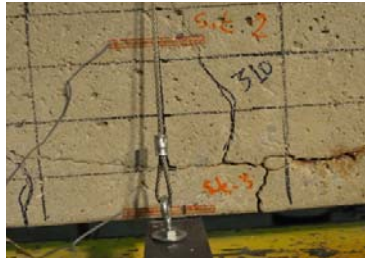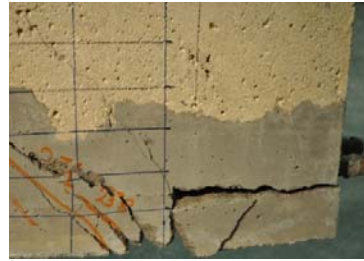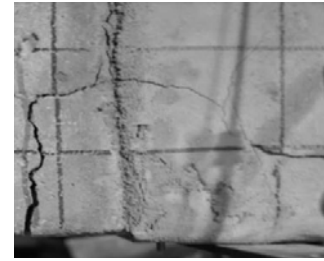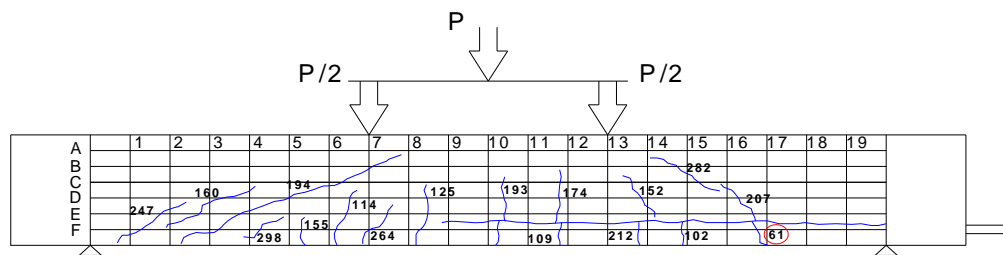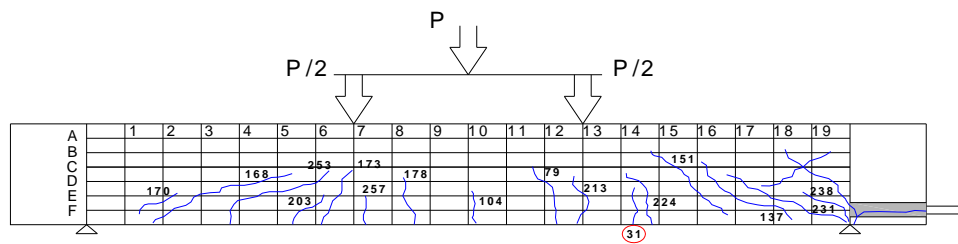
(a) N-C7.5-U-4B (b) N-C7.5-R(P)-4B (c) N-C7.5-R(GFRCM)-4B
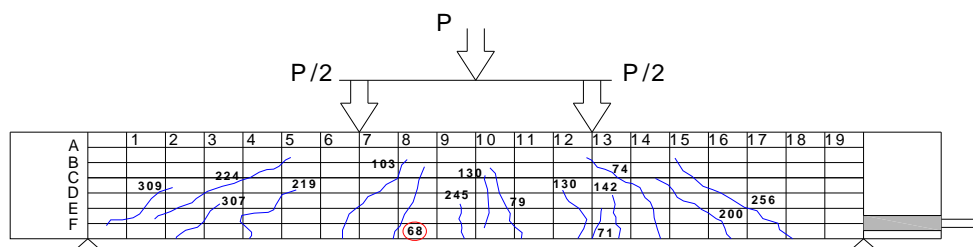
Figure 4.28: Effects of the repair scenario: failure modes

(a) N-C7.5-U-4B

(b) N-C7.5-R(P)-4B

(c) N-C7.5-R(GFRCM)-4B

Figure 4.29: Effects of the repair scenario: load cracking patterns

4.4.3.2 GFRCM repair versus CFRCM repair of beams with 15% mass loss

Figures 4.31(a) and 4.31(b) show the load-deflection curves and the load-end slip curves for two beams: corroded-patched-GFRCM-wrapped (N-C15-R(P+GFRCM)-4B) and corroded-patched-CFRCM-wrapped (N-C15-R(P+CFRCM)-4B) beams. These beams had the same steel mass loss following corrosion phase (Table 4.1). The CFRCM-wrapped beam had a slight 10.27% increase in stiffness. The CFRCM system provided better performance in terms of load-carrying capacity: the cracking load was increased by 18.87%, the yielding load by 21.92%, and the ultimate by 17.24% in comparison to the GFRCM repaired beam. The CFRCM-wrapped beam exhibited 9.29% improved ductility. Load-cracking behaviour was also affected: the CFRCM-wrapped beam showed 42% more flexural cracks, and 14% less average crack spacing (Figure 4.32). The CFRCM-wrapped beam provided superior confinement for the concrete, which prevented the initiation of free-end slip until a load 20% higher than that achieved with the GFRCM-wrapped beam (Figure 4.30 (b)). Figure 4.30 shows the failure modes for these beams.

(a) N-C15-R(P+GFRCM)-4B	(b) N-C15-R(P+CFRCM)-4B

Figure 4.30: Effects of the GFRCM vs. CFRCM repair scenario (15% mass loss): failure modes
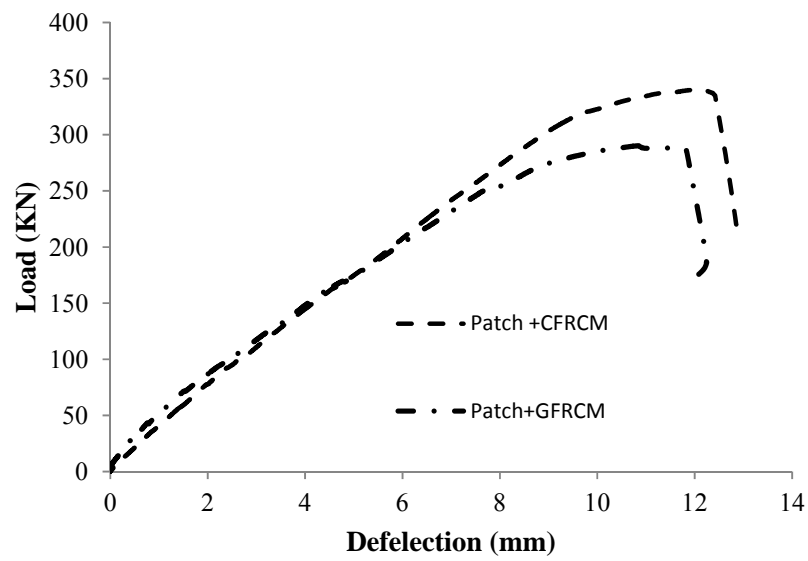
(a) Load-deflection relationship
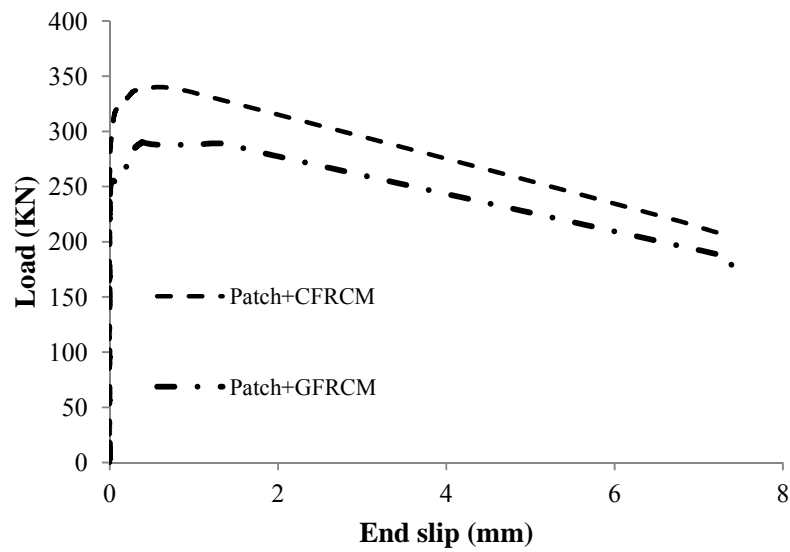
(b) Load-end slip relationship

Figure 4.31: Effects of the GFRCM vs. CFRCM repair scenario (15% mass loss)
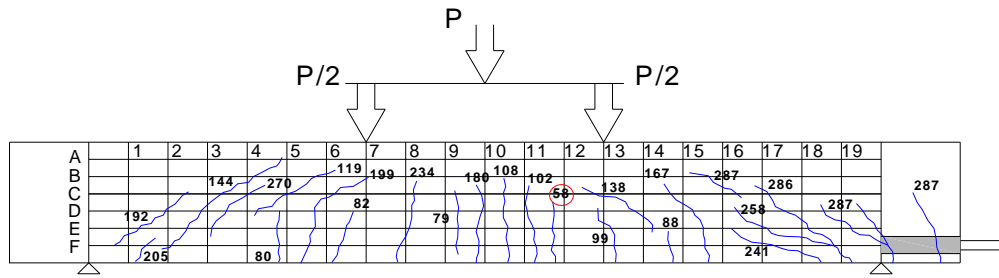
(a) N-C15-R(P+GFRCM)-4B
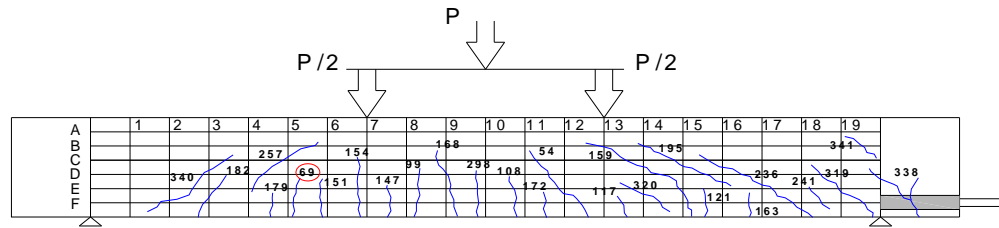
(b) N-C15-R(P+CFRCM)-4B

Figure 4.32: Effects of the GFRCM vs. CFRCM repair scenario (15% mass loss): load cracking patterns

4.4.3.3 Patch repair vs. CFRCM repair vs. patched-CFRCM repair of beams with 15% mass loss

Figures 4.33(a) and 4.33(b) show the load-deflection curves and the load-end slip curves for three beams: corroded-patch repaired, corroded-CFRCM wrapped, and corroded-patched-CFRCM wrapped beams. These beams had the same steel mass loss following the corrosion phase (Table 4.1). The comparison between the repair systems is relative because there was no corroded-unrepaired beam to serve as the control at this corrosion level.

It is obvious that the patch-repaired beam showed the poorest performance, and it was thereafter considered as the reference beam. The patch-repaired beam filed by bond-splitting failure. The poor performance can be attributed to the factors discussed in section 4.4.3.1. On the other hand, the CFRCM-repaired beam and the CFRCM-patch-repaired beam exhibited superior performance. The repair system enhanced the load-carrying capacity up to the level of the yielding load of tension steel, and changed the failure mode to a pull-out mode since the

repair provided higher confinement than the patch alone. The repair scenario did not affect the stiffness; the change in stiffness was in the range of 4.91%-8.23% over the reference beam. With the CFRCM system, the ultimate deflection was increased by 22.22% above that of the patched beam, and by 35.56% above that of the CFRCM-patched repaired beam. The cracking load of the CFRCM-repaired beam was 13.7% greater than that of the patched beam, whereas the cracking load of the combined CFRCM-patch-repaired beam was 5.48% lower than that of the patched beam. The ultimate load was significantly affected by the repair scenario. The CFRCM-repaired beam showed a 12.8% higher ultimate load than that of the patched beam, whereas the combined CFRCM-patch-repaired beam displays an 18% larger ultimate load than the patched beam (Figure 4.33(a)). The load-cracking behaviour is also affected by the repair scenario. In both the CFRCM repaired and the combined CFRCM-patch-repaired beams, 55% fewer flexural cracks were observed versus the patched beam (Figure 4.34).

The effect of the repair system on the structural performance can be explained by examining of the load-end slip curve shown in Figure 4.33(b). The CFRCM system provided sufficient confinement for the concrete to prevent the initiation of free-end slip until a higher load which was 13.62% greater than that of the patched beam. The combined CFRCM-patch repair system had the same effect until a load which was 16.34% above that of the patched beam. After failure, the load in the patched beam dropped rapidly as the slip increases. However, in the CFRCM-repaired beam, the load was maintained as the free-end slip increased from 0.25 mm to 0.5 mm, thus providing more ductile post-failure behaviour than was the patched beam. In addition, in the combined CFRCM-patch-repaired beam, the load was maintained as the free-end slip increased from 0.25 mm to 0.56 mm, thus providing even greater ductile post-failure behaviour than the patched beam. Figure 4.35 shows failure modes for these beams.
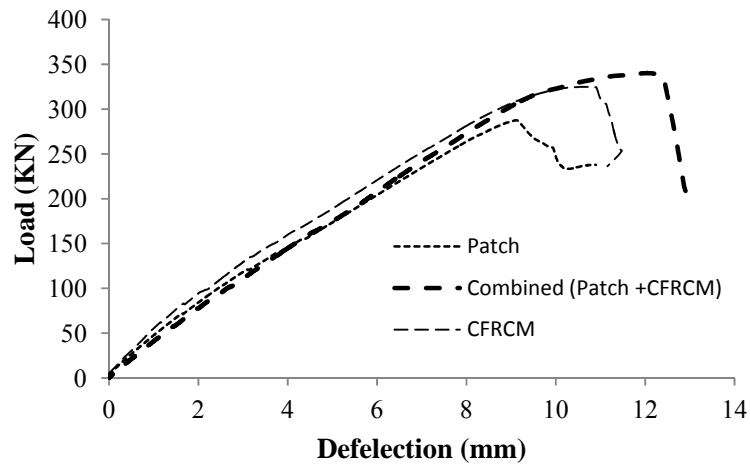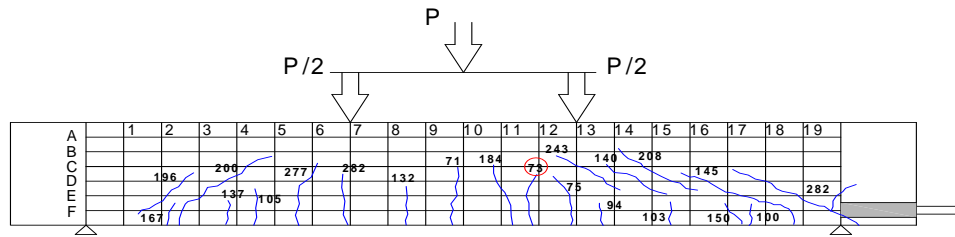
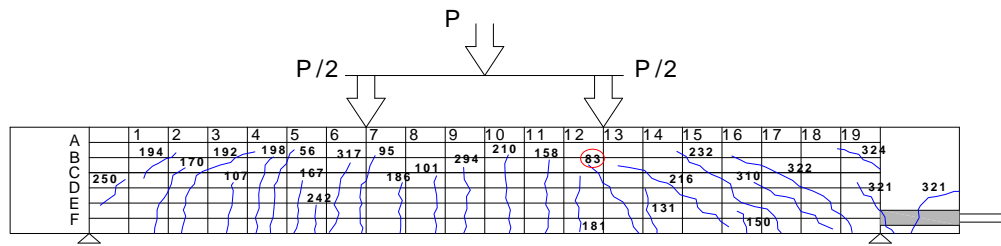(a) Load-deflection relationship
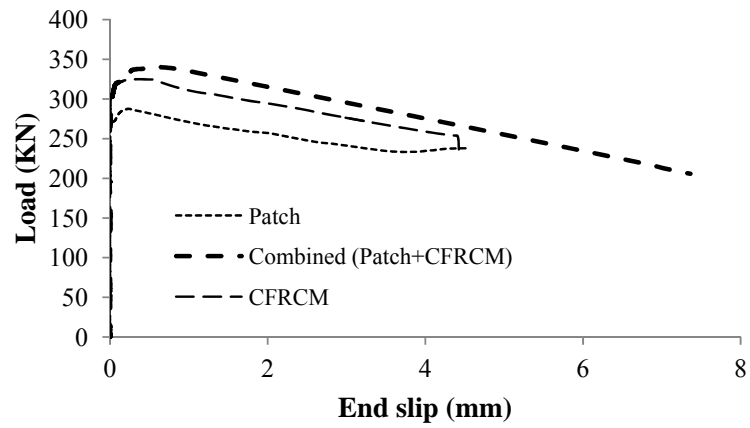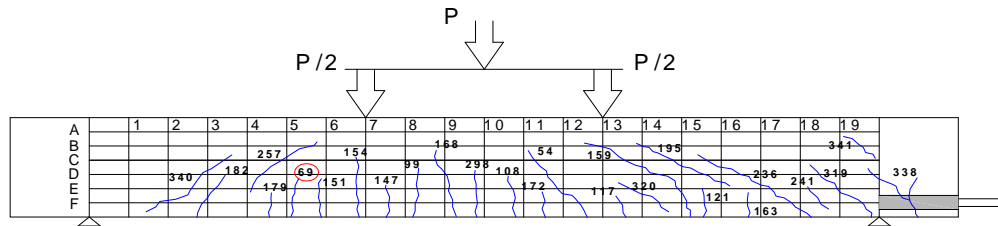

(b) Load-end slip relationship

Figure 4.33: Effects of the combined vs. single repair scenario (15% mass loss)
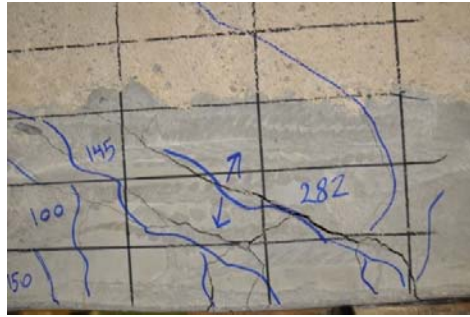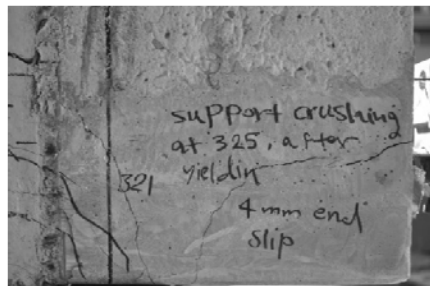
(a) N-C15-R(P)-4B

(b) N-C15-R(CFRCM)-4B

(c) N-C15-R(P+CFRCM)-4B

Figure 4.34: Effects of the combined vs. single repair scenario (15% mass loss): load cracking patterns

(a) N-C15-R(P)-4B

(b) N-C15-R(CFRCM)-4B

(c) N-C15-R(P+CFRCM)-4B

Figure 4.35: Effects of the combined vs. single repair scenario (15% mass loss): failure modes

Chapter 5
Analytical Modeling

5.1 Introduction

This chapter explains the programing of the analytical model of the nonlinear-load-deflection response for shear-span corroded beams. The model used is based on a model proposed by Maaddawy (2004). This chapter includes: a description of the program algorithm, predictions of the load-deflection curves for the different test specimens, and a comparison of the experimental and predicted results. Step-by-step calculation procedures and flowcharts are also provided.

5.2 Background

In this section, a mathematical model proposed by El Maaddawy (2004) to predict the nonlinear load-deflection relationship for corroded RC beams is described. The model was modified in this thesis to predict the behaviour of shear-span corroded beams. The following sections provide details of the original model.

5.2.1 Model philosophy

The beam is divided into a series of elements as shown in Figure 5.1. All elements are assumed to have the same length, which is equal to the mean stabilized crack spacing S_m. Stain compatibility and section analysis are applied at the center of each element, assuming a pure bending case for each crack. A single crack is assumed to initiate at the middle of each element when the concrete tensile strength is exceeded. As the crack is initiated, the steel stress reaches its maximum value at the middle of the element (crack location). However, the concrete is still contributing along the un-cracked zones of the element through tension stiffening (part of the tensile force is transferred from the steel to the concrete by the bond). As a result, the stress and strain are non-uniformly distributed along the length of the element. To account for the non-uniform distribution of the stress and strain, the relative movement between the steel and the concrete (steel slip) is addressed by the calculation the elongation of the

steel in terms of the average strain in the steel along the element. The elongation of the steel is then used for calculating the beam deflection. The model procedure is given below.
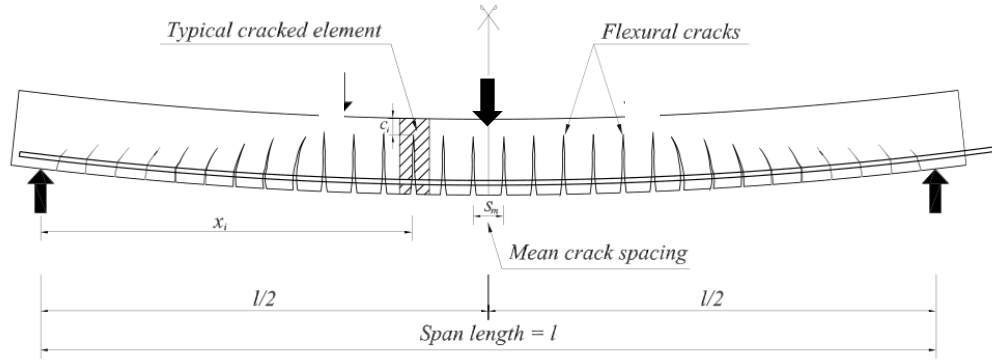

Figure 5.1: Beam model (Maaddawy, 2004)

A beam of span length l is divided into a number of elements each having a width of S_m. The number of elements within each half span is given by;

$$n = \frac{l}{2.S_m}$$

(5.1)

The mid-span deflection Δ of the beam is calculated based on the integration of the curvature along the beam length:

$$\Delta = \sum_{i=1}^{i=n} \phi_i x_i s_m$$

(5.2)

However from strain compatibility, it is known that:

$$\phi_i = \frac{\varepsilon_{si}}{d - c_i}$$

(5.3)

Substituting equation 5.3 into equation 5.2 produces:

$$\Delta = \sum_{i=1}^{i=n} \frac{\varepsilon_{si}}{d - c_i}.x_i.s_m$$

(5.4)

The steel elongation is represented as the product of the average steel strain and the length of the element, as follows:

$$e_i = \varepsilon_{si}.s_m \qquad (5.5)$$

Equation 5.4 can therefore be rewritten as:

$$\Delta = \sum_{i=1}^{i=n} \frac{e_i}{d - c_i}.x_i \qquad (5.6)$$

where;

n: the number of elements half the span;

e_i: the average elongation of the steel for element i;

d: i the depth of the steel reinforcement measured from the top of the compression fibers;

c_i: the depth of the neutral axis of element i;

x_i: the distance measured from the center of an element i to the beam support ; and

ε_{si}: the average steel strain along the length of element i.

ϕ_i : is the curvature of element i.

5.2.2 Material modelling

5.2.2.1 Concrete

Concrete in compression is assumed to follow a non-linear stress strain curve defined by the following equations:

$$f_c = f_c' \left[\frac{2\varepsilon_c}{\varepsilon_{co}} - \left(\frac{\varepsilon_c}{\varepsilon_{co}} \right)^2 \right] \qquad (5.7)$$

$$\varepsilon_{co} = \frac{2f_c'}{E_C} \qquad (5.8)$$

$$E_c = 4500\sqrt{f_c'} \ MPa \tag{5.9}$$

Concrete in tension is assumed to follow the linear-elastic equation proposed by CSA Standard A23.3-94:

$$f_r = 0.6\sqrt{f_c'} \ MPa \tag{5.10}$$

where;

f_c' : Compressive strength of concrete;

f_c : Concrete stress for a given concrete strain ε_c ;

f_r : Tensile strength of concrete;

ε_c : Concrete strain for a given stress f_c ;

ε_{co} : Concrete strain corresponding to the concrete compressive strength f_c' ; and

E_c : Modulus of elasticity of concrete.

5.2.2.2 Reinforcing steel

Steel reinforcement is assumed to follow an elastic-plastic-strain hardening curve:

$$f_s = \begin{cases} E_s \varepsilon_s & 0 \le \varepsilon_s \le \varepsilon_{sy} \\ f_y + E_{sp}\left(\varepsilon_s - \varepsilon_{sy}\right) & \varepsilon_{sy} \le \varepsilon_s \le \varepsilon_{su} \end{cases} \tag{5.11}$$

where;

f_s : Steel stress corresponding to strain ε_s ;

f_y : Steel yielding stress;

f_{su} : Steel ultimate strength;

ε_s : Steel strain corresponding to steel stress f_s ;

ε_{sy} : Steel strain corresponding to steel stress f_y ;

ε_{su} : Steel strain corresponding to the steel ultimate strength f_{su} ;

E_s : Modulus of elasticity of steel reinforcement before yielding; and

E_{sp} : Modulus of elasticity of steel reinforcement after yielding.

5.2.2.3 Calculation of the elongation of steel

As a result of crack formation at the middle of the element, stress and strain are distributed non-uniformly along the length of the cracked element. Figure 5.2 shows a typical cracked element and the variations in stress and strain along the length of the element.

A uniform distribution of the bond stress is assumed along the length of the cracked element, and equilibrium is applied as follows:

$$df_s\left(\frac{\pi.d_b^2}{4}\right) = \mu.\pi.d_b.dx \tag{5.12}$$

or;

$$\frac{df_s}{dx} = \frac{4.\mu}{d_b} \tag{5.13}$$

(a) Typical cracked element

(b) Variation of steel stress

(c) Variation of steel strain
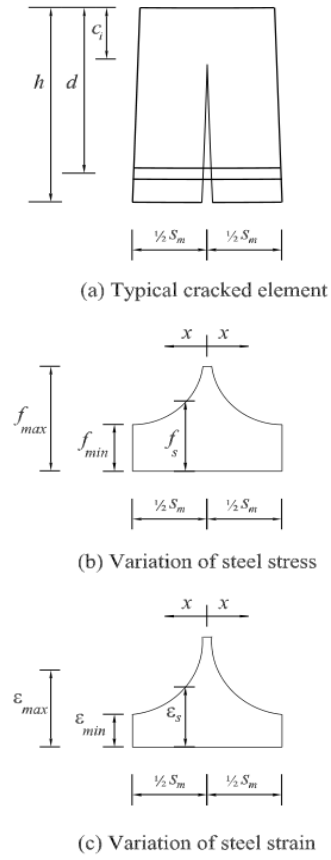
Figure 5.2: Typical cracked element with distribution of the stress and strain (Maaddawy, 2004)

where;

d_x : Length of the steel bar in the element;

df_s : Change in the steel stress over a length d_x ;

μ : Bond stress measured at distance x; and

d_b : Diameter of the steel bar.

The stress in the steel f_s as a function of the distance x within one-half the cracked element is given by:

$$f_s = f_{max} - \int_0^x \frac{4.\mu}{d_b} dx \qquad (5.14)$$

If a constant stress is assumed in the steel bar in an un-cracked half of the element, equation 5.13 can be rewrite as equation 5.14 as follows:

$$f_s = f_{max} - \frac{4.\mu}{d_b}.x \qquad (5.15)$$

The variation in the elongation of the steel bar over the length d_x can be represented as:

$$\frac{de_e}{d_x} = \varepsilon_s \qquad (5.16)$$

Based on elastic theory,

$$\varepsilon_s = \frac{f_s}{E_s} \qquad (5.17)$$

Combining equations 5.16 and 5.17 enables the calculation of the elongation of the steel bar in a cracked element in the pre-yield stage:

$$e_e = 2\int_0^{\frac{s_m}{2}} \frac{f_s}{E_s}.dx \qquad (5.18)$$

Combining equations 5.12 and 5.18, gives

$$e_e = \frac{s_m}{E_s}\left(f_{max} - \frac{\mu.s_m}{d_b}\right) \qquad (5.19)$$

where;

e_e : Elongation of the steel element in the pre-yielding stage;

s_m : Mean crack spacing;

103

f_{max} : Maximum steel stress at the middle of the cracked element;

E_s : Young's modulus of steel reinforcement;

d_b : Diameter of the steel bar; and

μ : Bond stress.

As the steel bar starts to yield, the deterioration of the bond spreads gradually along the length of the element. When the yield region covers the entire length of the element, the bond is completely lost. Maaddawy (2004) suggested an upper bound equation for the elongation of the steel in the post-yielding stage:

$$e_{p\,max} = \frac{S_m}{E_s}\left(f_y\right) + \frac{S_m}{E_{sp}}\left(f_{max} - f_y\right) \tag{5.20}$$

As long as the yielding stage does not encompass the entire length of the element, the elongation of the steel bar can be calculated as follows:

$$e_{ey} = \frac{S_m}{E_s}\left(f_y - \frac{\mu . S_m}{d_b}\right) \tag{5.21}$$

Therefore,

$$e_p = e_{ey} - e_{pinc} \tag{5.22}$$

$$e_p = \underbrace{\frac{S_m}{E_s}\left(f_y - \frac{\mu . S_m}{d_b}\right)}_{e_{ey}} + \underbrace{\frac{S_m}{E_{sp}}\left(f_{max} - f_y\right)}_{e_{pinc}} \tag{5.23}$$

Equations 5.23 and 5.19 are used to calculate the elongation of the steel bar as follows:

$$e_i = \begin{cases} \dfrac{S_m}{E_s}\left(f_{max} - \dfrac{\mu.S_m}{d_b}\right) & f_{max} \le f_y \\[4mm] \dfrac{S_m}{E_s}\left(f_y - \dfrac{\mu.S_m}{d_b}\right) + \dfrac{S_m}{E_{sp}}\left(f_{max} - f_y\right) & f_y \le f_{max} \le f_{su} \end{cases} \tag{5.24}$$

where;

e_i : Elongation of the steel bar within element i;

e_p : Elongation of the steel bar in the post-yielding stage;

e_{ey} : The elastic portion of the elongation of the steel bar;

e_{pinc} : Plastic portion of the elongation of the steel bar;

f_{su} : Ultimate strength of the steel bar; and

E_{sp} : Young's modulus of the steel bar in the post-yielding stage.

5.2.2.4 Bond stress-slip model

To determine the bond stress at the concrete-steel interface, a model based on the CEB Model Code (1990) was implemented to calculate the slip and the corresponding bond stress for each element. The model accounts for the effects of corrosion and wrapping repair (Maaddawy, 2004). The model equation is:

$$\mu = \begin{cases} \dfrac{d_b}{2.S_m}\left(f_{max} - n_s.f_r\right) & \mu \le \mu_{max} \\[3mm] \mu_{max} & s \le s_1 \\[3mm] \mu_{max} - \left(\mu_{max} - \mu_{friction}\right)\left(\dfrac{s - s_1}{s_2 - s_1}\right) & s_1 \le s \le s_2 \\[3mm] \mu_{friction} & s \ge s_2 \end{cases} \tag{5.25}$$

All of the parameters used to define the bond- slip relationship are as recommended by the CEB Model Code (1990), with the exception of the maximum bond strength μ_{max}, which is calculated according to the equation proposed by Maaddawy (2004):

$$\mu_{max} = \underbrace{(A_1 + A_2.m_1)}_{R} \underbrace{\left(0.55 + 0.24.\frac{c_c}{d_b}\right)\sqrt{f_c'}}_{\mu_{conc}} + \underbrace{0.191.\frac{A_t.f_{yt}}{s_s.d_b}}_{\mu_{st}} + \underbrace{\frac{0.06.A_{tf}.f_{ef}}{s_f.d_b}\sqrt{f_c'}}_{\mu_f} \qquad (5.26)$$

where;

μ : Bond stress for a given slip s ;

μ_{max} : Maximum bond stress;

$\mu_{friction}$: Bond strength based on friction;

μ_{conc} : Contribution of concrete to the bond strength;

μ_{st} : Contribution of stirrups to the bond strength;

μ_f : Contribution of wrapping repair to the bond strength;

s : Steel bar slip for a given bond stress μ ;

s_1 and s_2 : Constants taken from the CEB Model Code;

A_1 and A_2 : Constants that depend on the current level of corrosion density;

n_s : Modular ratio of steel to concrete;

f_r : Tensile strength of the concrete;

m_1 : Corrosion mass loss in the steel bar (%);

c_c : Concrete cover;

A_t : Cross-sectional area of the one stirrup;

A_{tf} : Area of the transverse fiber strip;

106

f_{yt} : Yield strength of the stirrups;

s_s : Center-to center spacing between stirrups;

s_f : Width of the fiber sheet;

f_{ef} : Effective stress in the fiber; and

R : Factor that accounts for the effect of corrosion on the bond strength.

5.2.2.5 Calculation of the mean crack spacing

The equation proposed by the CEB-FIP Model Code (1990) was used to estimate the mean crack spacing for a flexural member:

$$s_m = \frac{2}{3} \cdot \frac{d_b}{3.6\rho_{ef}}$$

(5.27)

$$\rho_{ef} = A_s / A_{cef}$$

(5.28)

where;

A_s : is the area of the tensile steel reinforcement, and

A_{cef} : is the effective embedment zone of the concrete, which is the area of the concrete that surrounds the tensile steel and has the same centroid as the steel.

5.2.2.6 Section analysis model

A layered section analysis model was used for the middle of each element for each load increment in order to determine the steel stress and the neutral axis depth. The model assumptions are as follows:

- The strain distribution is linear over the depth of the section;

107

- A perfect bond is assumed at the steel concrete interface;

- The strains in the concrete and the steel are equal at the same level along the beam section, with strain compatibility

Figure 5.3 illustrates the sectional analysis model; for which equations 5.29 and 5.30 produce the equilibrium requirements.

$$\int_{A_c} f_c.d.A_c + \int_{A_s'} f_s'.d.A_s' - \int_{A_{ct}} f_{ct}.d.A_{ct} - \int_{A_s} f_s.A_s - \int_{A_f} f_f.A_f = 0 \qquad (5.29)$$

$$\int_{A_c} f_c.y.d.A_c + \int_{A_s'} f_s'.y.d.A_s' + \int_{A_{ct}} f_{ct}.y.d.A_{ct} + \int_{A_s} f_s.y.d.A_s + \int_{A_f} f_f.y.d.A_f = M_{ext} \qquad (5.30)$$
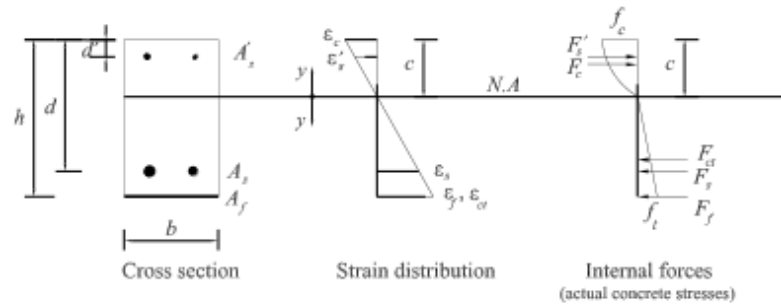
(a) **Pre cracking concrete analysis**
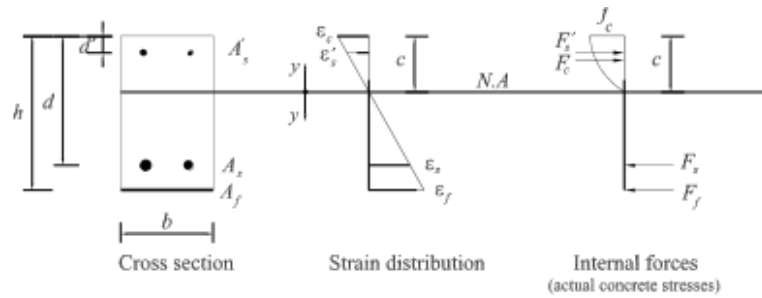
(b) **Post cracking concrete analysis**

(c)

Figure 5.3: Sectional analysis model (Maaddawy, 2004)

where;

h : Height of the section;

d : Depth of the tensile steel measured from the top face of the beam;

d' : Depth of the compression steel measured from the top face of the beam;

ε'_s : Strain in the compression steel;

ε_s : Strain in the tension steel;

ε_f : Strain in the longitudinal fiber sheet;

c : Depth of the neutral axis measured from the top face of the beam;

A_c : Area of the concrete in compression;

f_c : Concrete stress in compression;

A_{ct} : Area of the concrete in tension;

f_{ct} : Concrete stress in tension;

A'_s : Area of the compression steel reinforcement;

f'_s : Stress in the compression steel reinforcement;

A_s : Area of the tensile steel reinforcement;

f_s : Stress in the tensile steel reinforcement;

A_f : Area of the longitudinal fiber sheet;

f_f : Stress in the longitudinal fiber sheet;

y : Vertical distance measured for the neutral axis; and

M_{ext} : External applied moment.

The model proposed by Maaddawy (2004) was modified to predict the behaviour of shear-span corroded beams. This will be described in the following sections.

5.3 Program Concept and Layout

The principle behind model is to divide the beam into series of elements. Each element has a length equal to the mean crack spacing specified in design codes (Figure 5.1). The computer program generates load values with incremental increases of 1kN. For each load increment, the deflection is calculated based on the elongation of the steel reinforcement within each element. The flowchart of the main algorithm of the program is illustrated in Figure 5.4. The program includes four sub-models (subroutines) connected to the main algorithm (Figure 5.5): the structural analysis model, the layered section analysis model, the elongation-bond-slip model, and the mid-span deflection model. Figures 5.6 through 5.9 illustrate the flow-charts for the four subroutines. The tasks and calculation procedures for the main algorithm and the subroutines are described in the following sections.

5.3.1 The structural analysis model

The task of the structural analysis model is to use conventional structural analysis to calculate the external applied moments M_{ext} within the center of each element for each load increment P (Figure 5.3). The model is composed of the two load configurations considered in this study: a 3-point-load-configuration and a 4-point-load-configuration. The calculation procedure is as follows:

Based on Equation 5.1, for a given number of elements n, with a beam span-length l, a load P, and a load arm a;

1- Calculate the element arm x_i:

$$x_i = \left(\frac{(l/2)}{n} \right) \tag{5.31}$$

2- Identify the load configuration type
- For a 3-point-bending configuration:

$$M_{ext,i} = \frac{P.x_i}{2} \qquad \text{for } 0 \leq x_i \leq \frac{l}{2} \tag{5.32}$$

- For a 4-point-bending configuration:

$$M_{ext,i} = \begin{cases} \dfrac{P.x_i}{2} & \text{for } 0 \leq x_i \leq a \\[2mm] \dfrac{P.a}{2} & \text{for } a \leq x_i \leq \dfrac{l}{2} \end{cases} \tag{5.33}$$

111
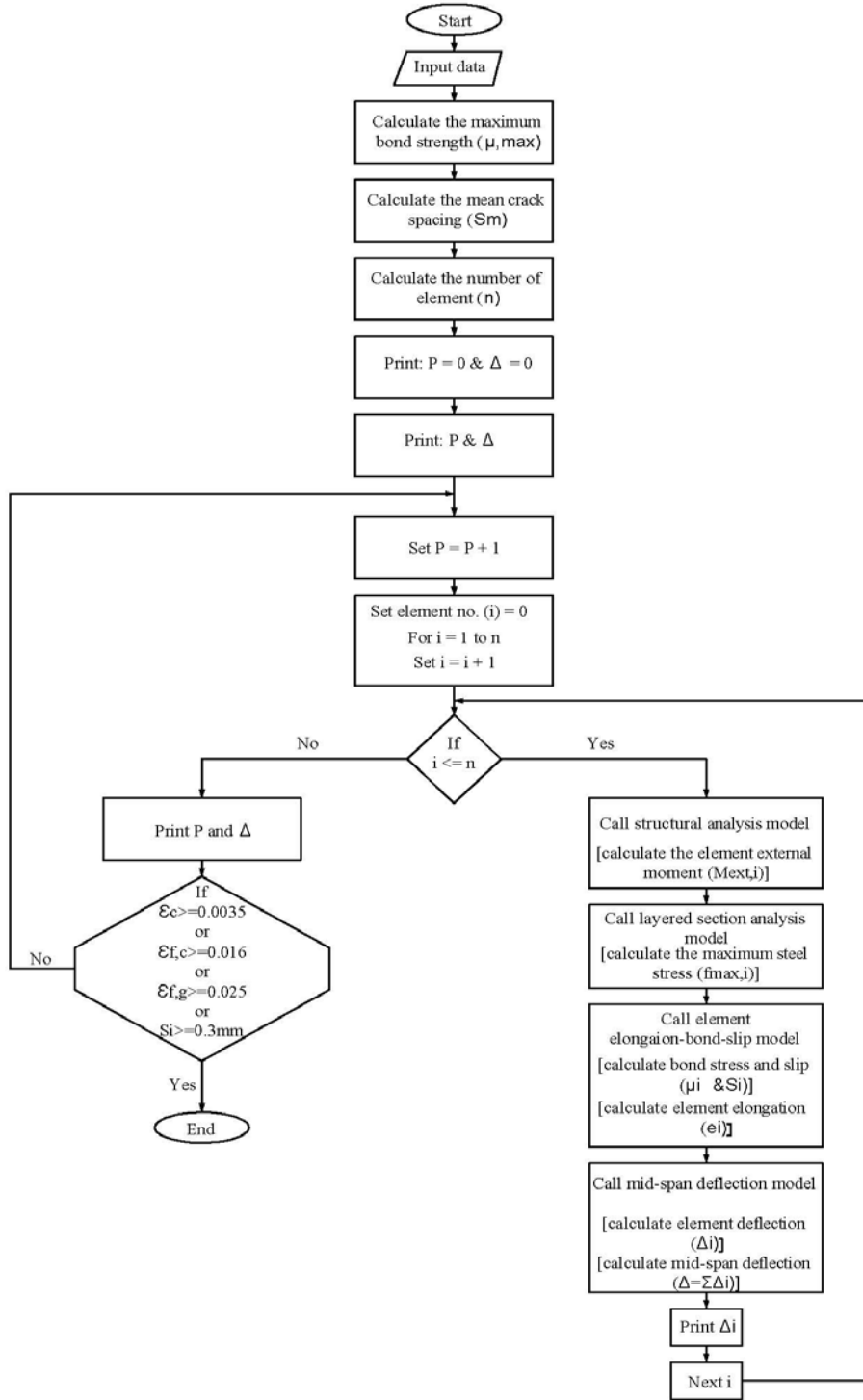
Figure 5.4: Flowchart of the main algorithm of the program

112
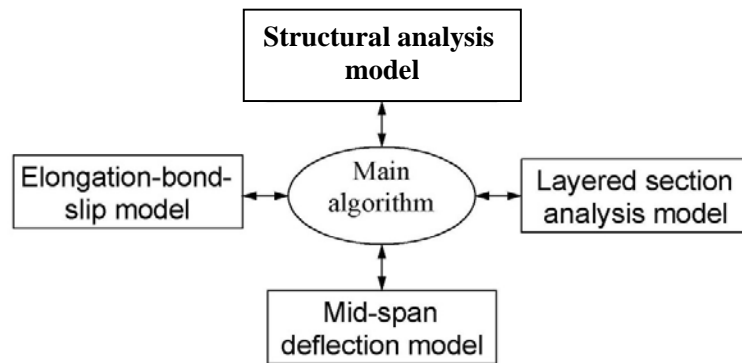
Figure 5.5: Subroutines connected to the main algorithm
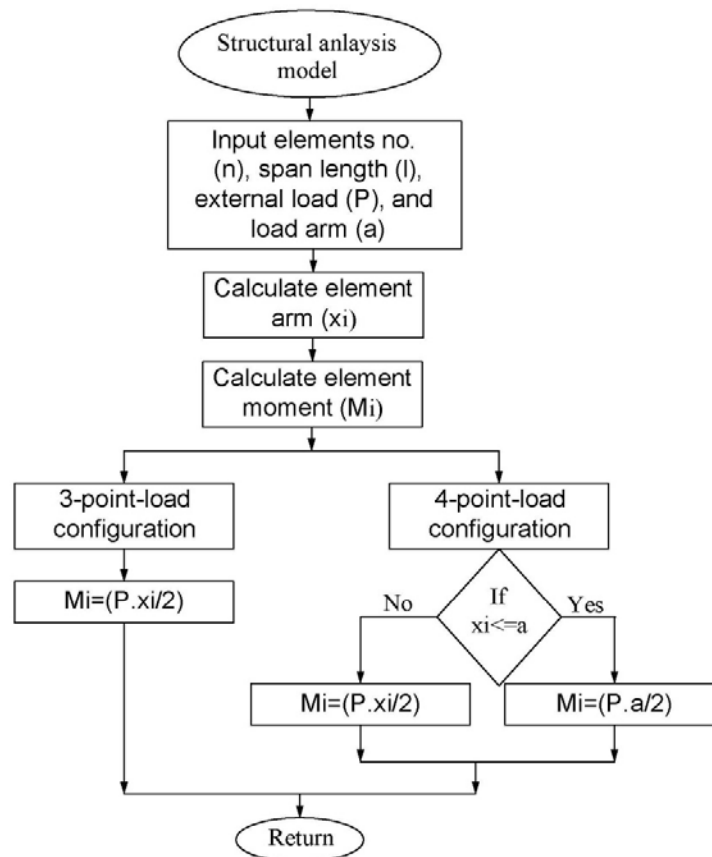
Figure 5.6: Flowchart of the structural analysis model

5.3.2 The layered-sectional analysis model

The task of the layered sectional analysis model is to analyze the beam section for a given external moment M_{ext} within each element for a given load in order to determine the maximum stress in the reinforcing steel $f_{s,max}$ (Figure 5.7). The calculation procedure is as follows:

1- Assume a strain at the extreme compression fiber of the concrete ε_c, and a neutral axis c.

2- Calculate the concrete strain, and stress in each concrete layer based on Figure 5.3 and Equation 5.7.

3- Calculate the fiber strain, and stress based on Figure 5.3.

4- Calculate the bottom and top steel strains and stresses using Figure 5.3 and Equation 5.11.

5- Apply the equilibrium conditions according to Equations 5.29 and 5.30.

6- Vary the concrete top strain and neutral axis until the equilibrium conditions are satisfied.

5.3.3 The elongation-bond stress-slip model

The task of the elongation-bond stress-slip model is to calculate the steel elongation for each element using the bond-slip model described in subsection 5.2.2.4 (Figure 5.8). The calculation procedure is as follows:

1- Recall the maximum bond strength

2- Identify the end anchorage condition: anchored or non-anchored (Appendix E)

- For beams with end anchorage, use the confined case defined by the CEB Model Code to determine the bond-slip parameters: S_1=3 mm, S_2=15 mm and $\mu_{friction}$=0.4 $\mu_{max.}$

- For beams with inadequate end anchorage, new values of : S_1=0.5 mm, S_2=6 mm, and $\mu_{friction}$ =0 were proposed based on experimental observations.

3- Identify the loading stage: un-cracked ($M_{ext} <= M_{cr}$) or cracked ($M_{ext} >= M_{cr}$)

- For an un-cracked stage use Equation 5.19 to calculate the elongation of the steel

- For a cracked stage use Equation 5.24 to calculate the elongation of the steel reinforcement.
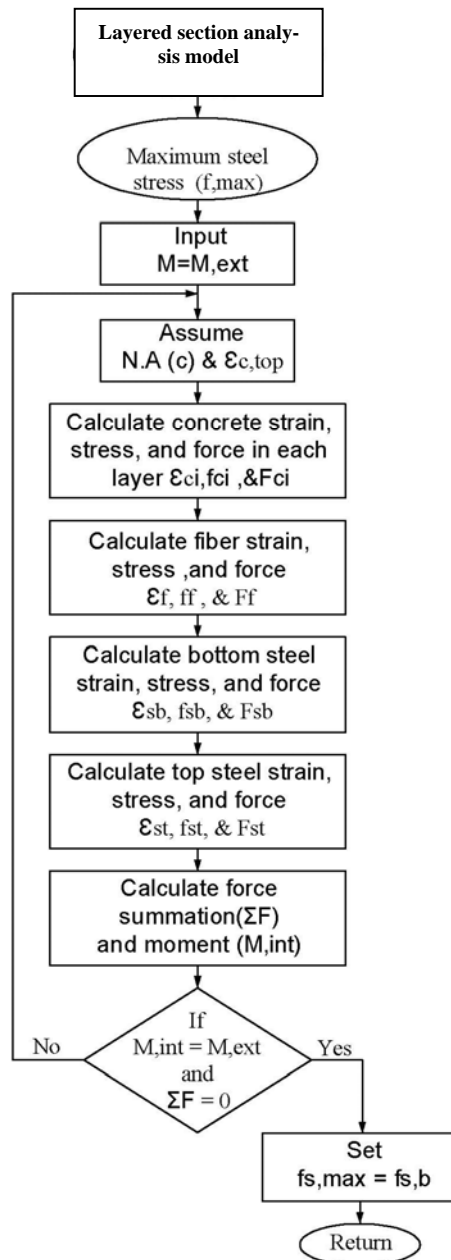
Figure 5.7: Flowchart of the layered section analysis model
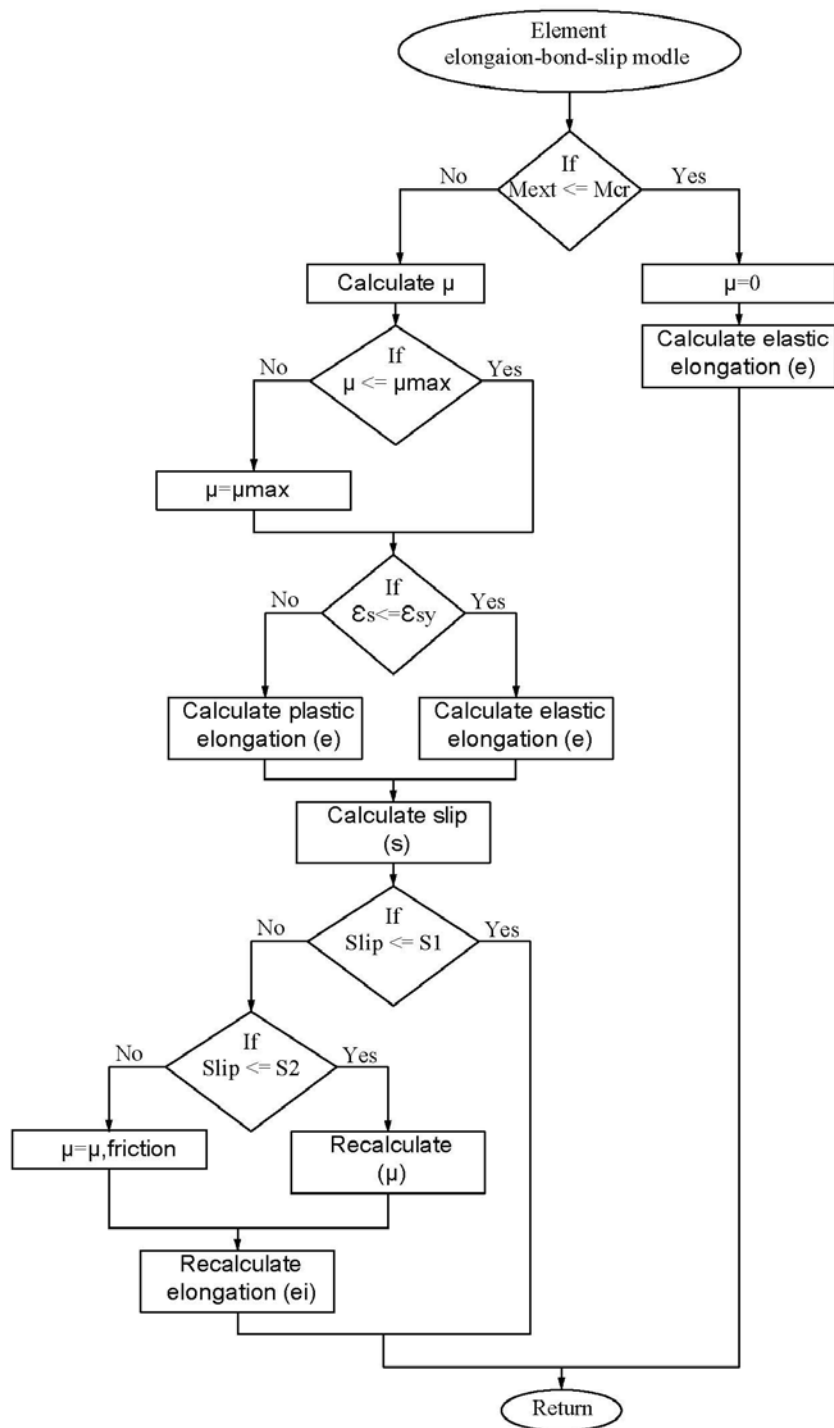
Figure 5.8: Flowchart of the elongation-bond-slip model

5.3.4 The mid-span deflection model

The task of the mid-span deflection model is to calculate the mid-span deflection (Figure 5.9). The calculation process can be summarized in one step: for a given element arm x_i, neutral axis c, and element elongation e, calculate the mid-span deflection for each load according to Equation 5.4.

It is important to note that for beams with a corroded shear-span, the deflection is calculated as the average of the deflections of a virgin beam with an un-corroded span and a beam with a corroded span.
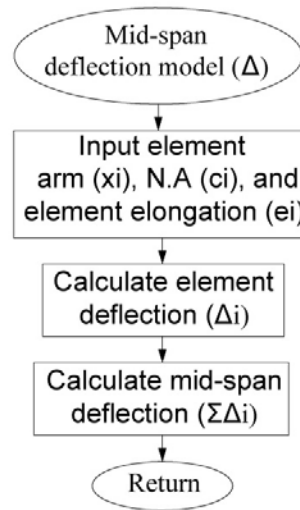
Figure 5.9: Flowchart of the mid-span deflection model

5.3.5 The main algorithm

The task of the main algorithm is to combine the four subroutines (Figure 5.4). The general procedure is as follows:

1- Input the material and geometric properties.
2- Calculate the maximum bond strength μ_{max} using Equation 5.26.
3- Calculate the mean crack spacing S_m using Equation 5.27.
4- Calculate the number of elements n using Equation 5.1.
5- Generate load values P.

6- Cal the structural analysis mode to calculate the moment in each element M_{ext}.

7- Call the layered section analysis model to calculate the maximum steel stress $f_{s,max}$.

8- Call the elongation-bond-slip model to calculate the steel elongation e.

9- Call the mid-span deflection model to calculate the mid-span deflection Δ.

10- Check the failure mode conditions: concrete crushing, fiber rupture, or bond.

5.4 Program Coding and Modes of Failure

The program was coded using the Visual Basic for Applications programming language integrated with the Microsoft Excel interface. The program was designed to stop if one of the following modes of failure occurred.

- Flexural failure: concrete crushing when $\varepsilon_{c,top} >= 0.0035$

- Fiber rupture: when $\varepsilon_{f,\,carbon} >= 1.6\%$ or $\varepsilon_{f,glass} >= 2.5\%$

- Bond failure: when steel slip $S >= 0.3$ mm

Figure 5.10 illustrates the possible modes of failure.
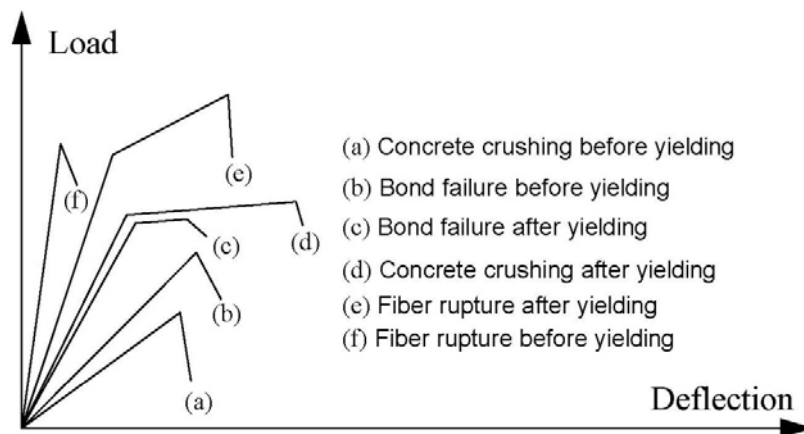
Figure 5.10: Possible modes of failure

118

5.5 Verification of Results

The test specimens were analyzed using the program presented in this Chapter. The load-deflection predictions produced by the model were compared with the experimental results. The comparisons are illustrated in Figures 5.11 through 5.13. Table 5.1 gives the absorbed percentage error values between the experimental and the predicted values for both the pre-yielding and the post-yielding stages.

Table 5.1 and Figures 5.11 through 5.13 show that the load-deflection curves predicted by the model are generally in reasonable agreement with the experimental results. With respect to the yielding stage, the comparison showed that 45% of the predicted yield loads are within a 5% error band and that 70% of the yield loads are within a 10% error band, whereas 61% of the yield deflections are within a 10% error band. For the ultimate stage, on the other hand, the table showed that 70% of the ultimate loads are within a 5% error band and that 100% of the ultimate loads are within a 10% error band, whereas 77% of the ultimate deflections are with a 15% error band.

It is important to note that the model overestimated the ultimate and yield capacities for patch-repaired beams, a result that could be attributed to the adverse effect of the sandblasting process, which reduced the heights of the ribs at the surface of the steel rebars. This affected the bond at the corroded steel-to-patch interface.

Table 5.1: Comparison of the experimental and predicted results

Specimen	Experimental				Predicted				*Error (%)			
	Py (kN)	Δy (mm)	Pu (kN)	Δu (mm)	Py (kN)	Δy (mm)	Pu (kN)	Δu (mm)	Py	Δy	Pu	Δu
A-C0-U-3B	209	7.5	250	23	225	8.95	254	23.6	+7.66	+19.33	+1.60	+2.61
A-C2.5-U-3B	224	11	239	17	224	8.56	254	22.7	0.00	-22.18	+6.28	+33.53
A-C5-U-3B	214	7	255	21	225	8.13	253	20.56	+5.14	+16.14	-0.78	-2.10
A-C7.5-U-3B	212	7	244	22	255	7.55	254	24.7	+20.28	+7.86	+4.10	+12.27
N-C7.5-U-3B	222	8.5	260	23	226	9.24	253	21.6	+1.80	+8.71	-2.69	-6.09
A-C7.5-U-4B	300	7	322	13	305	6.4	324	12.29	+1.67	-8.57	+0.62	-5.46
N-C7.5-U-4B	305	9	323	17	296	8.29	325	17.46	-2.95	-7.89	+0.62	+2.71
N-C15-U-4B	295	10	313	15	305	9.81	318	15.08	+3.39	-1.90	+1.60	+0.53
N-C15-R(P)-4B	-	-	288	9	305	9.46	305	10.27	-	-	+5.90	+14.11
N-C15-R(GFRCM)-4B	-	-	270	7.5	-	-	296	8.29	-	-	+9.63	+10.53
N-C15-R(P+GFRCM)-4B	260	8.3	290	11.6	305	9.05	317	13.36	+17.31	+9.04	+9.31	+15.17
N-C15-R(CFRCM)-4B	297	8.5	325	11	319	9.22	327	10.93	+7.41	+8.47	+0.62	-0.64
N-C15-R(P+CFRCM)-4B	317	9.6	340	12.2	319	9.49	341	15.33	+0.63	-1.15	+0.29	+25.66

*Error (%) = 100x(Predicted –Experimental)/(Experimental)

Beam A-C0-U-3B

Beam A-C2.5-U-3B

Beam A-C5-U-3B

Beam A-C7.5-U-3B
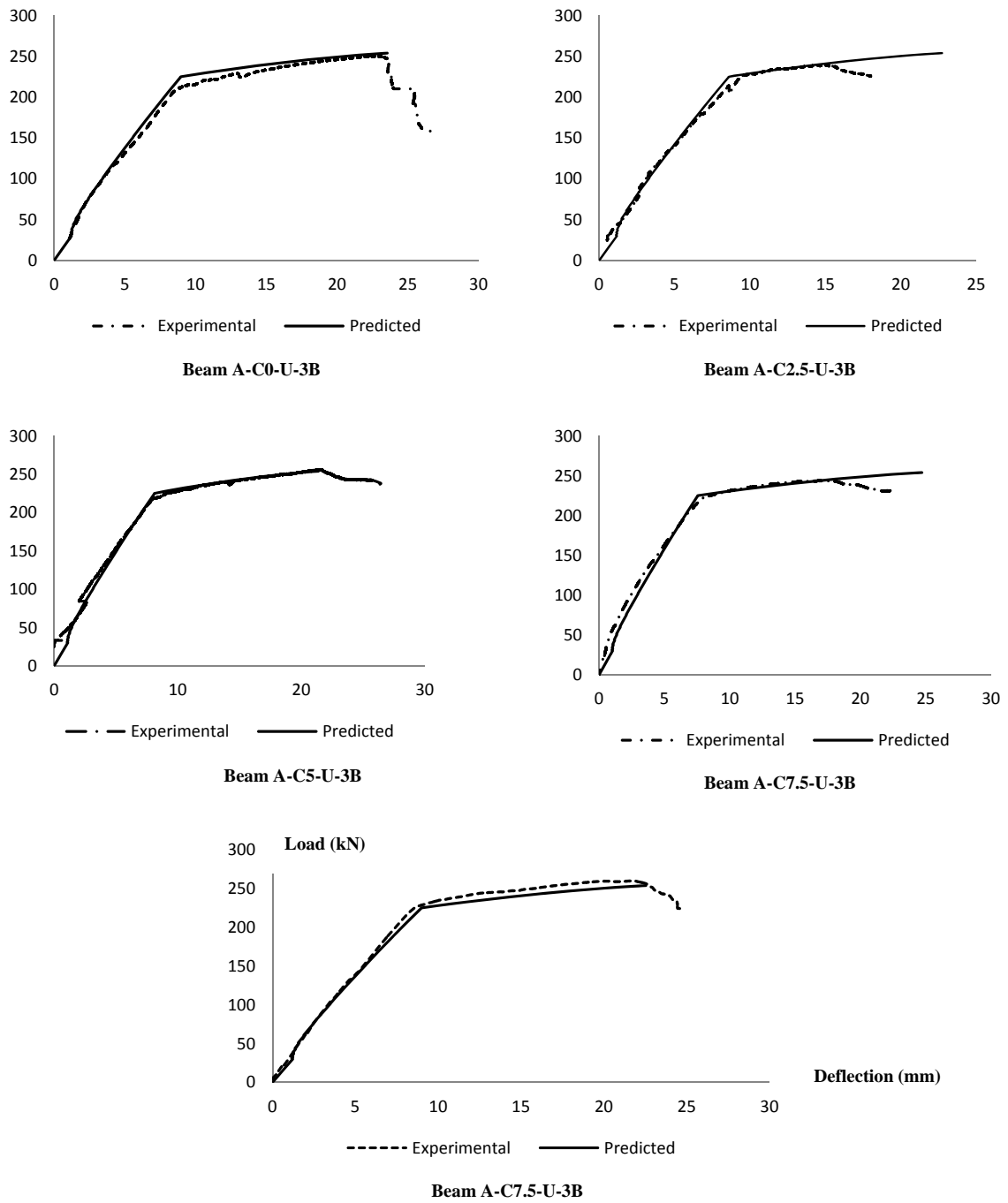
Beam A-C7.5-U-3B

Figure 5.11: Experimental and predicted load-deflection responses (anchored beams in a 3-point bending configuration)
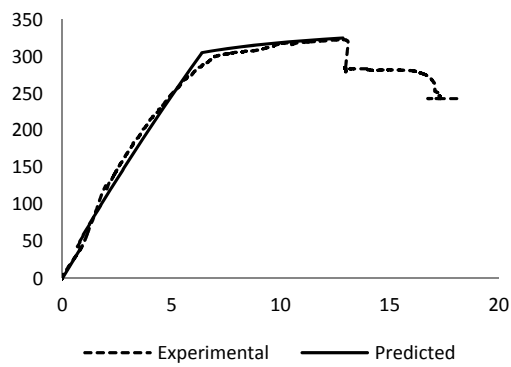
Beam A-C7.5-U-4B
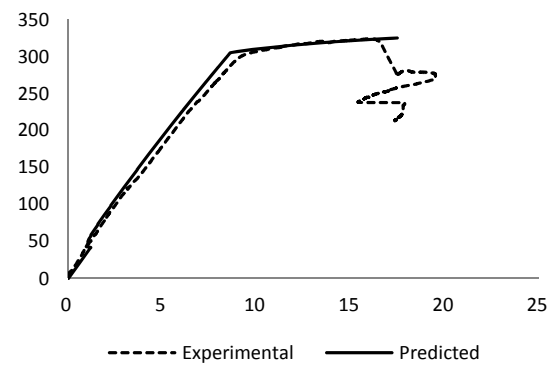
Beam N-C7.5-U-4B
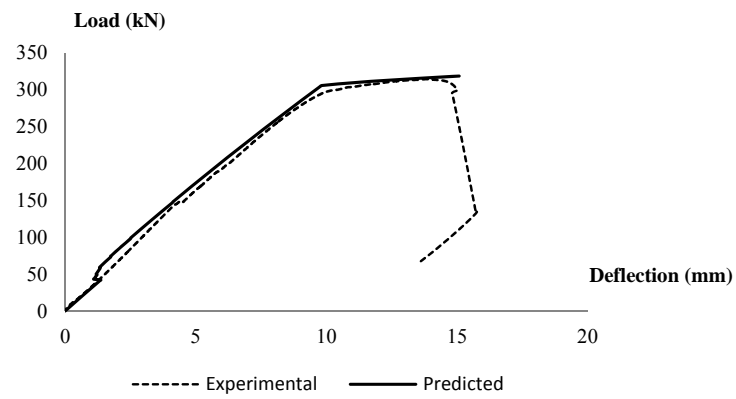
Beam N-C15-U-4B

Figure 5.12: Experimental and predicted load-deflection responses (un-repaired beams in a 4-point bending configuration
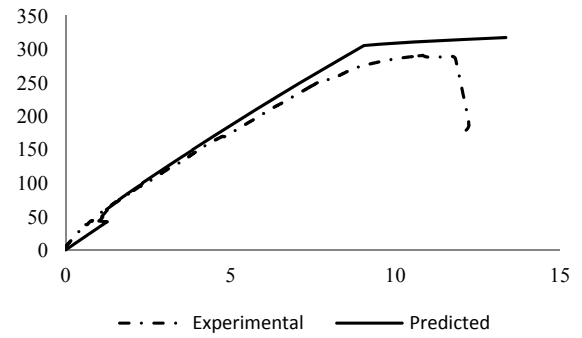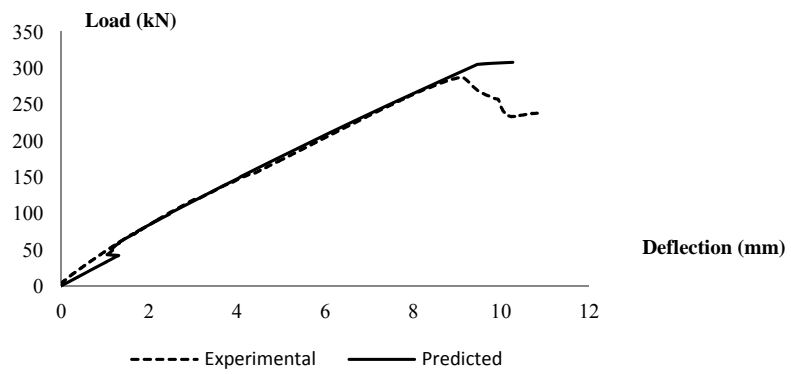
121
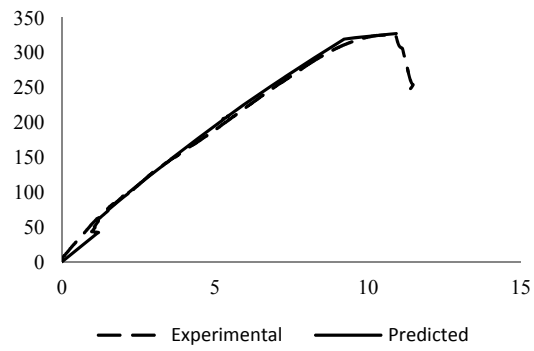
Beam N-C15-R(CFRCM)-4B
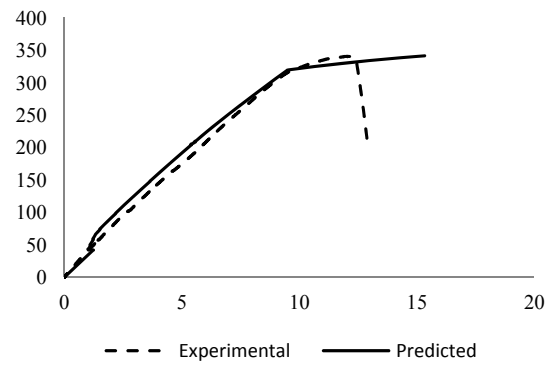
Beam N-C15-R(P+CFRCM)-4B
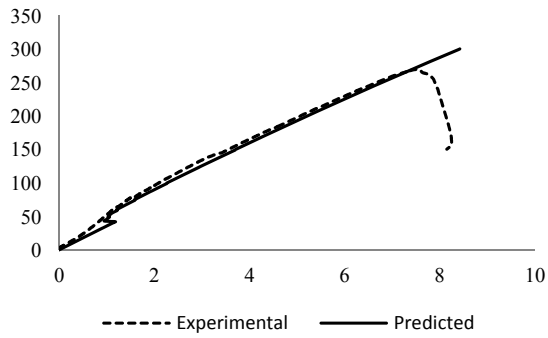
Beam N-C15-R(GFRCM)-4B

Beam N-C15-R(P+GFRCM)-4B

Beam N-C15-R(P)-4B

Figure 5.13: Experimental and predicted load-deflection responses (repaired beams in a 4-point bending configuration)

Chapter 6

Conclusions and Recommendations

6.1 Summary and Conclusions

The literature review highlighted the fact that, until now, little attention has been given to studying the effects of localized corrosion on the structural behaviour of RC beams, or the effectiveness of fiber-reinforced-cement-based composite (FRCM) systems as a repair method in such cases. The review also indicated no previous effort to develop models that can predict the load-deflection response of RC beams with partial span corrosion. The research work undertaken in this thesis aimed to address these gaps in the state of the art.

The effectiveness of different repair scenarios with respect to the rehabilitation of localized deteriorated zones in reinforced concrete beams was investigated both experimentally and analytically. The experimental comprised of 15 medium-scale reinforced concrete beams, 150 mm x 350 mm x 2400 mm each. Test variables included: the corrosion level (0%, 2.5%, 5%, 7.5% and 15% mass loss); the end anchorage condition of the tension reinforcement (anchored and non-anchored); the loading configuration (3-point bending and 4-point bending); and the repair technique (patching and U-wrapping with FRCM). Both the corrosion results and the load test results were analyzed and discussed in detail. An analytical model was implemented to predict the load-deflection responses for the test specimens. The experimental and predicted results were then compared. The following points highlight the relevant conclusions and observations:

- Due to the relatively large 40 mm concrete bottom-cover, all of the corroded beams had two bottom cracks along the corroded zone; parallel to the two main longitudinal tensile reinforcing rebars.

- The widths of corrosion cracks increased over time at an average rate of 0.02 mm per day. The maximum crack widths observed at the end of the corrosion phases were 0.5 mm, 1.0 mm, 1.21 mm, and 2.25 mm at 30 days, 60 days, 90 days, and 180 days respectively.

- The corrosion of the longitudinal reinforcement in the shear span had no significant effect on the structural behaviour of the RC beam that had properly anchored longitudinal reinforcement. The change in yielding load was less than 10%, and the change in the ultimate loads was less than 5% in comparison to the control (un-corroded) beam. The change in flexural stiffness was also less than 10% in comparison to the control (un-corroded) beam. The loading crack pattern was noticeably affected: the number of flexural cracks decreased by up to 50%.

- Medium corrosion in the intentionally un-bonded reinforcement in the anchorage zone significantly reduced the stiffness of the shear span corroded RC beams by 28.6%. The end slip was noticeably increased with no change in the mode of failure. On the other hand, severe corrosion of the intentionally un-bonded reinforcement in the anchorage zone had a substantial effect: the ductile flexural mode changed to a bond pull-out failure, with a noticeable 20% and 17% reduction in the beam stiffness and ductility; respectively. The severe level of corrosion was associated with bar slip.

- The patch repair system had an adverse effect on the flexural behaviour and the mode of failure of the RC beams with shear-span medium and severe corrosion and improperly anchored longitudinal reinforcement. The ultimate load decreased by 14.6% and the deflection at the ultimate load was reduced by 53%. The mode of failure was changed dramatically from a ductile flexural failure to a bond-splitting failure.

- GFRCM repair enhanced the flexural ductility of the RC beams with shear-span medium corrosion and improperly anchored longitudinal reinforcement. The increase in section ductility was up to 40%. The yield and ultimate loads were not affected by this strengthening system, whereas in the case of severe corrosion, the combined patch-GFRCM repair failed to restore the original capacity of the beam, and bond failure occurred.

- The capacity of the repaired beam was restored by CFRCM repair, whereas the combined patch-CFRCM repair increased the original capacity by 6%. Although neither

124

scenario resulted in the return of the ductile flexural mode of failure, bond failure could be delayed to a point beyond the yielding point.

- An analytical model that can predict the nonlinear load-deflection response of both corroded and corroded-repaired beams was developed and coded using the Visual Basic for Application programing language. A comparison of the predicted with the experimental curves revealed a reasonable agreement.

6.2 Recommendations for Future Research

This research assessed, for different corrosion levels and loading conditions, the structural behaviour of corrosion-damaged reinforced concrete beams. An additional contribution was to understand of the efficiency of conventional repair techniques for fixing the resulting deterioration. However, some additional topics require further investigation and /or verification. The following areas are recommended for future investigation:

- Additional examination of the effect of localized corrosion damage in RC elements is required with respect to different materials and geometric properties in order to generalize the effects and to provide additional understanding of the issues involved.
- Further applications using different repair schemes and types of fibers could help with the identification of an optimally effective repair method.
- Further testing directed at determining the bond strength properties of selected patch-repaired concrete is mandatory in order to avoid unexpected deficiencies in the application of such repairs in bond-damaged zones, and to ensure a reasonable compatibility between sound and new concrete; especially with respect to aggregate size.
- Appropriate careful measures for applying the concrete removal method should be developed, with the goal of preventing the formation of microcracks through the sound concrete.
- Sand-blasting and water-blasting procedures for cleaning concrete-removal zones should be explored because these processes can cause the ribs of the reinforcing steel

rebars to erode, and subsequently affect the bond between the steel and the new concrete patch.

Appendix A

Load-Cracking Patterns
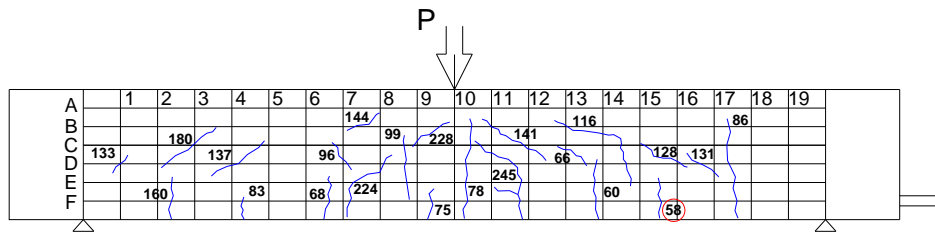
Figure A.1: Load-Cracking pattern of specimen A-C0-U-3B
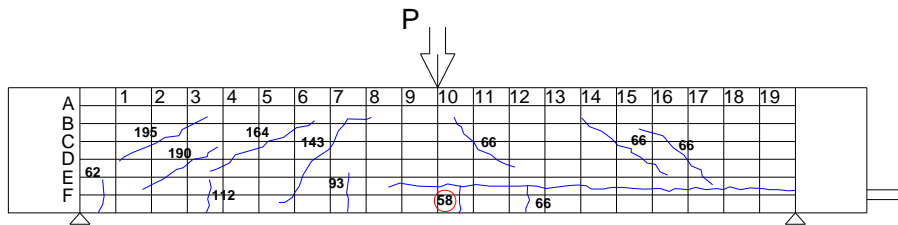
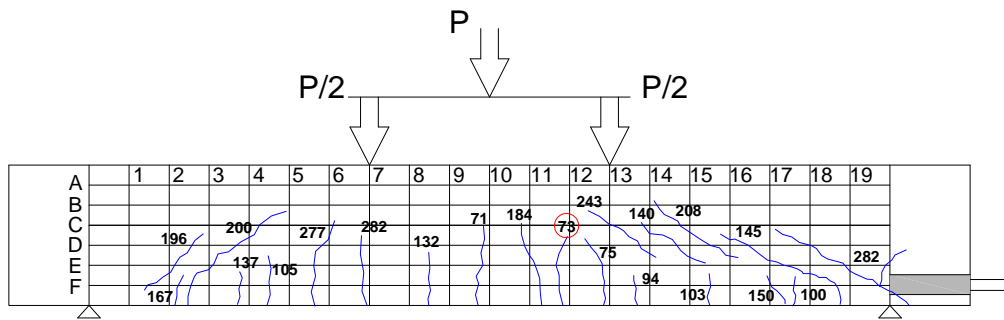**Figure A.2: Load-Cracking pattern of specimen A-C2.5-U-3B**
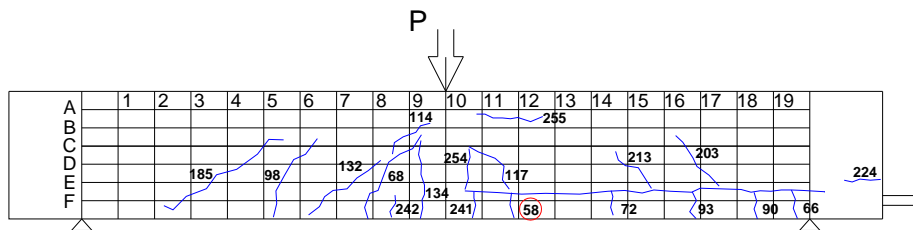
Figure A.3: Load-Cracking pattern of specimen A-C5-U-3B
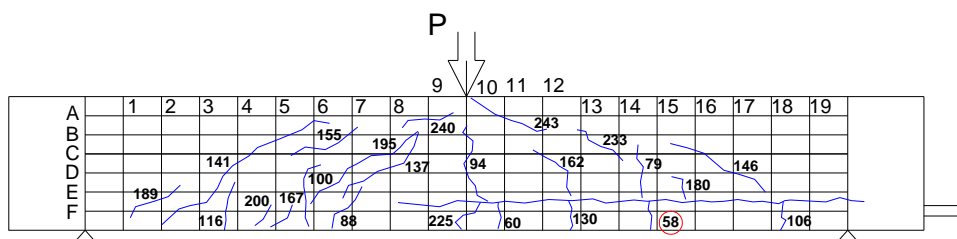
Figure A.4: Load-Cracking pattern of specimen A-C7.5-U-3B

127
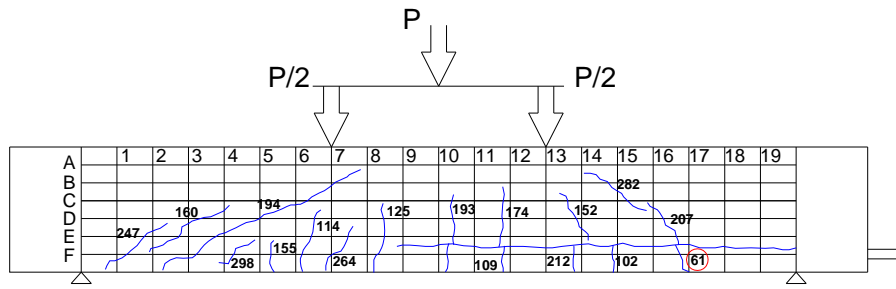
Figure A.5: Load-Cracking pattern of specimen A-C7.5-U-4B
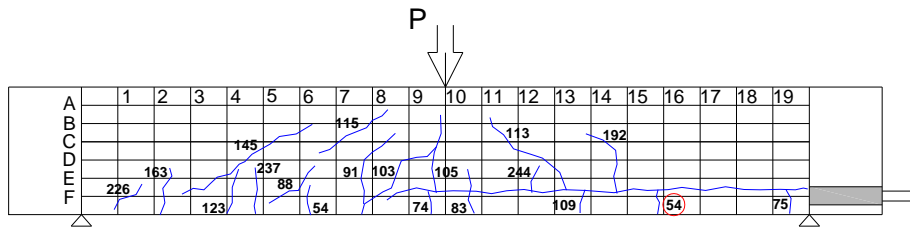
Figure A.6: Load-Cracking pattern of specimen N-C7.5-U-3B
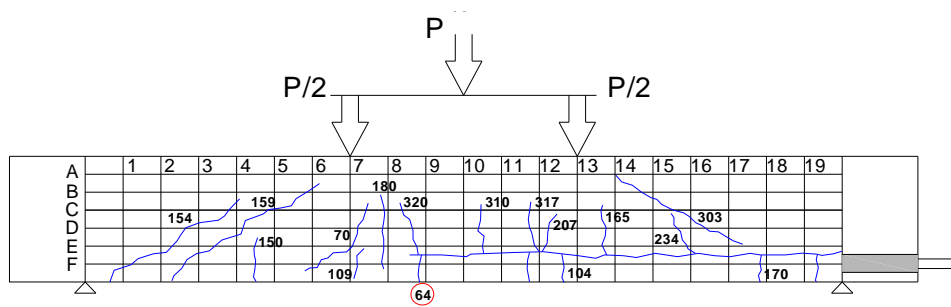
Figure A.7: Load-Cracking pattern of specimen N-C7.5-U-4B
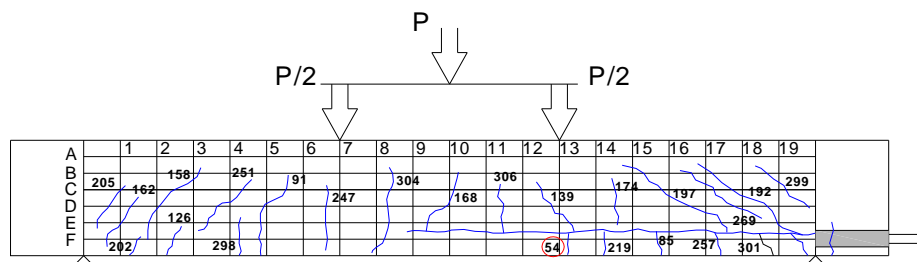
Figure A.8: Load-Cracking pattern of specimen N-C15-U-4B

128
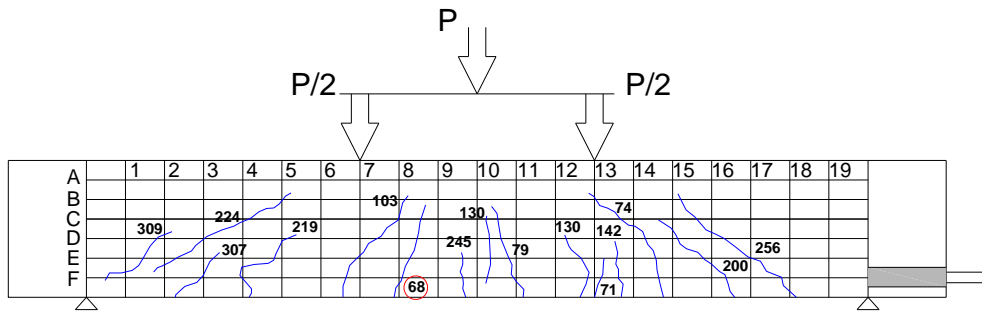
Figure A.9: Load-Cracking pattern of specimen N-C7.5-R(GFRCM)-4B
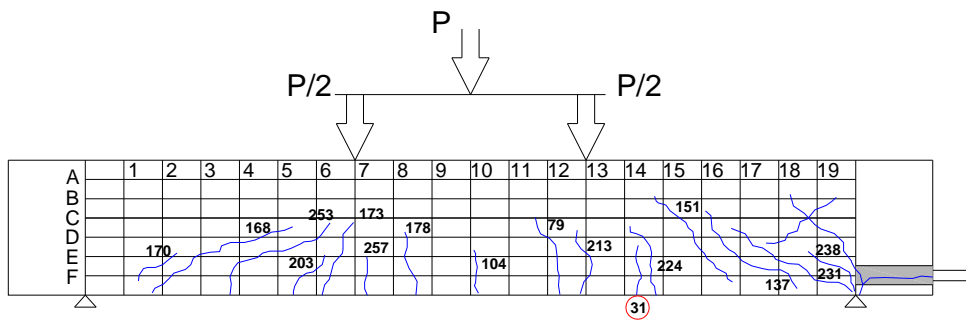
Figure A.10: Load-Cracking pattern of specimen N-C7.5-R(P)-4B
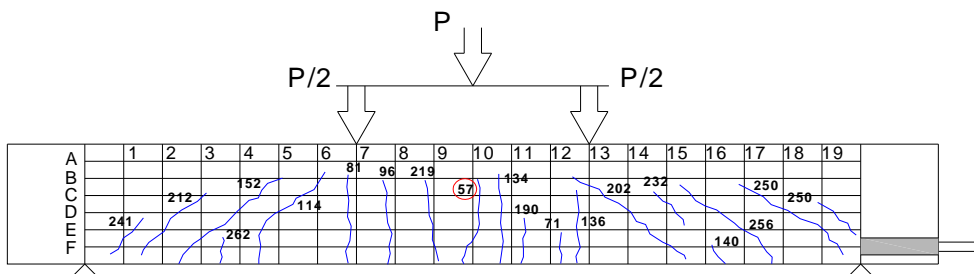
Figure A.11: Load-Cracking pattern of specimen N-C15-R(GFRCM)-4B
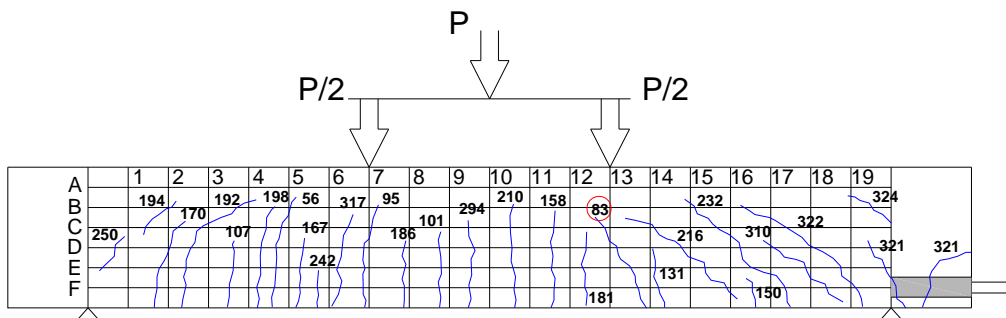
Figure A.12: Load-Cracking pattern of specimen N-C15-R(CFRCM)-4B

129

Figure A.13: Load-Cracking pattern of specimen N-C15-R(P)-4B
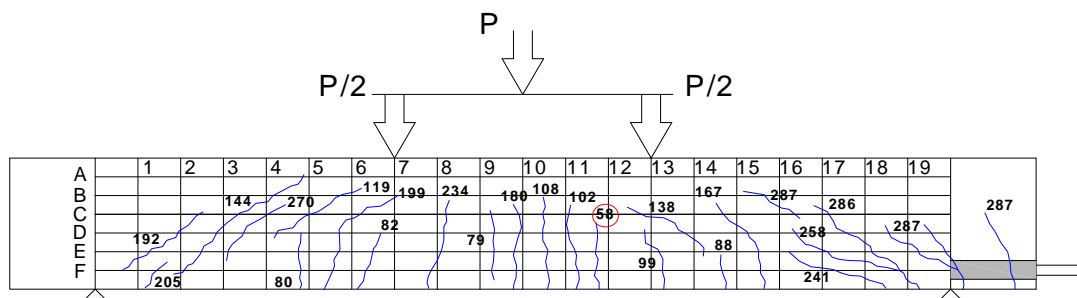
Figure A.14: Load-Cracking pattern of specimen N-C15-R(P+GFRCM)-4B
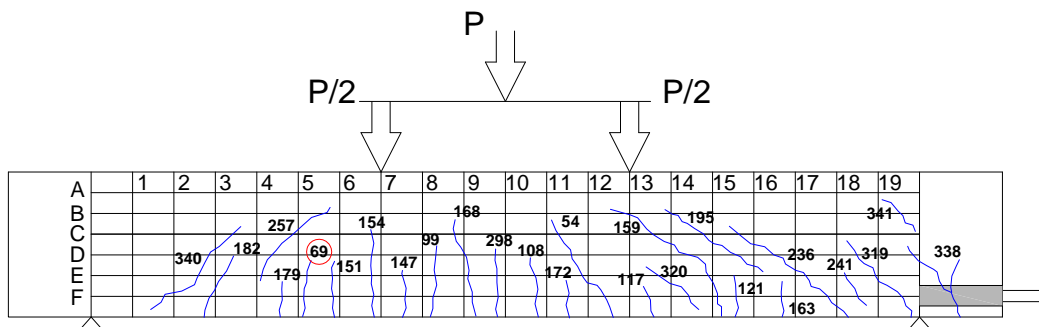
Figure A.15: Load-Cracking pattern of specimen N-C15-R(P+CFRCM)-4B

Concrete crushing

Dominated flexural crack

Figure B.1: Failure mode of specimen A-C0-U-3B

Flexural failure

Dominated flexural crack

Figure B.2: Failure mode of specimen A-C2.5-U-3B

Flexural failure

Dominated flexural crack

Figure B.3: Failure mode of specimen A-C5-U-3B
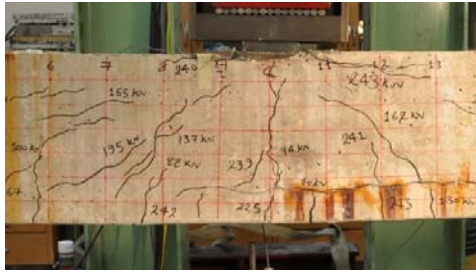
Flexural failure   Dominated flexural crack

Figure B.4: Failure mode of specimen A-C7.5-U-3B

Flexural failure   Dominated flexural crack

Figure B.5: Failure mode of specimen N-C7.5-U-3B
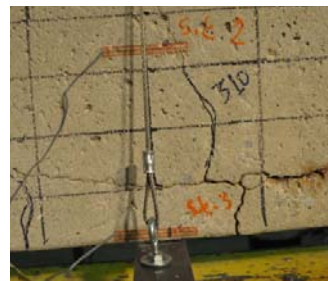
Flexural failure   Dominated flexural crack

Figure B.6: Failure mode of specimen N-C7.5-U-4B
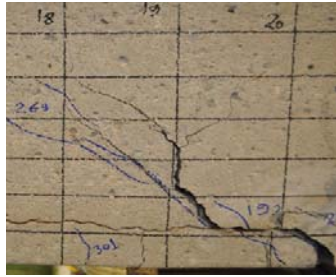
Critical inclined shear-bond Crack

Bottom view for the failure zone

Back view for the anchorage failure

Splitting induced cracks

Figure B.7: Failure mode of specimen N-C15-U-4B

Concrete crushing

Dominated flexural crack

Figure B.8: Failure mode of specimen N-C7.5-R(GFRCM)-4B
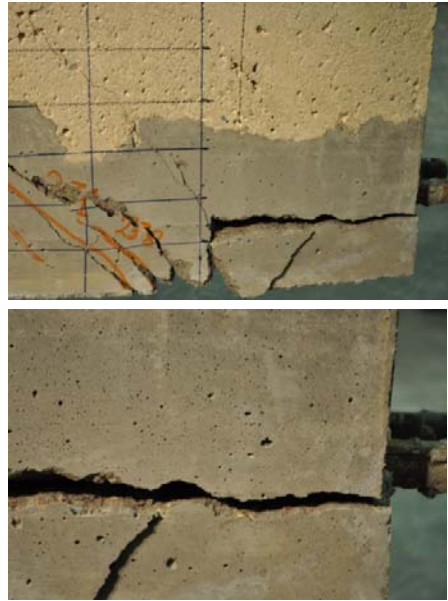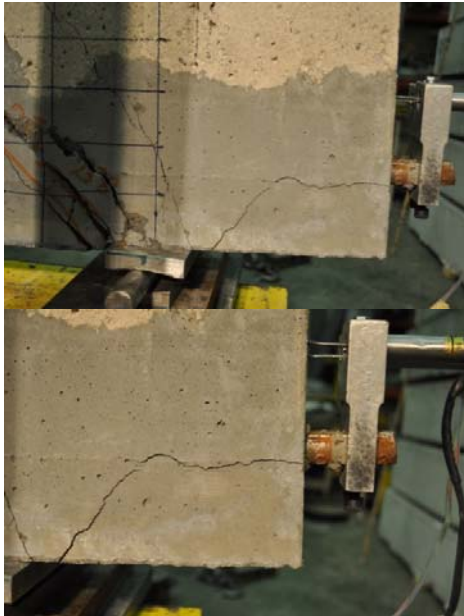
Propagation of Splitting crack.
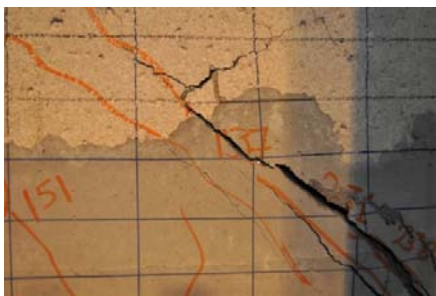
Critical inclined shear-bond Crack

Figure B.9: Failure mode of specimen N-C7.5-R(P)-4B
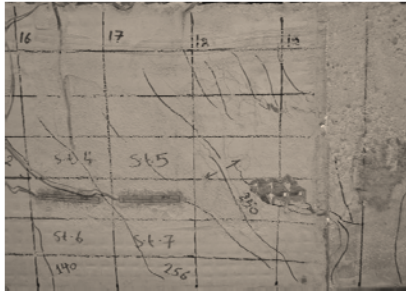
Critical crack location (front view)

Critical crack location (back view)

Figure B.10: Failure mode of specimen N-C15-R(GFRCM)-4B
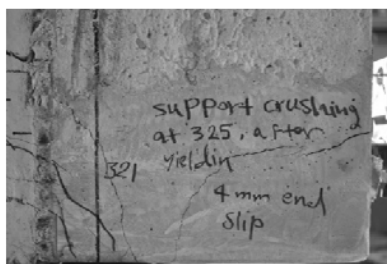
Critical crack location (front view)

Critical crack location (back view)

Figure B.11: Failure mode of specimen N-C15-R(CFRCM)-4B

Propagation of Splitting crack

Critical inclined shear-bond Crack

Figure B.12: Failure mode of specimen N-C15-R(P)-4B

Critical shear-bond crack (front view)
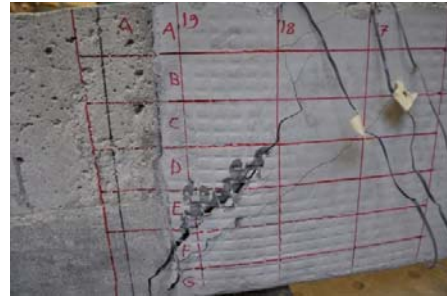
Critical shear-bond Crack (back view)

Figure B.13: Failure mode of specimen N-C15-R(P+GFRCM)-4B

Critical shear-bond crack (front view)

Critical shear-bond Crack (back view)

Figure B.14: Failure mode of specimen N-C15-R(P+CFRCM)-4B
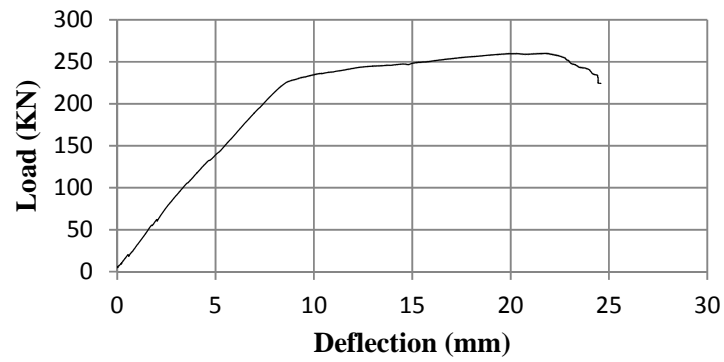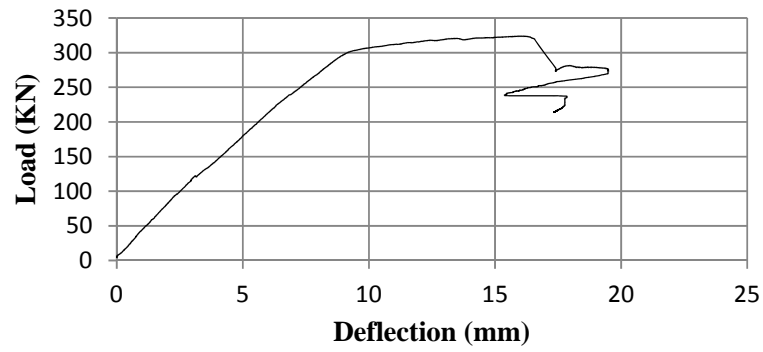
Appendix C

Load-deflection Responses
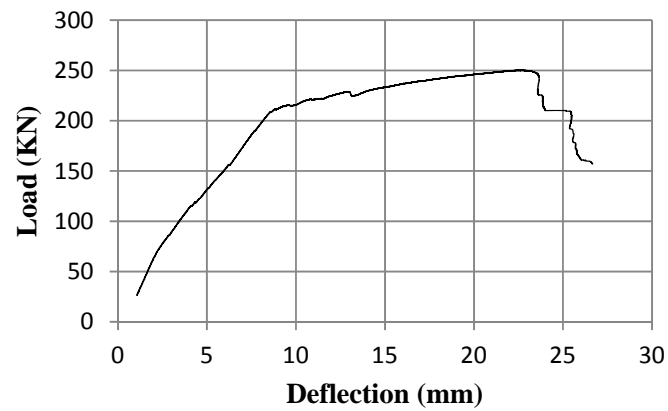
Figure C.1: Load-deflection response of specimen A-C0-U-3B
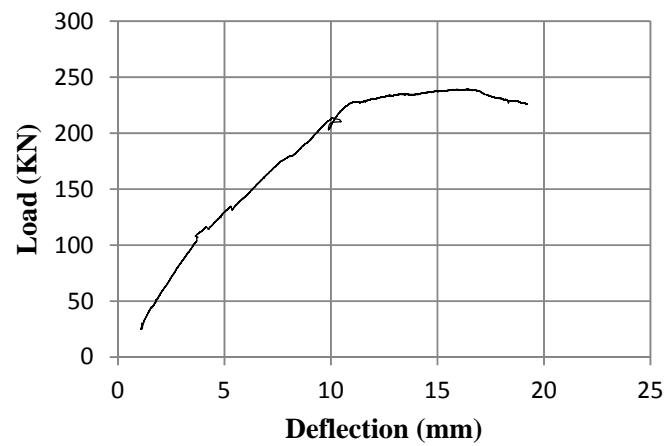
Figure C.2: Load-deflection response of specimen A-C2.5-U-3B
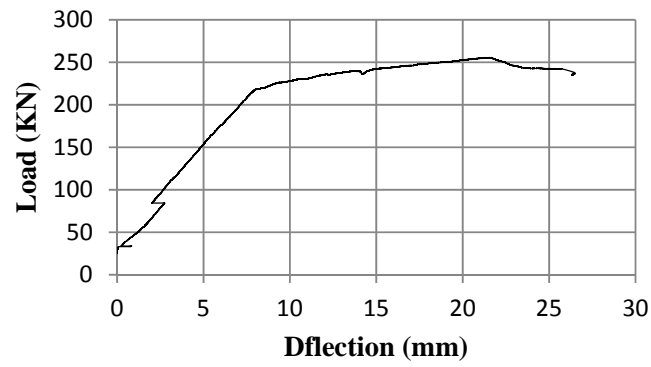
Figure C.3: Load-deflection response of specimen A-C5-U-3B
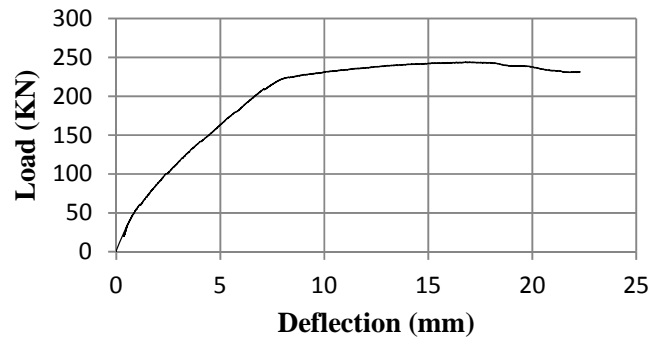
Figure C.4: Load-deflection response of specimen A-C7.5-U-3B
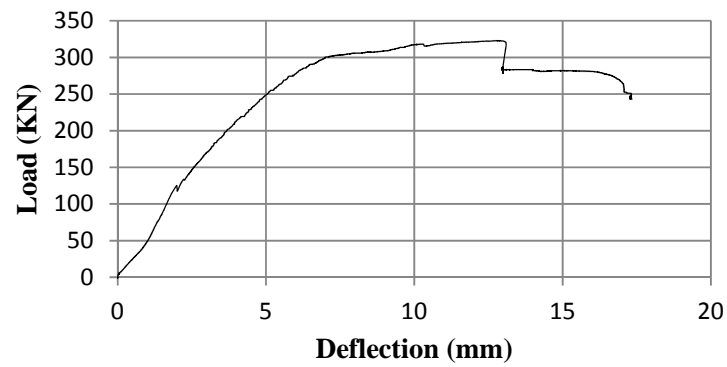
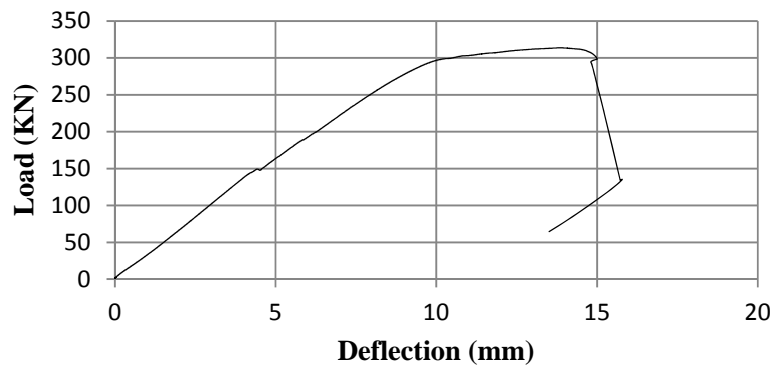**Figure C.5: Load-deflection response of specimen A-C7.5-U-4B**

Figure C.6: Load-deflection response of specimen N-C7.5-U-3B

Figure C.7: Load-deflection response of specimen N-C7.5-U-4B

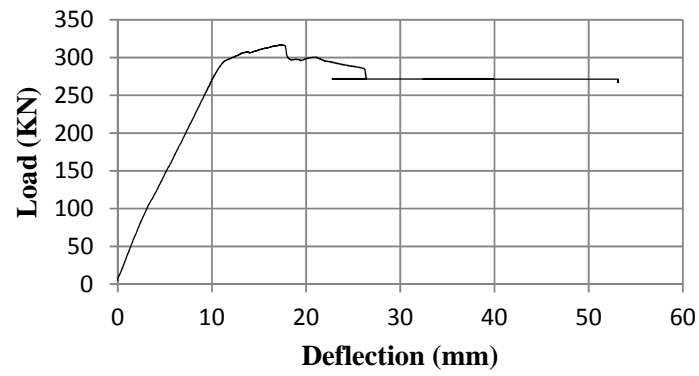**Figure C.8: Load-deflection response of specimen N-C15-U-4B**

Figure C.9: Load-deflection response of specimen N-C7.5-R(GFRCM)-4B
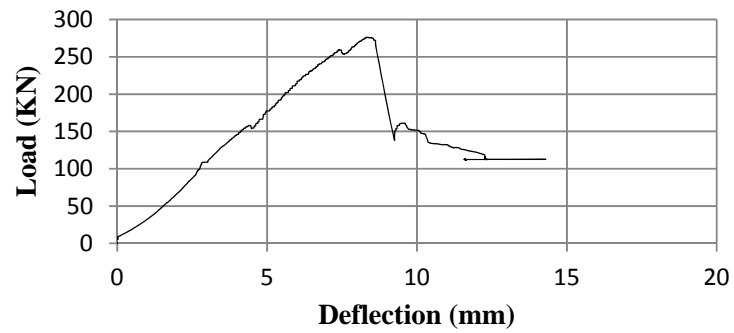

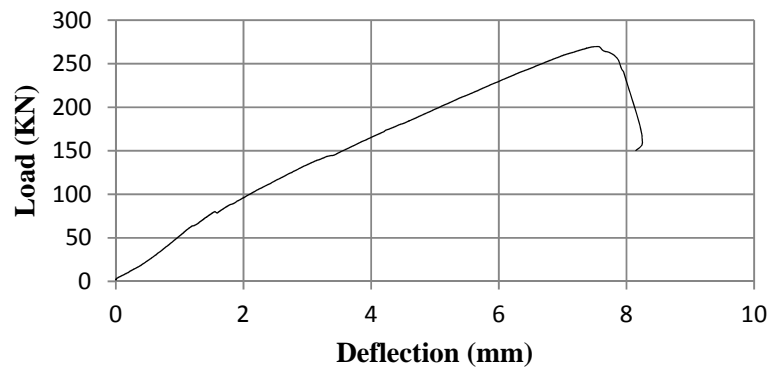**Figure C.10: Load-deflection response of specimen N-C7.5-R(P)-4B**

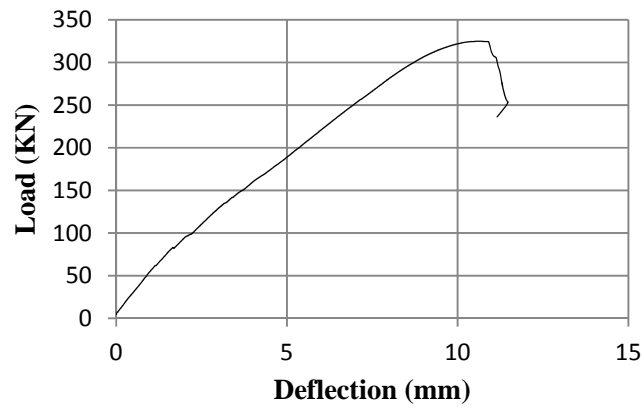**Figure C.11: Load-deflection response of specimen N-C15-R(GFRCM)-4**

Figure C.12: Load-deflection response of specimen N-C15-R(CFRCM)-4B
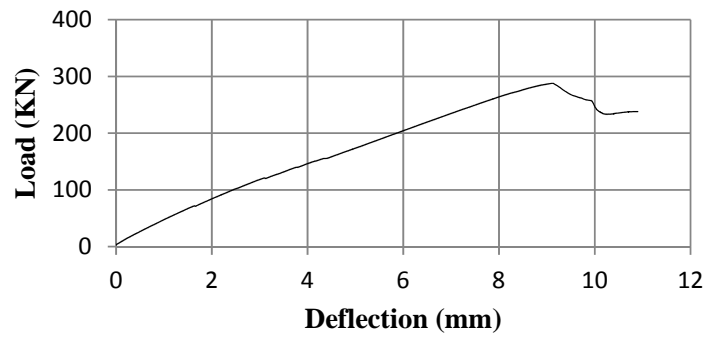

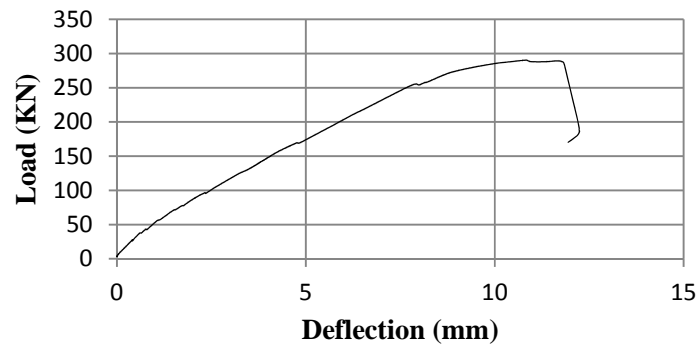**Figure C.13: Load-deflection response of specimen N-C15-R(P)-4B**

Figure C.14: Load-deflection response of specimen N-C15-R(P+GFRCM)-4B
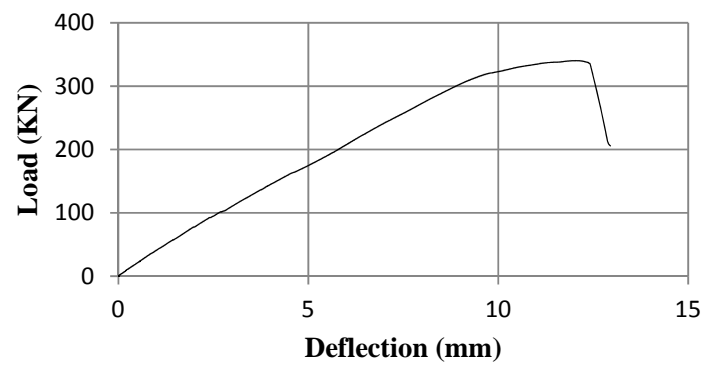
Figure C.15: Load-deflection response of specimen N-C15-R(P+CFRCM)-4B

Appendix D
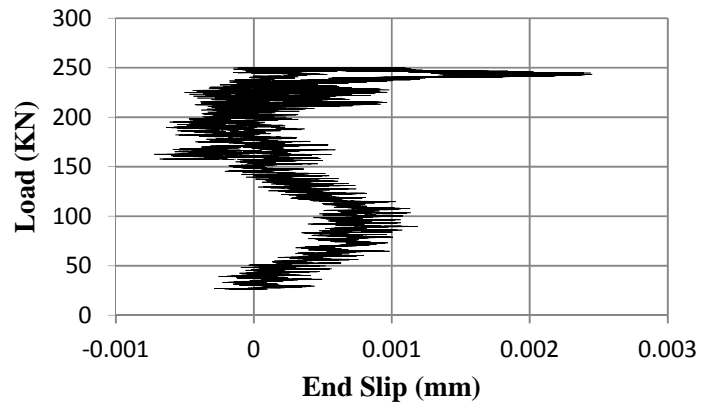# Load-end-slip Responses

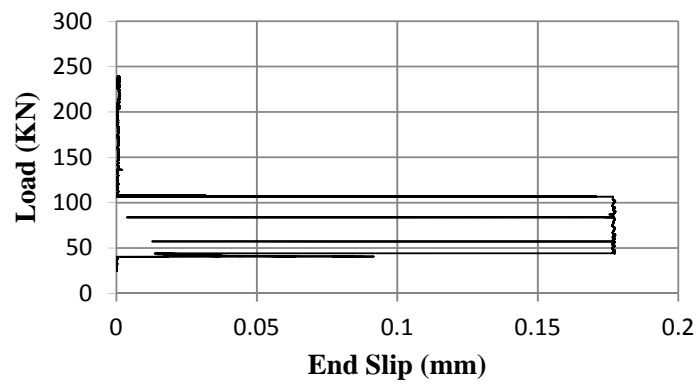**Figure D.1: Load-end slip response of specimen A-C0-U-3B**

Figure D.2: Load-end slip response of specimen A-C2.5-U-3B
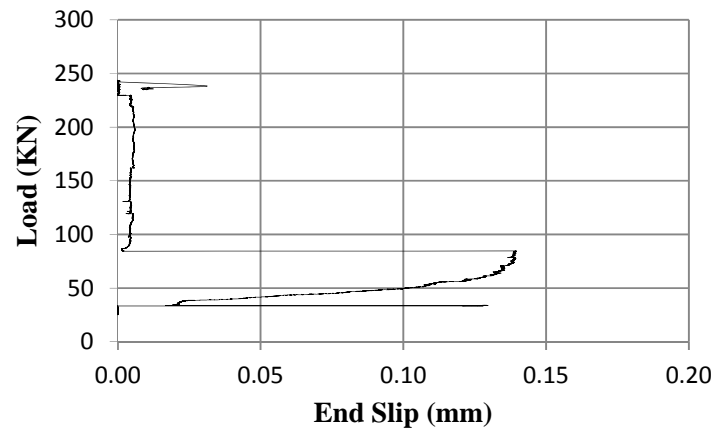
Figure D.3 Load-end slip response of specimen A-C5-U-3B

Figure D.4: Load-end slip response of specimen A-C7.5-U-3B
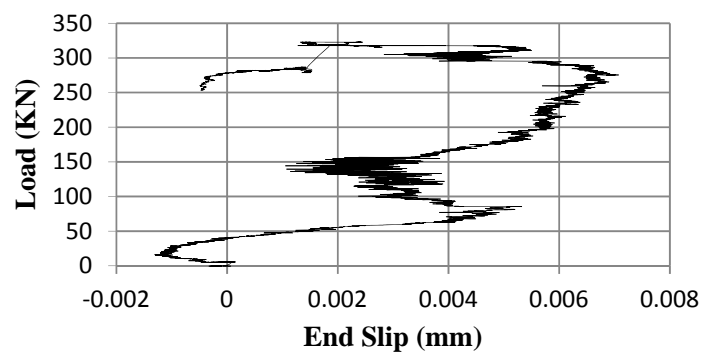
Figure D.5: Load-end slip response of specimen A-C7.5-U-4B

144

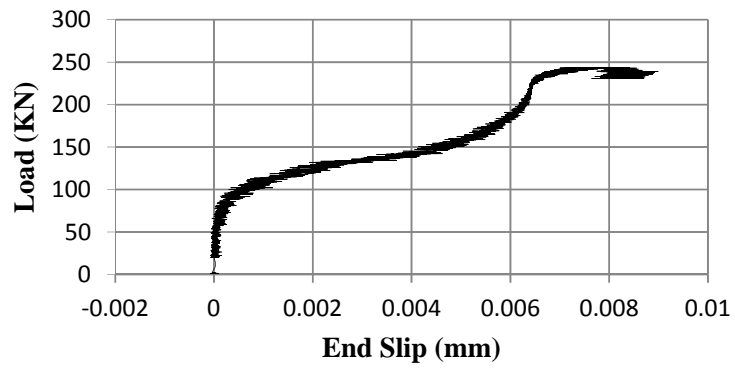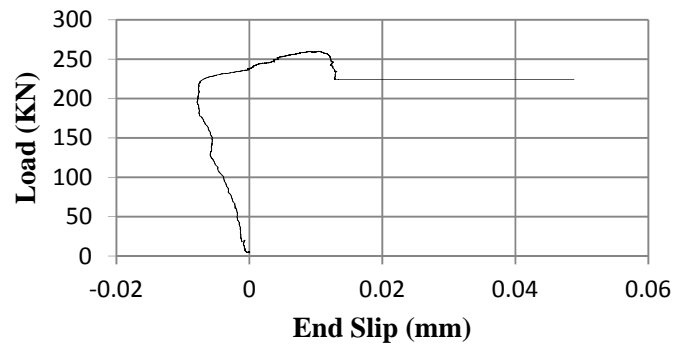**Figure D.6: Load-end slip response of specimen N-C7.5-U-3B**
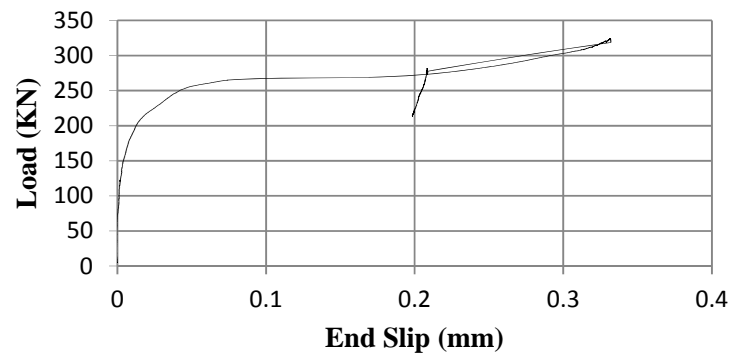
Figure D.7: Load-end slip response of specimen N-C7.5-U-4B

Figure D.8: Load-end slip response of specimen N-C15-U-4B
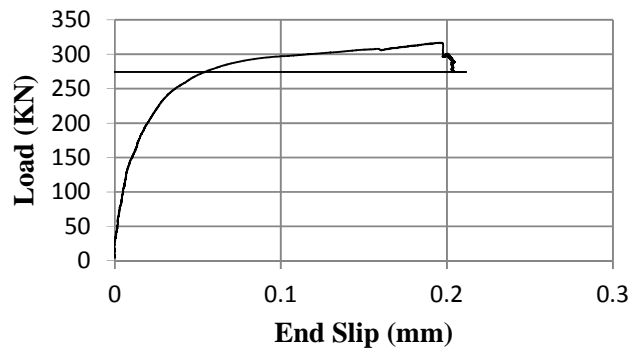
Figure D.9: Load-end slip response of specimen N-C7.5-R(GFRCM)-4B

Figure D.10: Load-end slip response of specimen N-C7.5-R(P)-4B

Figure D.11: Load-end slip response of specimen N-C15-R(GFRCM)-4B

146

Figure D.12: Load-end slip response of specimen N-C15-R(CFRCM)-4B

Figure D.13: Load-end slip response of specimen N-C15-R(P)-4B

Figure D.14: Load-end slip response of specimen N-C15-R(P+GFRCM)-4B
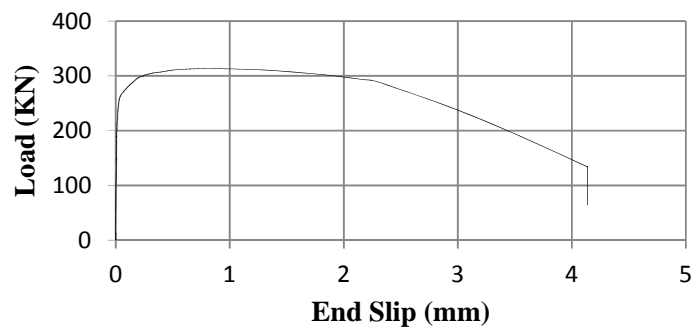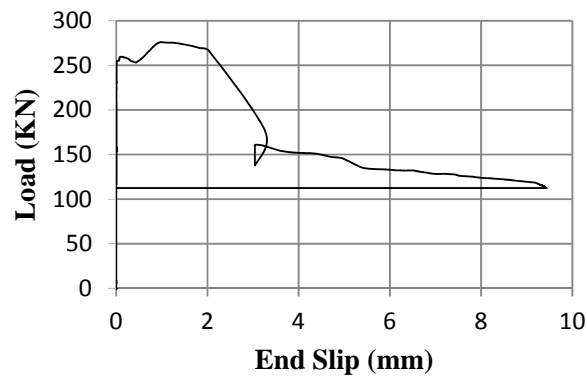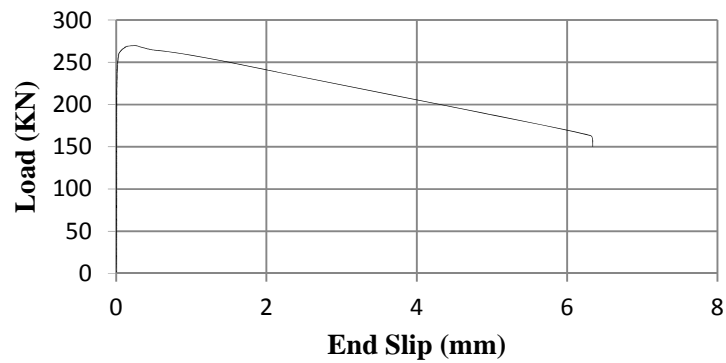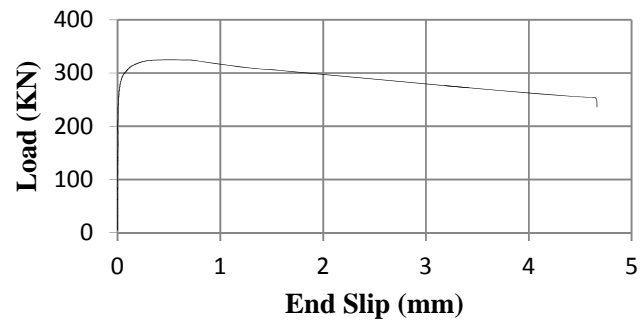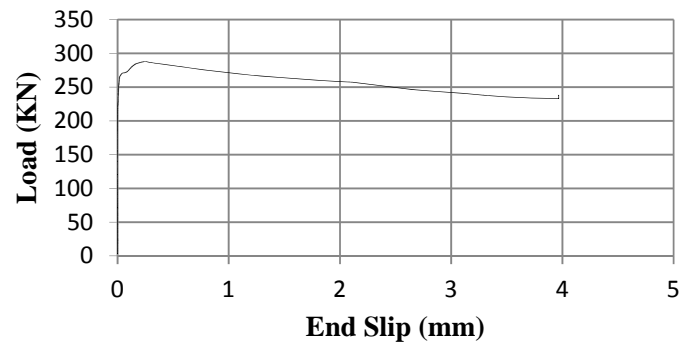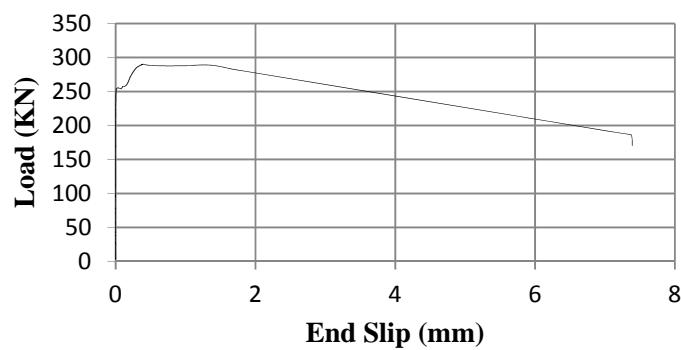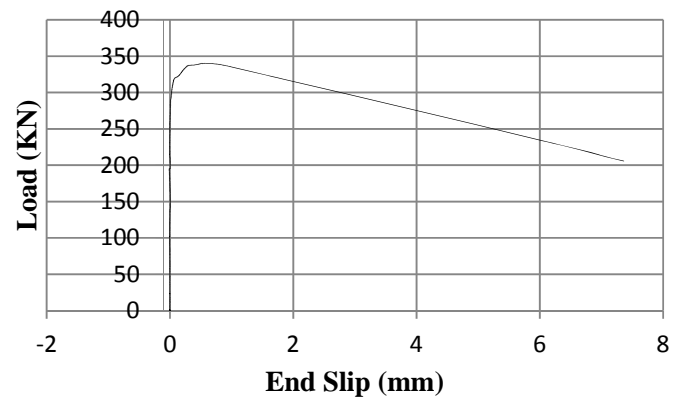
147

Figure D.15: Load-end slip response of specimen N-C15-R(P+CFRCM)-4B

Appendix E

Proposed parameters for the bond stress-end slip model
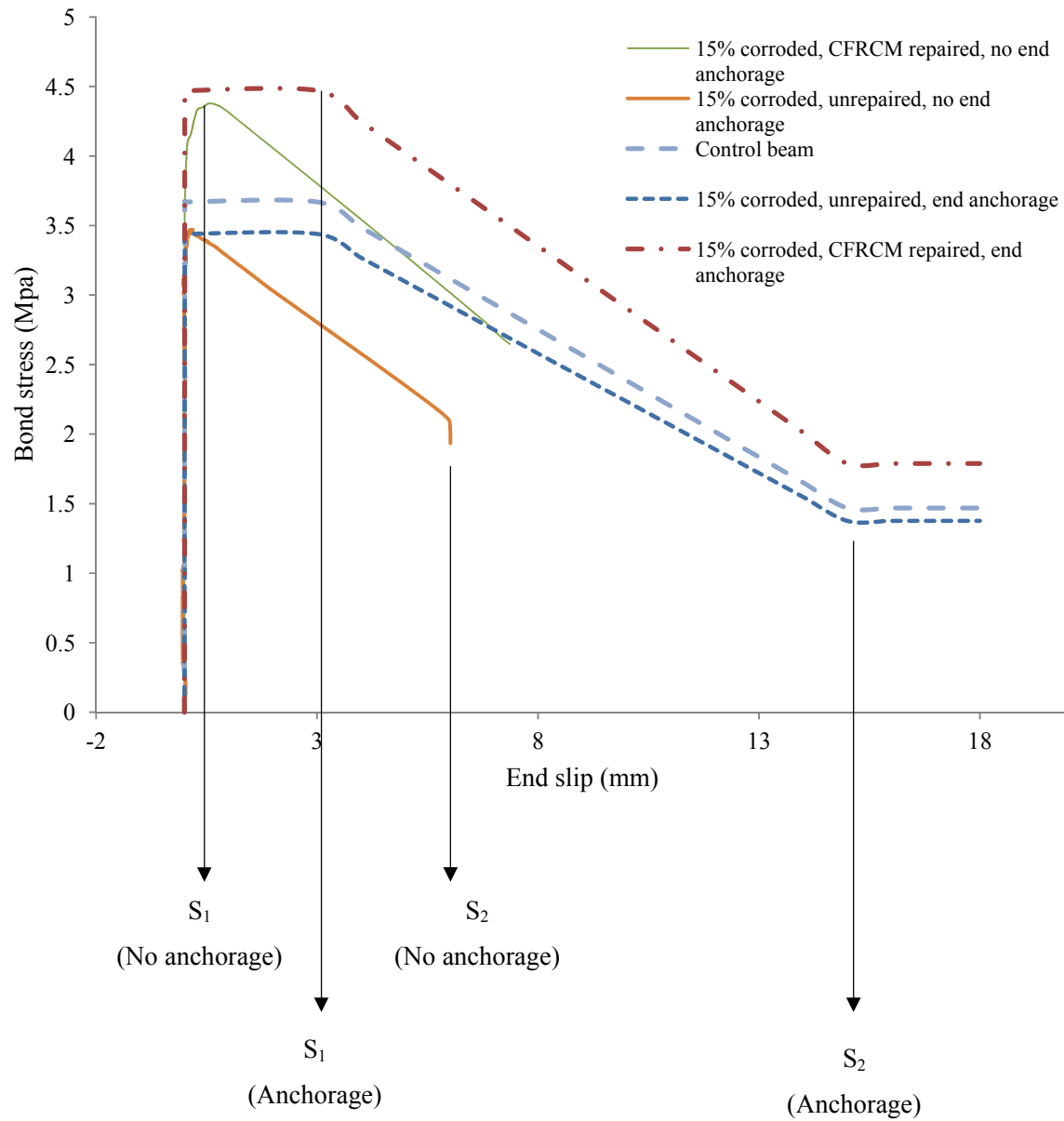

Figure E1: Proposed parameters for the bond stress-end slip model

Bibliography

American Concrete Institute (ACI). (2008). "Guide for the design and construction of externally bonded FRP systems for strengthening concrete structures." ACI 440.2R-08, Farmington Hills, MI.

ACI Committee 408, 2003. Bond and Development of Straight Reinforcing Bars in Tension (ACI 408-03). American Concrete Institute, Farmington Hills, MI, 49 p.

Al-Sulaimani, G.I. Kaleemullah M, Basunbul I A, & Rasheeduzzafar. , (1990). "Influence of corrosion and cracking on bond behaviour and strength of reinforced concrete members." *Proceedings American Concrete Institute*. 87(2), pp. 220-231.

Almusallam, A. A., (2001). "Effect of degree of corrosion on the properties of reinforcing steel bars." *Construction and Building Materials*, 15(8), pp.361-368.

Almusalam Abdullah, A, AI-Gahtani Ahmad S., Aziz Abdur Rauf and Rasheeduzzafar.. (1995), "Effect of reinforcement corrosion on bond strength." *Construction and Building Material*, 10(2), pp. 123-129.

Al-Negheimish, A. I., & Al-Zaid, R. Z. (2004). "Effect of manufacturing process and rusting on the bond behaviour of deformed bars in concrete." *Cement and Concrete Composites*, 26(6), pp.735-742.

Amleh. L. and Mirza, M.S., (1999). "Corrosion Influence on Bond Between Steel and Concrete,"*ACI Structural Journal*, May - June, pp. 415- 423.

ASTM. Standard test method for half-cell potentials of uncoated reinforcing steel in concrete. C876-91, West Conshohocken, PA,2002.

ASTM. Standard practice for preparing, cleaning, and evaluating corrosion test specimens. G1-90, West Conshohocken, PA, 2002.

Auyeung, Yubun, Balaguru, P .. and Chung. Lan. , (2000). "Bond Behaviour of Corroded Reinforcement Bars." *ACI journal*. No. 97-M28, pp. 2 I 4-220.

Azad, A. K., Ahmad, S., & Al-Gohi, B. H. A. (2010). "Flexural strength of corroded reinforced concrete beams." *Magazine of Concrete Research*, 62(6), pp.405-414.

Badanoiu, A., and Holmgren, J. (2003). "Cementitious composites reinforced with continuous carbon fibers for strengthening of concrete structures." *Cem. Concr. Compos.*, 25(4), 387–394.

Badawi, M., and Soudki, K.A. (2004). "Control of corrosion-induced damage in RC beams using CFRP laminates". *Journal of Composites for Construction, ASCE*, 9: 195-201.

Badawi, M. and Soudki, K., (2005). "Control of Corrosion-Induced Damage in Reinforced Concrete Beams using Carbon Fiber-Reinforced Polymer Laminates," *ASCE Journal of Composites for Construction*, 9(2), March, pp.195-201.

Badawi, M., & Soudki, K. (2010). "CFRP repair of RC beams with shear-span and full-span corrosions". *Journal of Composites for Construction*, 14(2): 323-335.

Bhargava, K., Ghosh, A. K., Mori, Y., & Ramanujam, S. (2008). "Suggested empirical models for corrosion-induced bond degradation in reinforced concrete". *Journal of Structural Engineering*, 134(2), 221-230.

Broomfield, J.P., 1997. "Corrosion of Steel in Concrete: Understanding, Investigation and Repair," E&FN Spon, London.

Brückner, A., Ortlepp, R., & Curbach, M. (2006). "Textile reinforced concrete for strengthening in bending and shear. Materials and *Structures/Materiaux Et Constructions*," 39(292), pp.741-748.

Cabrera, J. G. (1996). "Deterioration of concrete due to reinforcement steel corrosion." *Cement and Concrete Composites*, 18(1), pp.47-59.

CEB (2000): CEB-FIB Bond of reinforcement in concrete. CEB Bulletin d'Information No. 10, Lausanne 2000, pp.188-215.

CEB (1993): CEB-FIP Model Code 1990. CEB Bulletin d'Information No. 213/214, Lausanne 1993.

Chung, L., Cho, S., Kim, J. J., & Yi, S. (2004). "Correction factor suggestion for ACI development length provisions based on flexural testing of RC slabs with various levels of corroded reinforcing bars". *Engineering Structures*, 26(8), pp.1013-1026.

Collins, M.P., and Mitchell, D., 1997. "Prestressed concrete structure", Response publication, Toronto, Canada.

Coronelli, D. (2002). "Corrosion Cracking and Bond Strength Modeling for Corroded Bars in Reinforced Concrete". *ACI Structural Journal*, 99(3), pp. 267-276.

Coronelli, D; and Gambarova, P., (2004) "Structural Assessment of Corroded RC Beams: Modeling Guidelines." *Journal of structural engineering*, 130(8),pp.1207-1214.

Craig, B., and Soudki, K.A. (2005). "Post-repair performance of bond critical corrosion damaged concrete beams repaired with CFRP". *Fiber-Reinforced Polymer Reinforcement for Concrete Structures* (FRPRCS-7), Kansas City, Mo. American Concrete Institute, Farmington Hills, Mich. ACI SP230, pp. 563-578.

CSA. 2004. Design of concrete structures. Standard A23.3, Canadian Standards Association, Rexdale, Ont.

Coronelli, D., and Gambarova, P.G., (2000), "A Mechanical Model for Bond Strength of Corroded Reinforcement in Concrete", In Proceedings of EM2000, *14th ASCE Engineering Mechanics Conference*, Austin, Tex. CD-ROM. American Society of Civil Engineers, Reston.

Coronelli, D., (2002), "Corrosion Cracking and Bond Strength Modeling for Corroded Bars in Reinforced Concrete", *ACI Structural Journal*, 99(3), pp. 267-276.

Coronelli, D., & Gambarova, P. (2004). "Structural assessment of corroded reinforced concrete beams: Modeling guidelines". *Journal of Structural Engineering*, 130(8), pp.1214-1224.

D'Ambrisi, A., & Focacci, F. (2011). "Flexural strengthening of RC beams with cement-based composites". *Journal of Composites for Construction*, 15(5), pp.707-720.

El Maaddawy, T., and Soudki, K.A. (2003). "Effectiveness of impressed current techniques to simulate steel reinforcement corrosion." *Journal of Materials in Civil Engineering*, ASCE, 5: 41-47.

El Maaddawy, T., Soudki, K.A., and Topper T. (2004). "Computer-based mathematical model for performance prediction of corroded beams repaired with fibre reinforced polymers". *Journal of Composites for Construction*, ASCE, 9: 227-235.

El Maaddawy, T., Soudki, K.A., and Topper, T. (2005a). "Analytical model to predict the nonlinear Flexural behaviour of corroded reinforced concrete beams". *ACI Structural Journal*, 102: 550-560.

El Maadawy, T., Soudki, K.A., and Topper, T. (2005b). "Long-term performance of corrosion-damaged reinforced concrete beams". *ACI Structural Journal*, 102: 649-656.

El Maaddawy, (T. a. 2005). "Modeling the Non-linear Flexural Response of Corroded and FRP-repaired Beams". *Fourth Middle East Symposium on Structural Composites for Infrastructure* Applications, 20-23. Alexandria, Egypt.

Emberson, N. K., & Mays, G. C. (1996). "Significance of property mismatch in the patch repair of structural concrete. part 3: Reinforced concrete members in flexure". *Magazine of Concrete Research*, 48(1), pp. 45-57

Fang, C., Lundgren, K., Chen, L., & Zhu, C. (2004). "Corrosion influence on bond in reinforced concrete". *Cement and Concrete Research*, 34(11), pp.2159-2167.

Fib, 2000, Bond of Reinforcement in Concrete, State-of-the-art Report, Bulletin 10, fib-International Federation for Structural Concrete, Lausanne.

Fu, X., & Chung, D. D. L. (1997). "Effect of corrosion on the bond between concrete and steel rebar". *Cement and Concrete Research*, 27(12), pp.1811-1815.

Girard, C., and Bastien, J., (2002), "Finite-Element Bond-Slip Model for Concrete Columns under Cyclic Loads", ASCE, *Journal of Structural Engineering*, 128(12), pp. 1502-1510.

Gu, P., Beaudoin, J. J., Zhang, M.-H., and Malhotra, V. M. (1999). ''Performance of steel reinforcement in portland cement and high-volume fly ash concretes exposed to chloride solution.'' *ACI Mater. J.*, 96(5), pp.551–558.

Khalfallah, S., and Ouchenane, M., (2008). "Prediction of Bond between Steel and Concrete by Numerical Analysis." *The open Civil Engineering Journal*, 2(1), pp. 1-8.

Koch, G., H., Brongers, M., P., H., Thompson, N., G., Virmani, Y., P., and Payer, J., H., (2001) Corrosion cost and preventive strategies in the United States Federal Highway Administration Report (FHWA-RD-01-156)

Lee, H. -., Noguchi, T., & Tomosawa, F. (2002). "Evaluation of the bond properties between concrete and reinforcement as a function of the degree of reinforcement corrosion". *Cement and Concrete Research*, 32(8), pp.1313-1318.

Lundgren, K. (2002). "Modelling the effect of corrosion on bond in reinforced concrete". *Magazine of Concrete Research*, 54(3), pp.165-173.

Lundgren K. (2005a): "Bond between ribbed bars and concrete. Part 1: Modified model." *Magazine of Concrete Research*, 57(7), September, pp. 371-382

Lundgren, K. (2005b). "Bond between ribbed bars and concrete. part 2: The effect of corrosion". *Magazine of Concrete Research*, 57(7), pp.383-395.

Lundgren, K. (2007). "Effect of corrosion on the bond between steel and concrete: An overview." *Magazine of Concrete Research*, 59(6), pp.447-461.

Lundgren, K., Kettil, P., Hanjari, K. Z., Schlune, H., & Roman, A. S. S. (2012). "Analytical model for the bond-slip behaviour of corroded ribbed reinforcement". *Structure and Infrastructure Engineering*, 8(2), pp.157-169.

MacGregor J.G., "Reinforced Concrete," Prentice Hall, 3rd Edition, NJ, USA, 1996.

MacGregor, James G.; and Banleu, Michael F. RG Mechanics and Design (1st Canadian Edition: Scarborough, Prentice rIall,(2000):89-367.

Masoud, S., & Soudki, K. (2000). "Serviceability of corroded reinforced concrete beams strengthened with carbon fiber reinforced polymer sheets". Paper presented at the 2000 Annual Conference Abstracts – *Canadian Society for Civil Engineering*, 261.

Masoud, S. a. (2001). "Serviceability of Corroded Carbon Fibre Reinforced Polymer Strengthened Reinforced Concrete Beams". Proceedings of 3rd *Structural Speciality Conference of the Canadian Society for Civil Engineering*, 507-514. London.

Masoud, S., Soudki, K., and Topper, T. (2001). "CFRP-strengthened and corroded RC beams under monotonic and fatigue loads." *J. Compos. Constr*., 5(4), 288–236.

Malumbela, G., Moyo, P., & Alexander, M. (2011). "Load-bearing capacity of corroded, patched and FRP-repaired RC beams". *Magazine of Concrete Research*, 63: 797-812.

Nilson, A. H.; Darwin, D.,; and Dolan, C. W., (2004), Design of Concrete Structures, 13th Edition, McGraw-Hill,New York, 779 pp.

Nossoni, G., & Harichandran, R. S. (2010). "Improved repair of concrete structures using polymer concrete patch and frp overlay". *Journal of Materials in Civil Engineering*, 22: 314-322.

Pregartner, T., Cairns, J., & Ožbolt, J. (2004). "Modelling effect of corrosion on bond strength of plain bar reinforcement. Structural Concrete", 5(3), pp.113-120.

Río, O., Andrade, C., Izquierdo, D., & Alonso, C. (2005). "Behaviour of patch-repaired concrete structural elements under increasing static loads to flexural failure". *Journal of Materials in Civil Engineering*, 17(2), pp.168-177.

Rodriguez J., Ortega L., Garcia A. (1994): Corrosion of reinforcing bars and service life of reinforced concrete structures: Corrosion and bond deterioration. Int. Conference, Concrete across borders, Denmark, Vol, II, pp. 315-326

Rogalla, N. S., Carter, J. G., & Pojeta Jr., J. (2003). "Shell microstructure of the late carboniferous rostroconch mollusc apotocardium lanterna (branson, 1965)". *Journal of Paleontology*, 77(4), pp.655-673.

Smith, R. (2007). "The Effect of Corrosion on the Performance Of Reinforced Concrete Beams". MASc Thesis, Ryerson University, Toronto.

Soudki, K. A., Rteil, A. A., Al-Hammoud, R., & Topper, T. H. (2007). "Fatigue strength of fibre-reinforced-polymer-repaired beams subjected to mild corrosion". *Canadian Journal of Civil Engineering*, 34(3), pp.414-421.

Soudki, K., El-Salakawy, E., & Craig, B. (2007). 'Behaviour of CFRP strengthened reinforced concrete beams in corrosive environment'. *Journal of Composites for Construction*, 11: 291-298.

Soudki, K. and Sherwood, T. (2003). "Bond Behaviour of Corroded Steel Reinforcement in Concrete Wrapped with Carbon Fiber Reinforced Polymer Sheets." *J. Mater. Civ. Eng.*, 15(4), pp.358–370.

Soudki, K. A., & Sherwood, T. G. (2000). "Behaviour of reinforced concrete beams strengthened with carbon fibre reinforced polymer laminates subjected to corrosion damage." *Canadian Journal of Civil Engineering*, 27(5), pp.1005-1010.

Sahamitmongkol, R., Suwathanangkul, S., Phoothong, P., and Kato, Y., (2008), "Flexural Behaviour of Corroded RC Members with Patch Repair-Experimental & Simulation." *Journal of Advanced Concrete Technology*, 6: 317-336.

Stanish, K., Hooton, R. D., and Pantazopoulou, S. J. (1999). "Corrosion Effects on Bond Strength in Reinforced Concrete". *ACI Structural Journal*, 96(6), pp. 915-921.

Tassios, T. P., "Properties of bond between concrete and steel under load cycles idealizing seismic actions," in Proceedings of AICAP-CEB Symposium, Rome, Avril 1979, CEB Bulletin No. 131, Paris, pp. 67-122.

Torres-Acosta, A. A., Navarro-Gutierrez, S., & Terán-Guillén, J. (2007). "Residual flexure capacity of corroded reinforced concrete beams." *Engineering Structures*, 29(6), pp.1145-1152.

Val, D. V. 2007. "Deterioration of Strength of RC Beam due to Corrosion and its Influence on Beam Reliability". *Journal of Structural Engineering*, ASCE, 133: pp.1297-1306.

Wang, X., & Liu, X. (2004). "Bond strength modeling for corroded reinforcement in reinforced concrete." *Structural Engineering and Mechanics*, 17(6), pp.863-878.

Wang, X., & Liu, X. (2004). "Modeling bond strength of corroded reinforcement without stirrups." *Cement and Concrete Research*, 34(8), pp.1331-1339.

Wang, C., Shih, C., Hong, S., & Hwang, W. (2004). "Rehabilitation of cracked and corroded reinforced concrete beams with fiber-reinforced plastic patches". *Journal of Composites for Construction*, 8(3), pp.219-228.

Wang, X., & Liu, X. (2010). "Simplified methodology for the evaluation of the residual strength of corroded reinforced concrete beams". *Journal of Performance of Constructed Facilities*, 24(2), pp.108-119.

Wang, X., Gao, X., Li, B., & Deng, B. (2011). "Effect of bond and corrosion within partial length on shear behaviour and load capacity of RC beam". *Construction and Building Materials*, 25(4), pp.1812-1823.

Wang, X., & Liu, X. (2008). "Modeling the flexural carrying capacity of corroded RC beam". *Journal of Shanghai Jiaotong University (Science)*, 13(2), pp.129-135.

Xia, J., Jin, W., & Li, L., (2011). "Shear performance of reinforced concrete beams with corroded stirrups in chloride environment". *Corrosion Science*, 53(5), pp. 1794-1805.